

# UC San Diego

## UC San Diego Electronic Theses and Dissertations

### Title

Nanoparticle "theranostic" platforms for applications in cancer

### Permalink

<https://escholarship.org/uc/item/46b8093m>

### Author

Steiner, Jason Michael

### Publication Date

2011

Peer reviewed|Thesis/dissertation

UNIVERSITY OF CALIFORNIA, SAN DIEGO

Nanoparticle “Theranostic” Platforms for Applications in Cancer

A dissertation submitted in partial satisfaction of the  
requirements for the degree Doctor of Philosophy

in

Materials Science and Engineering

by

Jason Michael Steiner

Committee in Charge:

Professor Sadik Esener, Chair  
Professor Jennifer Cha  
Professor Michael Heller  
Professor Robert Mattrey  
Professor William Trogler

2011

Copyright

Jason Michael Steiner, 2011

All Rights Reserved

The Dissertation of Jason Michael Steiner is approved, and it is acceptable in quality and form for publication on microfilm and electronically:

---

---

---

---

---

Chair

University of California, San Diego

2011

## EPIGRAPH

“Always look for the silver lining...”

## TABLE OF CONTENTS

Signature Page .....	iii
Epigraph .....	iv
Table of Contents .....	v
List of Abbreviations .....	x
List of Figures.....	xii
List of Tables .....	xv
Acknowledgements .....	xvi
Vita .....	xvii
Abstract of the Dissertation .....	xix
Chapter 1: Introduction: Biological Applications of Nanoparticles for Cancer Therapeutics and Diagnostics .....	1
1.1 Background .....	1
1.2 Imaging/Diagnostics .....	3
1.3 Therapeutics .....	4
1.4 Nanoparticle Theranostics .....	6
1.5 Scope of Dissertation .....	7
Chapter 2: DNA Nanoparticles as a Theranostic Platform.....	9
2.1 Introduction/Rationale.....	9
2.2 Systematic Evolution of Ligands by Exponential Enrichment (SELEX) and Aptamers .....	12
2.3 DNA Nanoparticles.....	15

2.4 Synthesis of DNA Nanoparticles.....	16
2.5 Size Characterization—Estimations and Limitations.....	18
2.5.1 Dynamic Light Scattering.....	18
2.5.2 Ideal Chain Polymer Model.....	21
2.6 Protocol for Generating DNA Nanoparticles and Nanoparticle Libraries.....	23
2.7 Exponential Enrichment—Modified SELEX.....	24
2.8 Modified Selection Protocol.....	25
2.9 Human Dendritic Cell Selection Results.....	27
2.9.1 Specificity.....	29
2.9.2 Retention/Abrogation of Binding Activity.....	32
2.10 Effects of Library Size and Random Region Length on Folding and Sequence Space.....	34
2.11 Conclusions and Future Directions.....	37
2.12 Acknowledgements.....	41
Chapter 3: Inorganic Nanoparticle Theranostic Components: Iron Oxide.....	42
3.1 Introduction/Rationale.....	42
3.2 Iron Oxide Synthesis Overview.....	44
3.2.1 Aqueous Synthesis.....	44
3.2.2 Organic Synthesis.....	45
3.3 Iron Oxide Nanoparticle Stabilization.....	45
3.4 Novel Iron Oxide Functionalization.....	46

3.4.1 Iron Oxide Nanoparticle Synthesis Protocol .....	47
3.4.2 Surface Silane Functionalization .....	48
3.4.3 Silane Functionalization Protocol .....	49
3.5 Functionalization Characterization .....	50
3.5.1 Transmission Electron Microscopy .....	50
3.5.2 Fourier Transform Infrared Spectroscopy .....	51
3.5.3 Vibrating Sample Magnetometry.....	52
3.6 Aqueous Stability .....	53
3.7 Proposed Reaction Mechanism .....	55
3.8 Conclusions .....	57
3.9 Acknowledgements.....	57
 Chapter 4: Inorganic Nanoparticle Theranostic Components: Gold	
Nanoshells/Nanocages.....	58
4.1 Introduction/Rationale .....	58
4.2 Gold Nanoshell Synthesis Summary .....	59
4.2.1 Gold Nanoparticle Seeding.....	60
4.2.1.1 Production of Gold Shells on PLGA Templates Via Gold Seeding.....	62
4.2.1.2 Reducing Agents.....	64
4.2.1.3 Protocol For the Production of Gold Nanoshells on PLGA Templates.....	71
4.2.2 Galvanic Replacement.....	72

4.2.2.1 Protocol For Galvanic Replacement	
Reaction .....	77
4.3 Conclusions .....	78
Chapter 5: Core/Hollow Shell Nanostructures of Iron Oxide and Gold .....	82
5.1 Introduction/Rationale .....	82
5.2 Criteria for Effective Magnetic Imaging Particles for In Vivo Utilization .....	85
5.3 Iron Oxide/Gold Core/Hollow Porous Shell Structure.....	85
5.4 Iron Oxide/Gold Core/Hollow Shell Synthesis Via Galvanic Replacement.....	88
5.5 Summary of Silver Coating of Iron Oxide Methods.....	88
5.5.1 Nanoparticle Seeding Mechanisms.....	88
5.5.1.1 Sn <sup>2+</sup> Seeding.....	89
5.5.1.2 Ag[NH <sub>3</sub> ] <sub>2</sub> <sup>+</sup> Adsorption and Reduction .....	89
5.5.2 Direct Reduction on CSIOP Surface .....	90
5.5.2.1 Formaldehyde, Ascorbic Acid, Hydroxylamine, Citrate .....	90
5.5.2.2 Photoreduction .....	92
5.5.2.3 Glucose Reduction and Silver Shell Growth.....	93
5.5.2.4 Protocol for Silver Reduction on CSIOP by Glucose and Subsequent Silver Shell Growth.....	97

5.6 Gold Shell Generation by Galvanic Replacement .....	98
5.6.1 Transmission Electron Microscopy	
Characterization.....	98
5.6.2 Magnetic Response Characterization .....	100
5.7 Magnetic Resonance Imaging Response .....	103
5.8 Conclusions and Future Directions.....	107
5.9 Acknowledgements.....	111
Chapter 6: Concluding Remarks .....	112
References.....	117

## LIST OF ABBREVIATIONS

- MRI—Magnetic Resonance Imaging
- CT—Computed Tomography
- PET—Positron Emission Tomography
- FRET—Fluorescence Resonance Energy Transfer
- NIR—Near Infrared
- PEG—Poly-ethylene glycol
- DNA—Deoxyribonucleic acid
- PCR—Polymerase Chain Reaction
- SELEX—Systematic Evolution of Ligands by Exponential Enrichment
- RCA—Rolling Circle Amplification
- DLS—Dynamic Light Scattering
- PBS—Phosphate Buffered Saline
- PBMC—Peripheral Blood Mononuclear Cell
- DC—Human Dendritic Cell
- Gd—Gadolinium
- ICP-MS—Induced Coupled Plasma Mass Spectrometry
- IOP—Iron Oxide Nanoparticle
- CSIOP-Carboxy Silane Functionalized Iron Oxide Nanoparticle
- PLGA—Poly Lactic-co-Glycolic Acid
- PLL—Poly-L-lysine
- PVP—Polyvinylpyrrolidone
- TEM—Transmission Electron Microscopy

EDTA—Ethylene Diamine Tetraacetic Acid

VSM—Vibrating Sample Magnetometry

## LIST OF FIGURES

Figure 1: Systematic Evolution of Ligands by Exponential Enrichment .....	12
Figure 2: Binding constants of multivalent structures.....	13
Figure 3: Rolling Circle Amplification and Fluorescent Microscopy of DNA Nanoparticles .....	17
Figure 4: Dynamic Light Scattering (DLS) Results of DNA Nanoparticles .....	18
Figure 5: Theoretical Model of Clone 3 Nanoparticle Sequence (reverse complement of template sequence listed Table 1).....	21
Figure 6: Ideal Chain Polymer Model .....	22
Figure 7: DNA Nanoparticle Selection Scheme.....	24
Figure 8: Fluorescent Flow Cytometry Data From Dendritic Cell Selection .....	28
Figure 9. DC Specific Binding by Clone 3 DNA Nanoparticle .....	30
Figure 10: Fluorescence Flow Cytometry Data Showing Clone 3 Specificity Against K562 (a) and Primary Human CLL cells (b) .....	31
Figure 11: Abrogation/Retention of DNA Nanoparticle Binding Characteristics By Selective Hybridization.....	33
Figure 12: Effect of Melting and Cooling DNA Nanoparticles .....	35
Figure 13: Elution Profile of DNA Nanoparticles Purified by Size Exclusion Overlaid With Pt ICP-MS Quantification .....	38
Figure 14: WETSEM Image of DNA Nanoparticles Incubated with Cisplatin.....	39

Figure 15: Summary Schematic of Iron Oxide Nanoparticle Synthesis and Silane Functionalization .....	46
Figure 16: Bare Iron Oxide Nanoparticles .....	48
Figure 17: n-(trimethoxysilylpropyl)ethylene diamine triacetic acid, sodium salt.....	49
Figure 18: Bare IOP (A) and CSIOP (B) Showing No Morphological Differences.....	50
Figure 19: Dynamic Light Scattering Measurements of IOP and CSIOP .....	51
Figure 20: Fourier Transform Infrared Spectroscopy of IOP and CSIOP.....	51
Figure 22: Absorbion at 600nm of CSIOP Over Time .....	54
Figure 23: Proposed Reaction Mechanism for Carboxy Silane Iron Oxide Functionalization .....	55
Figure 24: Seeded Growth of Gold Nanoshells.....	60
Figure 25: Schematic Seeding of PLGA Nanoparticles with Gold Seeds for Gold Shell Production .....	64
Figure 26: Iterative Reduction of Chloroauric Acid on PLGA Templates by Formaldehyde .....	65
Figure 27: Growth of Gold Nanoshells on PLGA Templates Using Hydroxylamine .....	67
Figure 28: Morphology Comparison of Gold Nanoshells on PLGA Templates With Hydroxylamine and Formaldehyde .....	68
Figure 29: Homogeneity of Unwashed Gold Nanoshells Produced with Hydroxylamine Revealing No Free Nucleation .....	69

Figure 30: Schematic of the Galvanic Replacement on Silver Nanocubes.....	73
Figure 31: Images of Gold Nanoshells/Nanocages Produced by the Galvanic Replacement Reaction.....	75
Figure 32: SEM and TEM of Gold Nanocages .....	75
Figure 33: Ag Template vs. Gold Shell Thickness for Homogeneous Galvanic Replacement.....	76
Figure 34: Absorbance Profiles of Galvanic Replaced Samples in Figure 31 .....	77
Figure 35: Visualization of the Interactions of Nanoparticles With Biological Solutions .....	83
Figure 36: Core/Hollow Shell Iron Oxide/Gold.....	86
Figure 37: Photoreduction of Ag <sup>+</sup> on CSIOP Templates.....	92
Figure 38: Characterization of Silver Coated Iron Oxide Nanoparticles Produced Via Glucose Reduction.....	95
Figure 39: Stepwise Growth of Silver Shells over Iron Oxide Templates .....	97
Figure 40: Gold Shell Galvanic Replacement of Silver Coated Iron Oxide .....	99
Figure 41: Saturation Magnetization of Iron Oxide/Gold Core/Hollow Shell Nanoparticles Before and After Nitric Acid Dissolution of Free Silver.....	102
Figure 42: TEM/Photo Images and Absorbance Profiles of Iron Oxide/Gold Core/Hollow Shell Nanoparticles Before and After Nitric Acid Dissolution of Free Silver .....	103

## LIST OF TABLES

Table 1: Oligonucleotide Sequences For DNA Nanoparticle Preparation.....	15
Table 2: Dynamic Light Scattering (DLS) Results of DNA Nanoparticles .....	19
Table 3: Standard Electrode Potentials of the Two Half Reactions of Galvanic Replacement of Silver With Gold.....	72
Table 4: Relaxivity Measurements for Iron Oxide/Hollow Gold Shell Nanoparticles and Free CSIOP.....	105

## ACKNOWLEDGEMENTS

Chapter 2 contains material taken from Steiner, J.M. Sartor, M. Sanchez, A.B. Messmer, D. Freed, A. Esener, S. Messmer, B.T. “DeNano: Selectable deoxyribonucleic acid nanoparticle libraries”, *Journal of Biotechnology*, Vol. 145, Pp, 330-333, 2010.

Chapter 3 contains materials taken from Steiner, J. Esener, S. Self-Limiting Deposition of *n*-(Trimethoxysilylpropyl)ethylene Diamine Triacetic Acid for the Production of Aqueous-Stable Iron Oxide Nanoparticles. *Chemistry Letters*. Vol. 40 (2011) , No. 5 p.536.

Chapter 5 contains materials taken from Steiner, J. Esener, S. Iron Oxide/Gold Core/Hollow Porous Shell Nanostructures for Utilization as Magnetic Resonance Contrast Agents (in preparation).

## VITA

- 2004 Bachelor of Science, Bioengineering:Biotechnology, University of California, San Diego
- 2006 Master of Engineering, Bioengineering, University of California, San Diego
- 2011 Doctor of Philosophy, Materials Science and Engineering, University of California, San Diego

## PUBLICATIONS

Steiner, J.M. Sartor, M. Sanchez, A.B. Messmer, D. Freed, A. Esener, S. Messmer, B.T. “DeNano: Selectable deoxyribonucleic acid nanoparticle libraries”, *Journal of Biotechnology*, Vol. 145, Pp, 330-333, 2010.

Steiner, J. Esener, S. “Self-Limiting Deposition of *n*-(Trimethoxysilylpropyl) ethylene Diamine Triacetic Acid for the Production of Aqueous-Stable Iron Oxide Nanoparticles.” *Chemistry Letters*. Vol. 40 (2011) , No. 5 p.536.

Stuart Ibsen, Michael Benchimol, Dmitri Simberg, Carolyn Schutt, Jason Steiner, Sadik Esener, “A Novel Nested Liposome Drug Delivery Vehicle Capable of Ultrasound Triggered release of its payload”, *Journal of Controlled Release* (accepted 2011)

Steiner, J. Esener, S. “Iron Oxide/Gold Core/Hollow Porous Shell Nanostructures for Utilization as Magnetic Resonance Contrast Agents” (in preparation for submission for publication).

#### FIELDS OF STUDY

Nanotechnological Applications in Cancer Research

Professor Sadik Esener

ABSTRACT OF THE DISSERTATION

Nanoparticle “Theranostic” Platforms for Applications in Cancer

by

Jason Michael Steiner

Doctor of Philosophy in Materials Science and Engineering

University of California, San Diego, 2011

Professor Sadik Esener, Chair

The study and implementation of nanotechnology as applied to biology is making substantial progress toward the expansion of the dialogue between synthetic and biological systems. This dialogue leads to a deeper understanding of the origins, manifestations, and characteristics of biological phenomenon that ultimately will lead to improved methods of diagnosing and treating a variety of pathologies. Perhaps the

most prevalent application of this new technology is in the field of cancer research, encompassing an array of diagnostic and therapeutic approaches for *in vivo* utilization. These approaches include novel ways of enhancing tumor imaging for earlier detection or delivering toxic therapeutics directly to the site of action, sparing the systemic damage that so often accompanies cancer treatment. However, it is the combination of these essential and orthogonal functionalities that is the hallmark of the promise of nanotechnology. Such materials, coined as “theranostics” for their therapeutic and diagnostic capabilities, allow for a new depth of understanding of the behavior of nanoparticles *in vivo*, and in particular their efficacy as therapeutic treatments. This dissertation discusses the development of platforms and materials that may be employed as theranostic cancer agents from two distinct philosophical approaches—what may be called “traditional” and “non-traditional” nanotechnology. The “non-traditional” approach details the development of a novel DNA nanoparticle platform created through an exponential enrichment process for selected cell targeting. The products compose a novel class of nanoparticles that possess all of the naturally advantageous properties of DNA. The remainder of the dissertation presents a more “traditional” approach to hierarchical nanoparticle construction, discussing synthesis, stabilization and functionalization of theranostic materials of iron oxide and gold and their combination into novel nanostructures for more efficacious *in vivo* imaging agents. Ultimately, the preferred path between traditional non-traditional methods rests on whether biological selection is more powerful for functionality than rational design, or whether the most efficacious route is a combination thereof.

## **CHAPTER 1:**

### **INTRODUCTION: BIOLOGICAL APPLICATIONS OF NANOPARTICLES FOR CANCER THERAPEUTICS AND DIAGNOSTICS**

#### **1.1 Background**

The field of nanotechnology has taken center stage over the past several years as a burgeoning new discipline with wide ranging applications, the diversity of which are a direct consequence of the multiple disciplines that have converged to form this new field of study. Nanotechnology is fundamentally the manipulation of matter on the nanometer length scale and is commonly more restricted to length scales from the 1-100nm range. The properties of elemental matter on this scale, which may encompass as few as a few dozen atoms are often radically different from the bulk, macroscopic properties of the same materials. These unique properties can be structural (carbon nanotubes/graphene)<sup>1</sup>, photonic (metallic nanoparticle plasmon resonance bands)<sup>2,3</sup>, electric (metallic nanowires, carbon nanotubes)<sup>4-6</sup>, or a host of other properties that naturally define nanotechnology as an intersection of nearly all of the physical sciences including chemistry, physics, and biology. Furthermore, these materials can be combined in unique and specific manners that lend an almost infinite

range of manipulatable properties and lead to higher order functions and characteristics that are often coined as “smart” materials. These new, rationally designed, high functioning materials are forming the foundation of a modern science that is driving irreversibly toward smaller and more powerful applications, with the potential to revolutionize electronics, computing and materials. The increasing command that science has acquired over the natural world has provided nanotechnology some of the most powerful tools to interact with the world on a fundamental level—the atomic level. However, perhaps the most dramatic applications of nanotechnology will be its application to biology<sup>7</sup>. Never before has there been a method of addressing, understanding and actually interacting in a rationally designed manner with biological systems. While larger cells have long been manipulated and studied under a microscope, biology fundamentally operates at the nano-scale, being dominated by proteins, membranes, small molecules, etc, that all reside in the nanometer range. However, what truly separates biology from other applications is that biology can be said to be the only naturally occurring “smart” nanosystem. The last few decades have spawned a plethora of molecular biology tools used to exploit the existing systems such as molecular cloning, genetic engineering and hybridoma technology, among others, however, nanotechnology brings the promise of expanding and enhancing those systems by promoting the idea of being able to rationally design “smart” nanomaterials and devices that hold the potential for much more interesting, complicated and useful interactions that may be considered more as dialogues between the natural and synthetic worlds. Never before has there

been such a powerful platform for probing, testing and ultimately understanding biological systems.

One of the most promising applications of nanotechnology in the biological sciences is in the development of systems and materials that can effectively interact with the human body *in vivo*. It is not too far from science fiction to imagine small autonomous “nanobots” that will monitor, maintain, and regulate biological systems in real time in the body. To begin this process, nanotechnology has been applied extensively to both the fields of *in vivo* drug delivery and imaging, with the most prevalent indication being cancer<sup>8</sup>. The primary reason for this is two-fold: 1) From an imaging perspective, there is a substantial non-linear correlation between survival rate and stage of detection<sup>9</sup> with earlier detection of malignant tumors leading to dramatically increased survival rates, and 2) from a therapeutic perspective, the therapeutics used currently to treat cancer are extremely toxic and generally indiscriminate in their effects with can cause the side effects of therapy to be more devastating than the disease itself<sup>10,11</sup>. Both of these reasons have urged a substantial surge in the focus on “smart” materials that are better at either specifically detecting cancer at earlier stages or delivering therapies in a more efficacious and specific manner so as to spare the damaging side effects to normal tissue.

## **1.2 Imaging/Diagnostics**

A primary focus of nanotechnology is in the development of novel materials that have advantageous properties suitable for one of the major *in vivo* imaging modalities that include Magnetic Resonance Imaging (MRI), Computed Tomography

(CT), Ultrasound Imaging, Positron Emission Tomography (PET) and various forms of optical imaging. Examples of nanotechnological approaches to each of these forms of imaging include:

- Carbon nanotubes utilized for thermoacoustic imaging<sup>12</sup> or as scaffolds for absorbed gadolinium for enhanced MRI contrast agents<sup>13</sup>
- Iron oxide nanoparticles in the superparamagnetic domain are used extensively as MRI contrast agents<sup>14,15</sup> and are commercially available (Ferridex)
- Micro/nanobubbles are used as effective ultrasound contrast agents<sup>16</sup>
- Gold nanoparticles and nanoshells for CT as X-ray contrast agents<sup>17</sup>
- A variety of nanoparticles possess optical properties such as fluorescence resonance energy transfer (FRET) systems<sup>18,19</sup>
- Several of these can be combined such as iron oxide, with Fluorine<sup>18</sup> for combined MR, PET and CT imaging<sup>20</sup>

### 1.3 Therapeutics

A second major *in vivo* directed application of nanotechnology is in the development of efficacious and intelligent methods of delivering therapies specifically to cancer cells. The first generation of this approach was simply to encapsulate currently utilized chemotherapies into a nanoparticle package, typically consisting of a

polymer, liposome, or pelleted protein<sup>21</sup>. A wide range of drugs including doxorubicin, cisplatin and its derivatives, paclitaxol and its derivatives and many others have been utilized in this format and have shown substantial improvements over their free drug counterparts in both *in vitro* and *in vivo* assays<sup>10</sup>. It has been proposed that delivering chemotherapies in a nanoparticle format is advantageous for overcoming drug resistance commonly seen in malignant tumors due to a different method of drug entry into cells—endocytosis over diffusion—that may be able to bypass the common P-glycoprotein drug efflux pumps, though this mechanism is still debated<sup>22,23</sup>. In addition, such platforms consisting of hydrophobic nanoparticles can substantially improve the administration of hydrophobic drugs such as the taxols and relieve the need to inject deleterious organic solvents along with the drugs to keep them soluble<sup>24</sup>.

The emergence of these new nano-platforms has also opened up new potential methods of treating diseases apart from traditional chemotherapies. Gold and iron oxide nanoparticles have been extensively investigated for their ability to selectively heat and destroy tissue under near infrared (NIR) or magnetic stimulation<sup>25</sup>. In particular, hollow nanoshells of gold can be produced with specific and strong plasmon resonance absorbance bands in the 700-900nm range that is most optically transparent to tissue<sup>26</sup>. Absorption at these wavelengths causes local heating that can destroy nearby cells<sup>27</sup>. Similarly, iron oxide nanoparticles can be externally addressed by oscillating magnetic fields and produce a similar heating effect. The ability to externally and specifically address “smart” materials inside the body is one of the major benefits of nanotechnological approaches.

Several enhancements can be made to these nanoparticle constructs that have further improved their performance *in vivo* such as surface modification with tumor specific targeting ligands such as  $\alpha v\beta 3$  to target neo-vascularization<sup>28</sup>, addition of passivating surface groups like poly-ethylene glycol (PEG) which aids in immune evasion and increases circulation lifetime<sup>29</sup>, and chemical modification of particles themselves that allow for variable time or triggered release upon encounter with tumor specific ligands, pH<sup>30</sup>, temperature<sup>31</sup>, or a combination thereof. The combination of these properties into a single particle provides for a flexible and powerful platform for effective delivery of therapeutics that has applications extending beyond cancer. Its power lies in the ability to rationally design where, when, what, and how therapies are delivered in the body.

#### **1.4 Nanoparticle Theranostics**

However, the most unique and powerful property of the “smart” nanoparticle systems being designed for biological applications is the ability to combine both the therapeutic and diagnostic capabilities into a single entity. Such novel constructs have been labeled “nanoparticle theranostics” for their ability to both deliver a treatment and report back in some diagnostic manner on the efficacy of the treatment. This capability underlies the concepts of personalized and predictive medicine. Many of building blocks of bionanotechnology can naturally serve as theranostics such as both iron oxide and gold, which can inherently be used both for imaging and therapy as discussed in previous sections. However, it is more common to increase functionality by adding additional elements such as conjugating/encapsulating drugs to imaging

elements to track their *in vivo* distribution. Additionally, schemes have been designed to image only where therapies are actively released such as a novel aptamer/quantum dot construct that intercalates and quenches doxorubicin in the nucleic acid aptamer close to the quantum dot core via a FRET mechanism, but when released allows both the doxorubicin and quantum dot to fluoresce<sup>19</sup>. A comprehensive review of nanoparticle theranostics to date can have been compiled by Xie *et. al.*<sup>32</sup>

### **1.5 Scope of Dissertation**

The scope of this dissertation is to cover work on both “traditional” and “non-traditional” nanoparticle platforms that may be employed as theranostics. The platforms are so named for both their historical use as nanotechnology materials as well as the novelty of their structural properties. The traditional platform composes the development and characterization of a unique core/hollow shell structure consisting of a superparamagnetic iron oxide core and a porous, hollow gold nanocage, both of which have extensive histories as both functional and structural materials in nanotechnology. The structure is designed to enhance the magnetic resonance potential of the iron oxide by allowing direct interaction with environmental water through the porous gold shell while simultaneously shielding it from cellular surfaces and iron receptors that decrease iron oxide circulation times *in vivo*. The non-traditional nanoparticle platform composes a novel approach to DNA based nanostructures and combines many of the unique biochemical and physical properties of DNA with the power of exponential selection to produce a new class of nanoparticles with inherent biological targeting capabilities coupled to potential for

drug delivery, immune stimulation and imaging properties. This dissertation will discuss the properties and uses of DNA in the context of both structural and functional nanotechnology, as well as the synthesis, properties and applications of iron oxide, gold nanoshells and combinations thereof as potential theranostic agents for utilization in cancer diagnosis and treatment.

## CHAPTER 2:

### DNA NANOPARTICLES AS A THERANOSTIC PLATFORM

#### 2.1 Introduction/Rationale

The multi-functional nanoparticle field for biological applications is naturally a modular field with each separate building block granting a piece of the overall function. This paradigm is oriented around the framework of bottom-up construction. Generally, a scaffold of polymer, metal, lipid or other molecular structure serves as a basis for the addition of functional moieties to lend the nanomaterial the desired capabilities such as selective targeting, transport of therapeutic and imaging agents, and immune evasion<sup>8</sup>. This is a powerful platform for constructing complex structures with multiple functions, but poses difficult hurdles from both a synthetic and regulatory perspective as the complexity and diversity increases. Difficulties in maintaining stability, homogeneity and reproducibility increase dramatically with each novel addition to a nanoparticle platform and create challenges in synthesis that may preclude the precise definition and characterization required for regulatory purposes. For this reason, it becomes desirable to look for nanoparticle platforms that are more holistic in a sense, where several single function elements are not combined together

in a complex structure, but rather few core elements possess several inherent functionalities.

In the past 20 years, deoxyribonucleic acid (DNA) has been recognized as a rising candidate in this multifunctional arena. Much more than just a genetic information carrier, DNA has been observed to demonstrate a unique complement of overlapping biochemical, structural, and functional activities, particularly when compared to other standard polymers typically used in nanoparticle synthesis. The development of the process of Systematic Evolution of Ligands by Exponential Enrichment (SELEX) from the Tuerk and Gold labs in 1990 paved the way for DNA to be used as molecular recognition tools with affinities rivaling antibodies and even develop enzymatic properties as aptazymes or ribozymes<sup>33</sup>. In addition, DNA has been observed to be a strong immune stimulator through unmethylated CpG motifs<sup>34</sup> that are characteristic of DNA from non-human origin. These unmethylated CpG motifs are known to interact strongly with TLR9 receptors in immune cells as a defense mechanism against viral and bacterial infection<sup>35</sup>. From a structural perspective, the highly specific hybridization characteristics of DNA allow it to serve as a scaffold for the directed hybridization of oligonucleotide conjugates, and be easily chemically modified to allow small molecule or metal ion attachment which can serve as nucleation sites for direct metal deposition<sup>36</sup> and utilized for imaging. From a chemotherapeutic perspective, it is a natural carrier of many chemotherapeutic drugs such as cisplatin and doxorubicin whose mechanism of action is to bind DNA and prevent cell replication. And lastly, DNA is one of the most studied, understood and characterized molecules in biology and has a long clinical history of favorable toxicity

and biodegradability profiles<sup>37</sup>. When compared to monoclonal antibodies, which have long been the primary tool for biomolecular recognition both *in vitro* and *in vivo* but suffer from general immunogenicity of non-human versions and immune clearance of nanoparticle aggregated humanized versions, DNA as a recognition molecule becomes very appealing.

For each of these reasons, DNA has become an attractive addition to the nanoparticle tool kit. In many cases, the double helix structure is used as a rigid structural backbone for rationally designed geometric structures giving rise to an entire field of study of DNA origami<sup>38</sup>, however, the double stranded form of DNA is relatively uninteresting from a functional perspective. In contrast, single stranded DNA (ssDNA) is able to adopt much more diverse and complex structures through a liberated and flexible sugar phosphate backbone and the ability to internally self-hybridize forming unique three dimensional structures. In addition, this rigid structural approach of utilizing double stranded DNA as a scaffold has overlooked a fundamentally powerful tool of molecular biology, namely the ability to exponentially amplify DNA in rapid and reproducible manners using the polymerase chain reaction (PCR). This capability is extremely unique to DNA. Combined with cheap, simple and reproducible DNA synthesis, it gives rise to the simple creation and efficient combing of nucleic acid libraries with diversity of  $10^9$  or more utilizing the SELEX process<sup>39-41</sup>. This process has fundamentally revolutionized the perspective of DNA as a useful biomolecule and spawned a new field of molecules called aptamers.

## 2.2 Systematic Evolution of Ligands by Exponential Enrichment (SELEX) and Aptamers

The SELEX process developed in the Tuerk and Gold<sup>33</sup> labs is simple and powerful. The process can be seen visually in Figure 1.

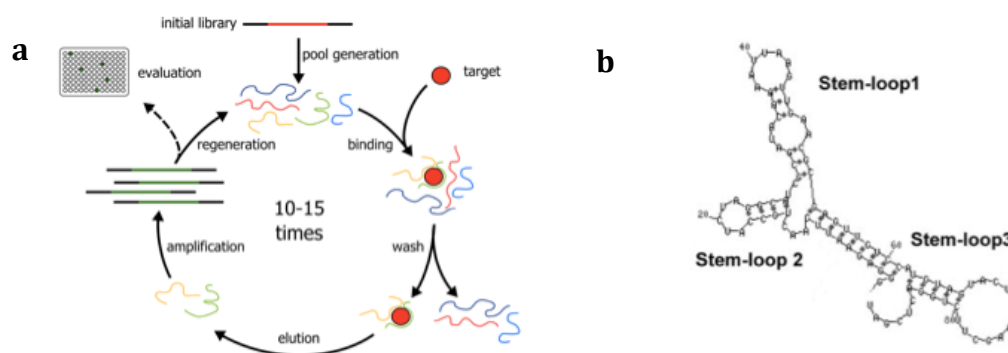


**Figure 1: Systematic Evolution of Ligands by Exponential Enrichment.** The cyclic process begins with a library of random ssDNA sequences ~20-40 bases long and flanked by fixed PCR priming sites. The library is incubated with a binding target, washed, and eluted sequences are amplified by PCR. The single library strands are regenerated and the process is repeated<sup>42</sup> (a). A prototypical example of a ssDNA aptamer produced from the SELEX process showing the canonical stem-loop structures and complex folding geometries that give rise to specific recognition properties<sup>43</sup> (b).

Random libraries of short single stranded nucleic acid sequences (ssDNA) (~20-50bases) are produced with universal PCR priming sites on the 3' and 5' ends. Sequences in these libraries internally hybridize into a diverse array of three dimensional structures, an example of which can be seen in Figure 1. The library is then mixed with a target of choice, washed, and structures that possess affinity and remain bound are amplified by PCR, followed by a regeneration of the single stranded library and subsequent repeat of target binding. Each cycle enriches for sequences that have greater affinity resulting in high affinity ssDNA ligands that can rival

antibody affinities<sup>44</sup>. A general aptameric structure will take on several stem loops as seen in the example Figure 1 where recognition sites exist in the loop regions.

The most common application of aptamers in nanotechnology is as recognition elements that decorate a solid nanoparticle surface and act as targeting elements<sup>45</sup>. However, there is a fundamental mistranslation in this process. Extremely high affinity aptamers can be selected using the SELEX process in a *monovalent* manner. When these ligands are conjugated in a *multivalent* manner on a nanoparticle, the affinity of one ligand can be compromised by the avidity of many. As shown in

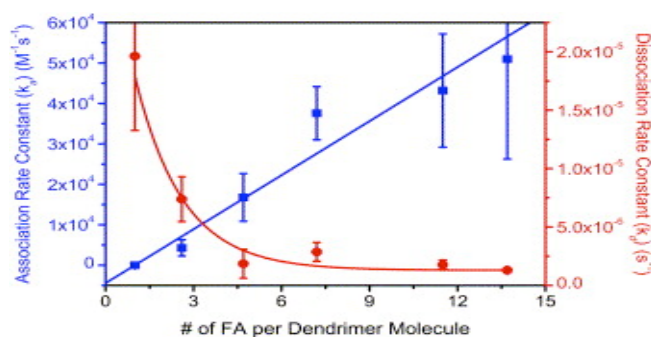


**Figure 2: Binding constants of multivalent structures.** Folic acid molecules conjugated in geometrically well-defined positions to the ends of dendrimers. Association and dissociation constants show log linear association increase but double exponential dissociation decrease assumed a “Velcro” effect of several weak interactions leading to a strong overall bond<sup>46</sup>.

Figure 2, which plots the kinetic constants of a dendrimer with various numbers of folic acid molecules attached, it was observed that the increase in affinity was relatively log linear with respect to ligand number, but the dissociation of the multivalent molecules falls precipitously with just few ligands. The effect of multiple ligands on dissociation is similar to Velcro, where many weak interactions work in conjunction to provide an overall strong bond. From a nanoparticle perspective with

targeting ligands selected in a monovalent format, the increase in avidity can substantially decrease the dissociation of even weak interactions and consequently compromise the highly specific properties of monovalent aptamers and overall nanoparticle targeting.

For this reason, we proposed to develop a modified selection protocol in which the nanoparticle itself, composed entirely of DNA was the element of selection, such that the product of the selection would exist in the same format as the ultimate desired usage. To begin, we first needed understand how to make nanoparticles out of DNA.

## 2.3 DNA Nanoparticles

**Table 1: Oligonucleotide Sequences For DNA Nanoparticle Preparation.**

Complete oligonucleotide sequences for DNA nanoparticle characterization and library screening and results. The (\*) indicates phosphorothioate bonds between bases. Phos indicated a free phosphate end. Bold bases represent PCR priming sites used to amplify the selected library sequences after each selection round.

	<b>Table 1: DNA Nanoparticle Template Sequences</b>
<b>Clone 3</b>	<b>5'GCGCGGTACATTTGCTGGACTATGCATGTTTCGTAGT TATATAGGGGGATTGTTTGATAGTCGGAACCGCTGTGCT CAAAGTTTGGAGGTTGGGGATTTGATGTTG 3'</b>
<b>Clone 4</b>	<b>5'GCGCGGTACATTTGCTGGACTATCGGATAACATCGG GGGCCGAGACCTAGTAAGGATGCAAGTAGAAAAGCTT GGAGGTTGGGGATTTGATGTTG 3'</b>
<b>Clone 10</b>	<b>5'GCGCGGTACATTTGCTGGACTAGTGTTGTGAGGGTG CGTATCAGGTCGTAGAATGCAAAACAGCGGTGAGTAAA TTTGTGTCTGGAGGTTGGGGATTTGATGTTG 3'</b>
<b>Clone 12</b>	<b>5'GCGCGGTACATTTGCTGGACTAAAACACTTAATTAA TCAACGGTACGCCTGCCTATTCTGACGCTTCCCTGATG TAGGTGATGGAGGTTGGGGATTTGATGTTG 3'</b>
<b>pphDCCpGv1 +K3CpG</b>	<b>5' Phos-GGT TCA TGC CGC CCG CGA GAA CGC TCG AGA GTC GAT AGC AAA ACG ACA AAA CGA CGA CCC TAT AGT GAG TCG TAT TAG GTG AGG ATG GGC CTC C 3'</b>
<b>pphDCCpGv1 +K3 CpG linking primer</b>	5' GGG CGG CAT GAA CCG GAG GCC CAT CCT CAC C 3'
<b>V6 library</b>	<b>/5Phos/GCG CGG TAC ATT TGC TGG ACT ANN NNN NNN NNN NNN NNN NNN NNN NNN NNN NNN NNN NNN NNN NNN NNN NNN NNN NNN NTG GAG GTT GGG GAT TTG ATG TTG 3'</b>
<b>V6 linking primer</b>	5' TCC AGC AAA TGT ACC GCG CCA ACA TCA AAT CCC CAA CCT 3'
<b>V6 linking primer added T</b>	5' TCC AGC AAA TGT ACC GCG CTC AAC ATC AAA TCC CCA ACC T 3'
<b>V6F</b>	5'Phos-G*C*G* CGG TAC ATT TGC TGG ACT A 3'
<b>V6B</b>	5' CAA CAT CAA ATC CCC AAC CTC CA 3'

## 2.4 Synthesis of DNA Nanoparticles

Double stranded DNA exists in a very rigid double helical structure governed by strict base pairing rules. Single stranded DNA (ssDNA), however, is substantially more flexible. ssDNA has a persistence length of  $\sim 3\text{nm}$ <sup>47</sup> which allows it to rapidly fold in three dimensional space and hybridize internally to itself. Therefore, in order to make condensed DNA nanoparticles, we needed to generate long sequences of ssDNA. Additionally, to have multivalent aptameric surface, in which a binding sequence is displayed several times across the surface of the particle, the sequences needed to be concatemeric repeats. The production of long, concatemeric ssDNA is achieved by a linear amplification called Rolling Circle Amplification (RCA), which begins with a circular ssDNA template and utilizes a strand displacing polymerase ( $\phi$ 29 DNA Polymerase) to synthesize and spin off the concatemeric single stranded complement strand. As this long ssDNA strand is produced, it rapidly fold and self hybridizes into a condensed particulate. RCA is visually described in Figure 3.

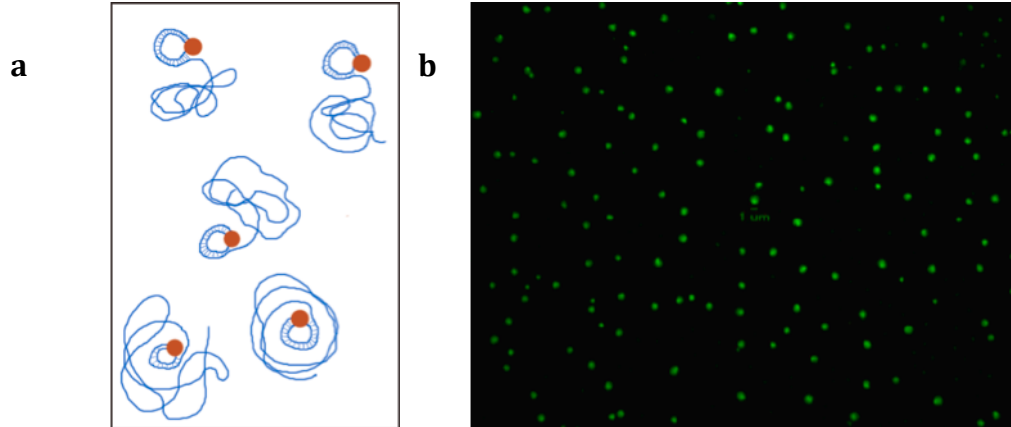


**Figure 3: Rolling Circle Amplification and Fluorescent Microscopy of DNA Nanoparticles.** Cartoon illustrating the process of Rolling Circle Amplification (RCA) showing the circular ssDNA template, strand-displacing polymerase (red) and ssDNA product **(a)**. Fluorescent Microscopy image of DNA nanoparticles stained with SYBR Green dye showing the discrete nature of the particles. Note the scale bar in the center of the image is 1mm, however visualized particles are fluorescent light cones and not accurate determinants of particle size. This image is to display their discrete particulate nature **(b)**.

The products of the reaction are visually seen as discrete particles when stained with the DNA binding dye SYBR under a fluorescent microscope—note that the size is not an accurate measurement because the fluorescent light cone seen in the microscope does not resolve the particles. The discrete, particulate nature of long ssDNA strand has also been observed by Jarvius *et. al.*<sup>48</sup>

## 2.5 Size Characterization—Estimations and Limitations

### 2.5.1 Dynamic Light Scattering

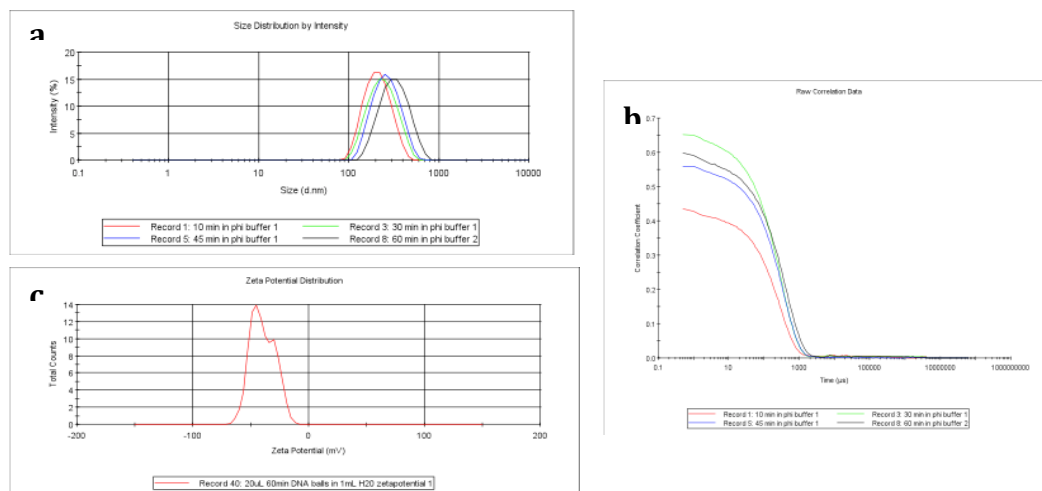


**Figure 4: Dynamic Light Scattering (DLS) Results of DNA Nanoparticles.** DLS results of DNA nanoparticles produced with RCA template sequence pphDCCpGv1+K3CpG for 10, 30, 45, and 60 minute reaction times. Size distributions based on intensity **(a)** and corresponding correlation curves **(b)**. Zeta potential is measured at -39mV **(c)**.

The particles are characterized by Dynamic Light Scattering (DLS) and there is observed control over the size of the particles based on reaction time with reaction times from 10–60 min having hydrodynamic radii between 217 and 338 nm with polydispersity indices of .228–.333. The DLS results can be seen visually in Figure 4 with complete data in Table 2.

**Table 2: Dynamic Light Scattering (DLS) Results of DNA Nanoparticles.**  
Numerical results corresponding to plots in Figure 4.

Sample Name	T(C)	Z-Ave d.nm	PdI	Pk 1 Mean Int d.nm	Pk 2 Mean Int d.nm	Intercept	Volume Ratio
<b>10 min</b>	25	173.1	0.228	217	0	0.645	1
<b>30 min</b>	25.1	181.3	0.313	248.6	0	0.8	1.5
<b>45 min</b>	25	211.4	0.259	273.9	0	0.744	1.99
<b>60 min</b>	24.9	240.2	0.333	338.3	0	0.761	3.77

To generate this data, DNA nanoparticles were produced with template probe sequence pphDCCpGv1+K3CpG for reaction times of 10, 30, 45, and 60 minutes (see DNA nanoparticle synthesis protocol for details). Reactions were stopped by heat inactivation of phi29 DNA polymerase by incubation for 10 minutes at 65°C and immediately measured by DLS. For a monodisperse sample the autocorrelation plots (Figure 4) should show a single exponential decay, the exponent coefficient of which is known as the first moment and is used to calculate a Z-average size. The second moment is used to calculate the deviation from monodisperse and is known as the polydispersity index (PdI), which is a measure of relative peak width of the Gaussian size distribution based on scattering intensity. In general if the PdI is greater than 0.25 it is recommended to use a secondary algorithm called Non-Negative Least Squares (NNLS) which models the autocorrelation curve as a contribution of several size samples and extracts individual peak data (Peak 1 Mean Int d.nm). Results indicate that there is only one intensity peak, however because of slightly different mathematics, the Z-average and the NNLS calculations will produce different average sizes. It is important to note that the definition of nanoparticle size for condensed

DNA is a very fluid concept and is useful only for comparison between different batches and different reaction time points. The assumptions made in any DLS calculations are based on solid sphere scattering and makes use of the Stokes-Einstein equation to relate an estimated diffusion coefficient to a hydrodynamic radius. Volume ratios are calculated from peak mean diameter ratios and are expected to grow linearly as the reaction proceeds (if the reaction is continuously linear, equal synthesis rates should grow volume at a linear rate). Linear regression on time vs. volume ratio gives  $Y = .052X + .176$ , where Y represents the volume ratio and X the time in minutes. Therefore at  $X=0$  one could extrapolate the diameter to be 121nm. This is, of course, not feasible before RCA occurs, but it is of note that there is probably a lower limit to the particle nature of a DNA condensate under which it does not take a stable conformation. Even though the persistence length of ssDNA is only 3nm (~5 bases), higher order structures may still be in significant conformation flux up to a certain point and not register consistent scatter signals. Molecular modeling of concatemers indicates that the concatemer is not simply a repeat of a monomer unit motif but achieves much more complex formations as the sequence grows. Four potential conformations can be seen in Figure 5.

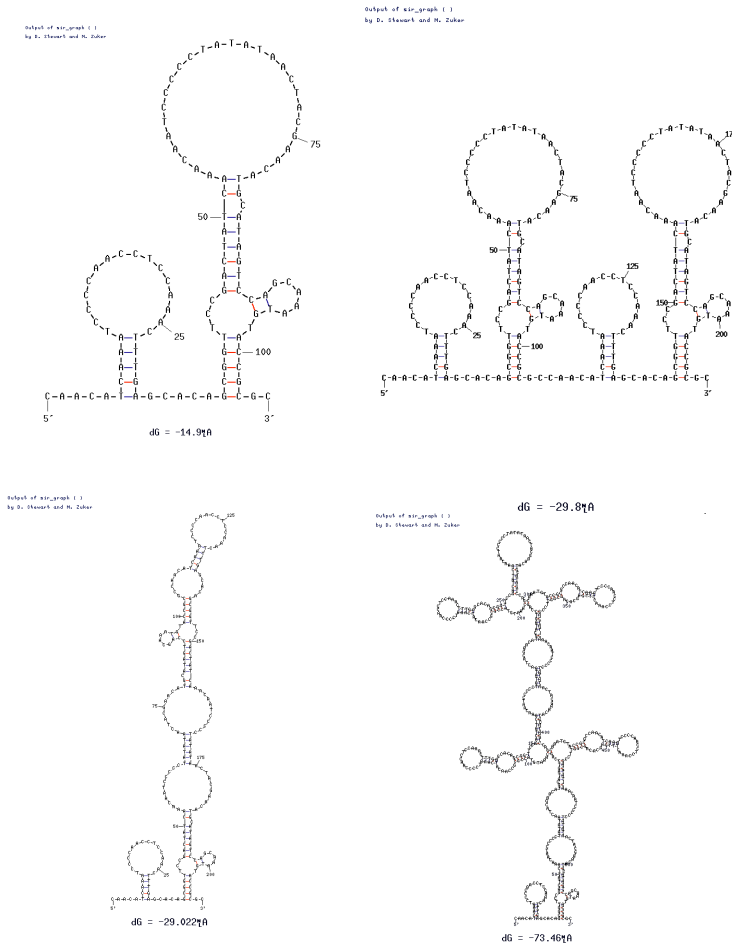


**Figure 5: Theoretical Model of Clone 3 Nanoparticle Sequence (reverse complement of template sequence listed Table 1).** Computational DNA modeling showing predicted structures of concatemeric sequences in phosphate buffered saline (PBS). All structure predictions made using The DINAmelt server from Rensselaer found at <http://dinamelt.bioinfo.rpi.edu/quikfold.php> using a linear template and temperature at 4C, Na<sup>+</sup> concentration at 137mM and Mg<sup>2+</sup> concentration at 0mM. **(a)** Unit monomer. **(b)** One possible predicted structure created by a concatemer of 2 unit monomers showing a simple motif repeat. **(c)** Secondary predicted structure of 2 unit monomer repeat showing potential for interactions of nucleotides distant in sequence space and higher order structures. **(d)** Concatemer repeat of 5 unit monomer with both higher order structures and conserved motifs.

### 2.5.2 Ideal Chain Polymer Model

The polymerization rate of phi29 DNA Polymerase is ~1kb/min, consequently a 60 minute reaction time would have an estimated length of 60kb. It is of note that

DLS measurements make several assumptions such as sphericity and a solid scattering

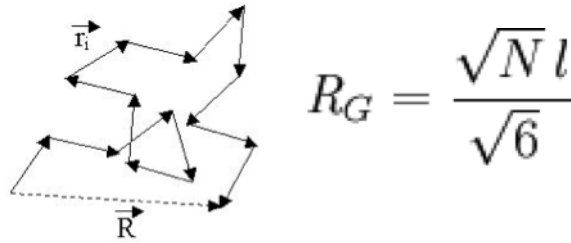


**Figure 6: Ideal Chain Polymer Model.** Diagram of ideal chain model and equation defining the radius of gyration ( $R_G$ ) for estimation of DNA nanoparticle size.  $N$  is the number of rigid chain units (calculated by dividing total estimated length by ssDNA persistence length) and  $l$  is the length of each unit, known as the Kuhn Length.

surface that may not apply to DNA particles. However, an ideal chain model is the best approximation of ssDNA from polymer theory. It assumes a polymer as a random walk and neglects any kind of interactions among monomers. This is not precisely accurate for ssDNA which possesses both base attraction and backbone repulsion. In this situation the radius of gyration is defined by Figure 6 where  $N$  is the number of “rigid chains” and  $l$  is the length of each chain (Kuhn Length), defined as two times the persistence length of each segment. With a ssDNA persistence length of 3nm and base-base distance in ssDNA at  $\sim 0.6$ nm, there are 5 bases per persistence length and 10 bases in each chain of Kuhn length 6nm. The radius of gyration for a 60 minute RCA nanoparticle with estimated length of 60kb is then 189nm or a hydrodynamic diameter of 379nm, which is in close agreement with DLS measurements. It is also of note, that it was difficult to effectively measure/produce the size of DNA nanoparticles below a certain size. This is likely the result of insufficient scattering due to incomplete condensation or insufficient material in each particle. Because of their large size and chaotic single stranded structure, the particles

will not migrate in an agarose gel. This method of production can be used to make DNA nanoparticles using any circular template sequence and will produce concatemeric, condensed particulates of DNA. For subsequent library screenings, the template sequences were composed of a random region flanked by PCR priming sites on either side.

## **2.6 Protocol for Generating DNA Nanoparticles and Nanoparticle Libraries**

Anneal v6 linking primer to v6 library. Mix 5  $\mu\text{L}$  T4 Ligase 10X buffer, .5  $\mu\text{L}$  v6 library (10 $\mu\text{M}$ ) to a final concentration of 100nM, 1.5  $\mu\text{L}$  v6 linking primer to a final concentration 300nM, 42  $\mu\text{L}$  water. In a thermoblock heat sample to 95C for 2min and cool to 25C at .1C/sec. To the sample add 1  $\mu\text{L}$  T4 Ligase (400 units). Incubate at RT for 30 min. Add 1 $\mu\text{L}$  Exonuclease 1 and incubate at 37C for 40 min followed by 80C for 20min. RCA proceeds as follows: Mix 5  $\mu\text{L}$  10X Phi29 buffer, 3  $\mu\text{L}$  10mM dNTPs (2.5mM each), .5  $\mu\text{L}$  DTT (500mM), .5  $\mu\text{L}$  of ligated DNA from the above reaction (final conc. 1nM), .5  $\mu\text{L}$  Phi29 polymerase (5 units), 40.375  $\mu\text{L}$  H<sub>2</sub>O. Perform reaction for 30 minutes at 30C, terminate by heat inactivation of the polymerase at 65C for 10 minutes.

## 2.7 Exponential Enrichment—Modified SELEX

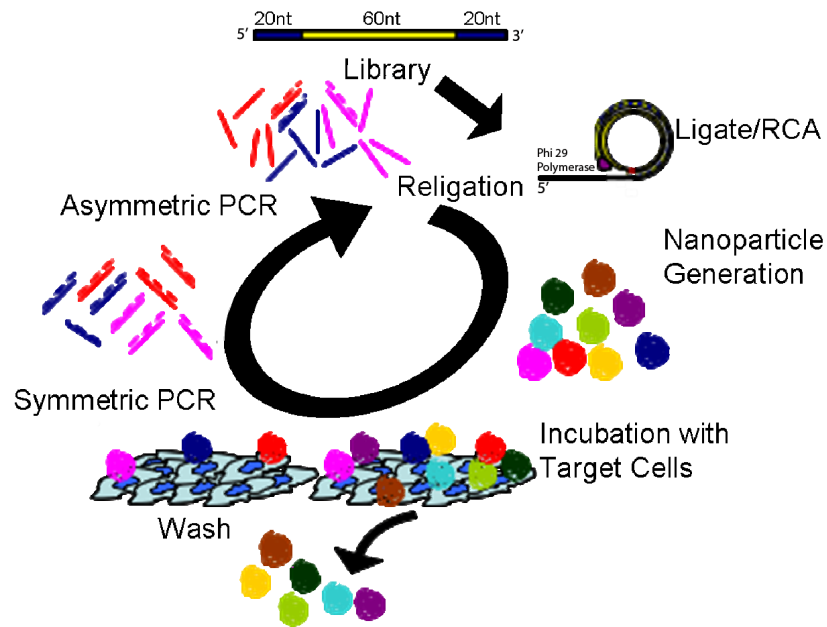


**Figure 7: DNA Nanoparticle Selection Scheme.** The selection design for DNA nanoparticles executes an exponential enrichment of full DNA nanoparticles. An initial random library is circularized and serves as a template for RCA to produce a library of DNA nanoparticles. The nanoparticle library is incubated with a binding target, washed and amplified with PCR. To regenerate the desired template strands, asymmetric PCR is used to enrich the desired strand. This strand is then re-circularized and serves as a template for RCA and the production of a new enriched nanoparticle pool. Phi29 DNA polymerase used for RCA also possesses 3’-5’ exonuclease activity that ensures that ancillary and excess DNA (from PCR) is digested and does not interfere with subsequent selection steps.

The selective enrichment of DNA nanoparticles requires several modifications to the SELEX protocol but is rooted in the same idea of exponential enrichment. A summary can be seen in Figure 7. The protocol begins with a library of random nucleic acid sequences flanked by PCR primers. From this, DNA nanoparticle generation occurs, followed by incubation and washing. PCR amplifies the sequences (note here that this should be a very sensitive assay as just one concatemeric particle

that would bind would be able to provide several hundred PCR templates). The symmetric PCR is followed by asymmetric PCR that is used to generate the desired library strand and the process is repeated. The phi29 DNA polymerase used in the RCA step to produce the new nanoparticle pool has the benefit of possessing 3'-5' exonuclease activity that ensures that excess DNA from the PCR step does not interfere with future selection steps, while not damaging the circularized DNA or the long ssDNA nanoparticle produced (only one end per particle makes exonucleases relatively ineffective). Only template strands that have been ligated and circularized are resistant to this exonuclease and will survive to subsequent binding steps.

Human dendritic cells (DCs), as the gatekeepers of the immune system, were chosen as the primary selection target with an eye toward immediate incorporation into the immunostimulatory properties of unmethylated CpG sequences in DNA. In addition human dendritic cells have the advantage that they are not created from a cell line, but rather generated from fresh donors weekly. This circumvents the possibility of selecting for some possible idiosyncrasies of a cell line. Once selective DNA nanoparticles are obtained, it would be a natural addition to begin addressing the immune system.

## **2.8 Modified Selection Protocol**

Peripheral blood mononuclear cells (PBMCs) were isolated from the blood of normal volunteers (San Diego Blood Bank) over a Ficoll-Hypaque (Amersham Biosciences, Uppsala, Sweden) density gradient. To generate DCs, PBMCs were allowed to adhere to culture plates for 1h. The non-adherent cells were washed off and

the adherent cells were cultured in RPMI 1640 medium supplemented with 2 mM L-glutamine (GIBCO-BRL Life Technologies; Grand Island, NY, USA), 50 mM 2-mercaptoethanol (Sigma, St. Louis, MO, USA), 10 mM HEPES (GIBCO-BRL), penicillin (100 U/ml), streptomycin (100mg/mL) (GIBCO-BRL) and 5% human AB serum (Gemini Bio Products West Sacramento, CA, USA), supplemented with 1000 U GM-CSF/ml (Cardinal Health, Dublin, OH, USA) and 200U IL-4/ml (R&D Systems, Minneapolis, MN ) at days 0, 2, and 4. Immature DCs were harvested on days 5-7.

DNA nanoparticles created from v6 library were produced using v6 linking primer in the first round and v6 linking primer added T in the later rounds. The latter was used for later round ligations to accommodate the nonspecific adenosine nucleotide that Taq polymerase often adds to the end of extension products. For the selection rounds, RCA was terminated by the addition of 5ul 500mM EDTA in place of heat inactivation.  $10^5$  DC cells were aliquoted and stored on ice for 10-15 minutes. Nearly all media was drawn off and 50uL of the EDTA inactivated RCA reaction was added to the cell and incubated for 1 hour on ice. Cells were washed 4X by pelleting for 3 minutes at 3000RPM in a microfuge, removing supernatant and adding 1mL of PBS with 5% BSA. After each resuspension, cells were transferred to a new tube that had been coated overnight with 5% BSA in PBS to reduce potential plastic binders. After 4<sup>th</sup> wash, cells were suspended in 50uL PCR buffer (10 mM KCl, 10 mM Tris-HCl, 5mM MgCl<sub>2</sub> pH 8.3) with 250  $\mu$ M each dNTP (Applied Biosystems), 200nM v6B, 200nM v6F protected phosphate, 2X SYBR Green (Life Technologies Corporation), and 5 units of AmpliTaq® DNA Polymerase, Stoffel Fragment (Applied Biosystems). QPCR was run 95C for 2 minutes, then cycle 95C 30 seconds, 61C 1 minute, 72C 20

seconds, until PCR is complete by SYBR Green signal. 30  $\mu\text{L}$  of each round was frozen at  $-20\text{C}$  for reference. 15  $\mu\text{L}$  was removed and run in a 2.5% precast Gel Red (Biotium, Hayward, CA, USA) agarose gel at 86V for 80 minutes. To the remaining 5  $\mu\text{L}$  was added 45  $\mu\text{L}$  of PCR buffer with dNTPs as above and 400nM v6F protected phosphate, no v6B was added. 10 additional cycles of PCR were repeated to generate an excess of the desired single strand. Samples were then cleaned using QIAquick Nucleotide Removal Kit (Qiagen, Valencia, CA, USA) and eluted into 43  $\mu\text{L}$  5mM Tris-Cl pH 8.5. To this was added 5  $\mu\text{L}$  10X T4 DNA Ligase Buffer and 300nM v6 linking primer added T, sample was re-annealed, ligated and amplified by RCA. Nine rounds were produced after which sequences were cloned (P-GEM, Promega)

## **2.9 Human Dendritic Cell Selection Results**

Initial selection protocols were carried out against human dendritic cells. Nine rounds of selection were performed, after which the selected DNA nanoparticle population was labeled by incorporation of fluorescent Alexa488 OBEA-dCTPs and the binding to dendritic cells evaluated by flow cytometry and microscopy. A random clone from the unselected library was used as a negative control. Each round of enrichment possesses a population of potential candidate sequences so several population members from the 9<sup>th</sup> round of selection were cloned, sequenced, and regenerated with fluorescent nucleotides. The sequenced clones are seen in Table 1 (Clones 3, 4, 10, 12) and their fluorescent binding can be seen in Figure 8.

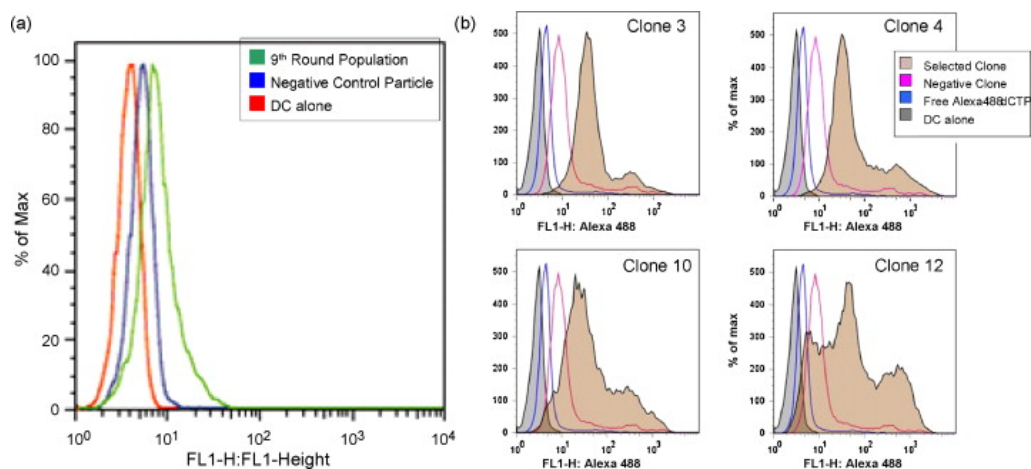


**Figure 8: Fluorescent Flow Cytometry Data From Dendritic Cell Selection.**

Human dendritic cell binding of whole library populations before and after enrichment generated using fluorescent dCTP nucleotides incorporated into DNA nanoparticles (a). Fluorescent flow cytometry data of specific selected clones from the enriched 9<sup>th</sup> round selection pool (b).

There are a several things to note in these results. First, there is an increase in the net binding ability (as measured by fluorescence) of the enriched 9<sup>th</sup> round pool as compared to a random clone from the unselected library and dendritic cells alone. The shift is smaller than may be expected from several rounds of enrichment, however, it is a general population average and the incorporation efficiency of Alexa488 OB EA-dCTPs by phi29 DNA polymerase was calculated to be ~1.5% so there are very few labeled fluorescent labels per DNA nanoparticle resulting in lower signals to noise (auto-fluorescence). The isolated clones, however, exhibit much greater signal enhancements as compared to both free Alexa488 OB EA-dCTPs (as a control for nonspecific solution uptake), and an unselected clone. All of the clones exhibit a form of bimodal distribution that is even seen to a lesser extent in the unselected clone. It is possible that the particular dendritic cells used for this binding assay were composed

of a slightly heterogeneous population because this same effect was not seen in every future case. For future experiments Clone 3 was selected as the primary scaffold because it appeared to have the cleanest binding profile.

### **2.9.1 Specificity**

In general, enrichment protocols are efficient at generating high affinity ligands, however, there is no guarantee of specificity. This can be particularly challenging when performing a selection against a complex target such as a cell with many specific and non-specific surface features. In phage display, for example, it may be common that peptides with many cationic amino acids are preferentially selected to bind against the negatively charged cell surface. It may be a high affinity interaction, but is not specific to the target of choice. To obtain specific ligands, it is most often necessary to perform negative selection steps, which deplete the population of generic binding elements before exposing it to the desired target. In order to determine the level of specificity of our DNA nanoparticle selection protocol, we performed binding assays against several other cell lines, particularly in the immune lineage. Mouse mastocytoma P815, human monocytic and myelogenous leukemia THP1 and K562 and primary human chronic lymphocytic leukemia (CLL) cells were all tested. Flow cytometry and fluorescent microscopy data for P815 and THP1 cells as compared to dendritic cells (DCs) are seen in Figure 9, and fluorescent flow cytometry data for K562 and CLL cells can be seen in Figure 10. The selected Clone 3 sequence and its complement (which should not bind) were used as the positive and negative samples respectively.

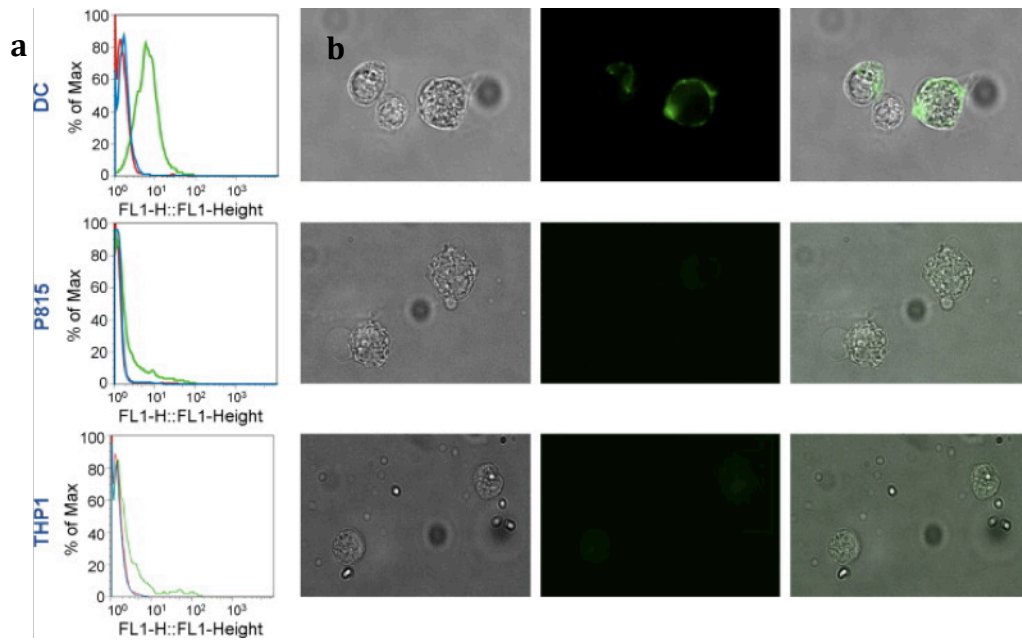


**Figure 9: DC Specific Binding by Clone 3 DNA Nanoparticle.** Clone 3 particles were generated with incorporated fluorescent nucleotides and evaluated for binding to DCs as well as P815 and THP1 cell lines by flow cytometry and fluorescent microscopy. For each flow cytometry plot, the cells with the labeled Clone 3 particles are shown in green, a control particle that is made from the complementary sequence of Clone 3 is shown in blue, and the cells alone are indicated by the red curve (a). Microscopy images show bright field, fluorescent and overlays (from left to right) of fixed cells incubated on ice with the labeled Clone 3 particles. Cells were washed three times before imaging. Fluorescent staining was seen only on the DCs. The complementary control particles did not produce any fluorescent labeling in microscopy images (b).

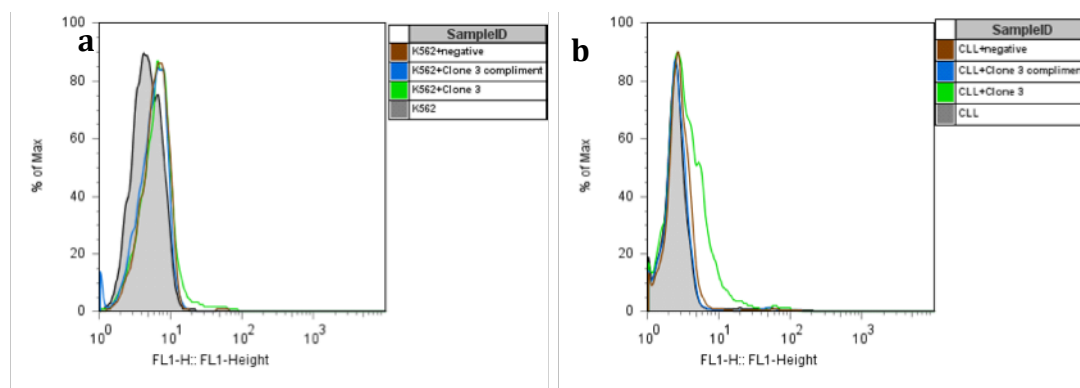


**Figure 10: Fluorescence Flow Cytometry Data Showing Clone 3 Specificity Against K562 (a) and Primary Human CLL cells (b).** DNA nanoparticles were produced using an unselected clone from the v6 library, Clone 3 sequence and Clone 3 reverse complement as the circular DNA nanoparticle generating sequence. Clone 3 has no specificity for either cell line over its reverse complement or an unselected DNA nanoparticle.

In this case, it is interesting to note that we appear to have achieved a large degree of specificity without performing negative selection steps. This is actually a slightly surprising result as it may be conjectured that these types of nanoparticles would suffer from the same avidity issues that compromise the specificity of aptamers conjugated in mass to the surface of nanoparticles. However this does not appear to be the case for this particular selection. The reasons for this are unknown, though it is of note that DC cell binding could be completely abrogated by incubation of the nanoparticles with oligonucleotides that hybridize to the selected random regions, though hybridizing a smaller oligonucleotide to the PCR priming flanking sequence did not affect the DC binding as seen in Figure 11. This suggests that the binding is a consequence of the single stranded nature (and not general charge attraction) of the particle, presumably due to specific secondary structure and that cell specificity is encoded in that sequence. It may also be the case that the result is simply a

consequence of binding different sized oligos to the nanoparticles, with the random sequence binding region being substantially longer than the priming sites.

### **2.9.2 Retention/Abrogation of Binding Activity**

DNA nanoparticles appear to bind via sequence specific mechanisms that can be eliminated by selective hybridization as seen in Figure 11. Fluorescent DNA nanoparticles were incubated with increasing amounts of either the entire complementary sequence to the nanoparticle concatemer random region or a short 20mer sequence complementary to a priming site on the nanoparticles to determine if binding was affected. Note that Clone 3 serves as the nanoparticle templating sequence which produces a nanoparticle with a sequence concatemer consisting of the complement sequence of Clone 3 such that Clone 3 itself is thus complementary to the nanoparticle.

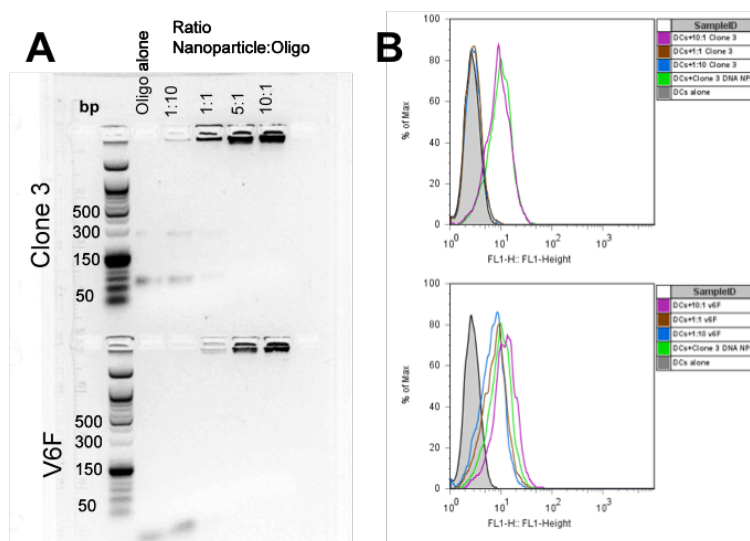


**Figure 11: Abrogation/Retention of DNA Nanoparticle Binding Characteristics By Selective Hybridization.** To determine hybridization efficiency of each of the sequences to the DNA nanoparticles, a gel shift assay was used. Each respective oligo concentration was kept constant at 50ng and increasing nanoparticle concentration was added in varying mass ratios as indicated in the gel where ratios indicate mass of nanoparticle to oligo. Near complete hybridization of each oligo was seen at mass ratios of 1:1 in both cases as seen by the disappearance of the free oligo band in the gel (a). Flow analysis of each of the hybridized constructs showing the effect of hybridizing oligos either in the random or the fixed priming region. Hybridizing the short PCR priming oligo in the lower graph does not appear to have any affect on nanoparticle binding at any concentration whereas hybridization of the larger complement sequence completely abrogates binding at a certain concentration (b).

When hybridizing Clone 3 to the nanoparticles, binding was only seen when the nanoparticle sequence was in 10 fold excess to the hybridizing oligo such that there were still free binding sites on the nanoparticles. When Clone 3 was in equal or greater concentration, the binding is completely eliminated as it can hybridize to all potential binding sites. There was very little effect on binding when hybridizing the 20mer v6F primer to the nanoparticles. This verifies that the key binding characteristics lie in the random region that was selected for and that we can then

hybridize various payloads to the nanoparticles without disrupting their binding characteristics.

## **2.10 Effects of Library Size and Random Region Length on Folding and Sequence Space**

In any exponential enrichment protocol, there are two major determinants that will determine the success of the selection: 1) the total number of unique sequences that enter the selection in the first round and 2) the size of the random region of each sequence—the key issue of both being the size of the sequence space that is being sampled in the initial round. A random region of length  $N$  has  $4^N$  possible sequences. From a practical standpoint, general aptamer selections are done with initial libraries in the range of  $10^{14}$  different sequences. Therefore, selecting a random region of  $\sim 23$  bases will allow each library element to exist in only one copy in the initial round. However, the major key element for aptameric selection is the *shape space*—or the number of conformations that a sequence can assume giving rise to its binding characteristics. Molecular modeling (such as that seen in Figure 5) would indicate that for short oligonucleotide sequences (<50 bases) there is often a favored thermodynamic structure that is achieved and in many aptamer selections, an initial step is to melt and slowly cool the library pool such that each sequence can find this global minimum and fold consistently from round to round. As seen in Figure 5, however, molecular modeling of long ssDNA sequence can rapidly become quite complex (albeit its consistency is assisted by the concatemeric nature of the

sequences) and it is quite possible that there are many local minima that DNA nanoparticles can assume from round to round. Initial tests to melt and cool DNA

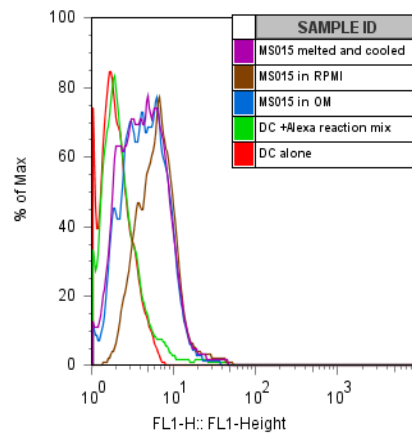


**Figure 12: Effect of Melting and Cooling DNA Nanoparticles.** DC binding DNA nanoparticles are assayed for binding activity in RPMI and original DC media (OM) before/after being heated to 95C and cooled slowly (MS015 is the same sequence as Clone 3)

nanoparticles in order to achieve a consistent low energy state show that there is an effect on binding efficiency (Figure 12), however repeated binding assays done over several different DNA nanoparticle preparations continue to show consistent binding profiles indicating that there is some consistency in folding or surface features that is unique to the selected sequences under the synthetic and binding conditions employed. This gives us confidence that the sequences selected are indeed selected for human DCs uniquely.

As an additional note, while most aptamer selections have random regions of ~20-30 bases, the length of DNA nanoparticle templates is limited by the ability to efficiently circularize the template. Circularization efficiency was seen to drop dramatically below ~80 bases due to the steric difficulty of folding, so assuming 2 X

20 base PCR priming sites, this makes a minimum of a 40 base random region, with the exception of simply adding generic bases to fill the extra space. It is of note that the artificial restriction of aptamer (and peptide) shape space can be achieved by biasing the initial library toward certain features. This can be achieved by altering the library's initial base composition ratios<sup>49</sup> or peptide ratios/ properties in the case of phage display<sup>50</sup>. In this case, the actual random region may be shorter and the fraction of shape space sampled can be increased. Furthermore, the generation of DNA nanoparticles results in many copies of each sequence in the initial round as opposed to SELEX protocols, which ideally have one copy of each sequence in the first round. With a fixed total number of sequences, this means that DNA nanoparticles will have less overall diversity, but more multiplicity for each sequence in the initial round. The diversity is also limited practically by the concentration of nucleotides in the synthesis reaction. With these considerations, the practical diversity of the initial round of DNA nanoparticle selection is  $\sim 3E10$  particles with a random region of 60 bases (see DNA nanoparticle synthesis protocol). Therefore only a tiny small fraction of the sequence space is being assayed, however with each sequence being present in many copies in the initial round, the probability of a successful binding particle being amplified is greater. A detailed model of the mathematics of SELEX against complex targets such as cells has been described by Vant-Hull *et. al.*<sup>51</sup>. Practically, these limitations are difficult to circumvent given the current selection protocol.

## 2.11 Conclusions and Future Directions

The future of this nanoparticle platform is still very open as screenings can be performed against any number of potential targets. Likely the most attractive candidates will continue to be cells of various types primarily because the diverse surface structures that these nanoparticles are likely to possess may serve as an ideal specific recognition “surface” for complex cell surfaces. In this scenario, we can imagine that in place of using a single short aptamer that recognizes a single target on a cell surface, the DNA nanoparticle may not actually fold into neat repeat motifs but rather into a low energy form that matches a cell surface topographically. Other potentially useful pursuits include taking advantage of the simple attachment chemistry that DNA affords. For example, the primary amines on adenine, guanosine and cytosine are candidates for carbodiimide (EDC/NHS) attachment ligands containing carboxyl groups. A proposed application may be the attachment of the carboxyl groups of DOTA, which can be used as a heavy metal chelator including MRI contrast agents such as gadolinium (Gd). This will allow for the highly concentrated co-localization of Gd which has been previously shown to increase MRI efficiencies 40-90 fold over free Gd contrast agents when Gd complexes and concentrates in the defects of carbon nanotubes<sup>13</sup>. Additionally, there may be other ways of functionalizing the DNA nanoparticle that can be explored.

Attempts were made to incorporate platinum (Pt) into the DNA nanoparticles via cisplatin which naturally binds at the N5 position of guanine nucleotides and crosslinks most intrastrand guanine dinucleotides. DNA nanoparticles that were incubated with cisplatin were purified via size exclusion in a Bio-Gel P100 resin

column and collected wells were analyzed by induced coupled plasma mass spectrometry (ICP-MS).

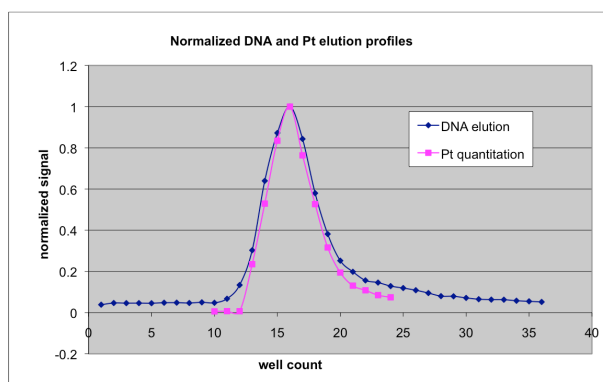


**Figure 13: Elution Profile of DNA Nanoparticles Purified by Size Exclusion Overlaid With Pt ICP-MS Quantification.** DNA nanoparticles are incubated at room temperature with cisplatin and purified from free cisplatin by size exclusion chromatography in a Bio-Gel P100 resin column. Well elutions were evaluated both for DNA content (by OliGreen fluorescent staining) and for platinum content (by ICP-MS). The co-elution of the DNA with platinum is evidence of platinum incorporation into the DNA nanoparticles.

DNA elution was evaluated by OliGreen quantification and Pt elution by ICP-MS (Figure 13). It was observed that a substantial amount of Pt co-eluted in the fractions containing the DNA nanoparticles (vs later fractions of free nucleotides as determined previously) indicating Pt incorporation into the particles. Loading efficiencies were not calculated, however, given the apparently good binding of cisplatin to the DNA, electron microscopy was attempted utilizing WETSEM cells (Electron Microscopy Sciences) in order to keep the DNA in its hydrated shape. Preliminary images can be seen in Figure 14. It is not certain that these particles are the DNA nanoparticles, however, they match very closely the DLS and calculated estimates for the particle size. From both an imaging and therapeutic perspective, it is worth pursuing the incorporation of metals into DNA nanoparticles.

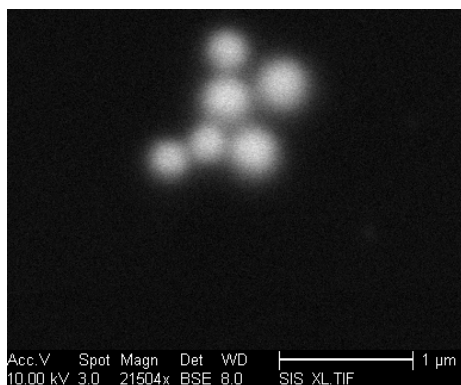


**Figure 14: WETSEM Image of DNA Nanoparticles Incubated with Cisplatin.** DNA nanoparticles incubated at room temp with cisplatin and purified by gel chromatography imaged with WETSEM electron microscopy.

The novelty of this platform has great potential for the future nanotechnology applications due to the diversity of potential characteristics and properties that are available with carefully designed exponential enrichment protocols. There is currently no other targeted nanoparticle that utilizes the principle of selection “in context” as the process described in this dissertation does. In addition, no other nanoparticle platform has the unique characteristic of possessing several different orthogonal properties with a single molecular entity such as DNA. The evolutionary approach versus the structural/rational approach for the design of nanoparticles is an interesting and ongoing argument in the biological field with one side arguing that evolutionary methods are nature’s way and will always produce superior functionality regardless of structure, and the other claiming that without an understanding of hierarchical and rational design, complex functionalities cannot be achieved or understood. The core of the argument is whether functionality is in itself sufficient for applications. The complexity of biology often necessitates this approach as prior to the invention of protein crystallography there was very little understanding of biological mechanisms

of action and even now there is still a large degree of ignorance about how many biological processes operate. This does not, however, hinder the progress of biological research and the utilization of the products of these unknown mechanisms, but nevertheless runs a bit counter to the precept of nanotechnology as a rationally hierarchical design paradigm. With regards to the DNA nanoparticles described in this dissertation, it appears that we have discovered a novel form of functionality, which is reproducible and specific. However, due to the complexity of the product, it is extremely difficult to understand how or why this functionality arose or what precisely is its mechanism of action. For some proposed applications of novel cell recognition particles such as cell sorting, staining, and perhaps even *in vivo* targeting, a simple functional readout is likely sufficient to achieve the goal. However, without an understanding of the structure/function relationship, there will always be limitations to how much functionality can be added, how much structure can be altered and what its effect on function will be, and whether any of these proposed modifications or additions would have reproducible effects. Nevertheless, despite these potential hurdles, the concept of exponential and evolutionary selection of biomolecules for nanotechnological applications will continue to be a dominant and growing field. The relative biocompatibility of the products (both peptides and oligonucleotides), the diversity of functions that can be rationally selected, and their ease of homogenous synthesis and characterization (at least for short segments) will contribute to their success in the nanotechnology tool kit. The potential challenges and risks of this functional platform can be, in part, mitigated by taking, in parallel, a more traditional approach to constructing nanoparticles. In nanotechnology, materials are just as

important as the unique structures that can be made from them. The next few chapters will discuss steps toward developing novel structures from more traditional building blocks of iron oxide and gold.

## **2.12 Acknowledgements**

This chapter contains material taken from Steiner, J.M. Sartor, M. Sanchez, A.B. Messmer, D. Freed, A. Esener, S. Messmer, B.T. “DeNano: Selectable deoxyribonucleic acid nanoparticle libraries”, *Journal of Biotechnology*, Vol. 145, Pp, 330-333, 2010.

## CHAPTER 3:

### INORGANIC NANOPARTICLE THERANOSTIC COMPONENT: IRON OXIDE

#### 3.1 Introduction/Rationale

Much of the history of the synthetic nanoparticle field has been dominated by small (1-100nm) particles of inorganic materials such as metals and oxides. For example, gold nanoparticles (~10nm) have been used for centuries as the red pigment in stained glass windows and titanium dioxide nanoparticles have long been a common ingredient in cosmetics, paints, vitamins and a wide range of other applications. Their ubiquitous use is a consequence of the unique physical properties that arise on the nano-scale as well as well-understood mechanisms of synthesis. It is, therefore, a natural extension to consider these materials for biological applications, and much work has been done toward this goal. Perhaps the most well known inorganic material being now utilized for biological applications is iron oxide. Consisting of just atomic iron and oxygen, with molecular formulas  $\text{Fe}_2\text{O}_3$  and  $\text{Fe}_3\text{O}_4$ , or some mix thereof, iron oxide has many unique properties that make it advantageous as a biomaterial<sup>52</sup>. In particular, it is the only naturally magnetic material composed of

elements already common in biology—cobalt and nickel are also naturally magnetic but do not exist in any appreciable concentration in biological systems, whereas iron exists naturally in relatively large quantities bound to heme groups in blood. As a result of the magnetic functional properties and relative bio-compatibility, iron oxide nanoparticles have taken a central role in both *in vivo* diagnostics and therapeutics<sup>52,53</sup>. The most common use of iron oxide nanoparticles for *in vivo* biological diagnostics is as a Magnetic Resonance Imaging (MRI) contrast agent. MRI operates by rapidly aligning hydrogen nuclei in water with a very strong magnetic field and observing their relaxation when the field is removed. Iron oxide is a naturally ferromagnetic material with multiple magnetic domains and consequently a relatively high Curie Temperature. However, at the nano-scale (<~20nm), iron oxide can be considered to consist of a single magnetic domain and the Curie Temperature drops below room temperature as thermal energy alone dominates the motion of atoms and consequently the magnetization of the particle—this state is known as superparamagnetism and is necessary for the rapid alignment of the magnetic fields under an externally applied field at room temperature such as in MRI. The induced magnetic fields of the iron oxide alter the local environment of hydrogen nuclei and therefore act as agents lending contrast to the resulting image. The greatest magnetic effect is seen when surrounding water can interact directly with the iron oxide surface where the field is the highest and when that water can freely exchange with the bulk solution water<sup>54,55</sup>. This superparamagnetic property and the ability to instantly manipulate the magnetic moment of small particle of iron oxide have also been utilized for therapeutic applications. Under a rapidly oscillating external magnetic field, nanoparticles of iron

oxide vibrate and generate substantial thermal energy that has been used to selectively ablate tissue. This therapy has been shown to register temperature increases of several dozen degrees Celsius *in vivo*<sup>25</sup>. From both the diagnostic and therapeutic standpoint, therefore, there has been substantial research on methods of producing and, more importantly, stabilizing iron oxide nanoparticles.

### **3.2 Iron Oxide Synthesis Overview**

There are several approaches for the synthesis of iron oxide nanoparticles that can be divided into two principle categories: aqueous and organic synthesis.

#### **3.2.1 Aqueous Synthesis**

The most common aqueous synthesis method is alkaline co-precipitation. The process involves mixing ferrous and ferric ions in a 2:1 ratio and rapidly raising the pH using a basic solution. The morphology of the Fe<sub>3</sub>O<sub>4</sub> particles produced is dependent on original ion concentrations, temperature and pH and results in particles with no stabilizing surface groups. In practice, this process yields nanoparticles between 5-15nm in diameter. A second method is a hydrothermal route in which iron salt precursors are mixed under high temperature and pressure to crystallize with or without surfactants. In general this process yields a high degree of crystallinity and nanoparticles can be produced that range in size depending on reaction period. Iron oxide nanoparticles up to 40nm have been produced using this method<sup>53</sup>.

### 3.2.2 Organic Synthesis

Organic methods of iron oxide synthesis include thermal decomposition of  $\text{Fe}(\text{cup})_3$  (cup = N-nitrosophenylhydroxylamine),  $\text{Fe}(\text{acac})_3$  (acac = acetylacetonate), or  $\text{Fe}(\text{CO})_5$  followed by oxidation at increased temperatures. In general, this process yields extremely monodisperse products but is much more involved than aqueous methods. Products are produced in organic solvents and are stabilized by hydrophobic capping ligands rendering them insoluble in water. Iron oxide of a range of sizes can be achieved with this method, up to  $\sim 50\text{nm}$ . An alternative method is the microemulsion method where water emulsions (with iron salts) are stabilized in oil solutions with surfactants. This also yields water insoluble products that are often prone to aggregation<sup>53</sup>.

### 3.3 Iron Oxide Nanoparticle Stabilization

The aqueous stabilization of iron oxide nanoparticles is a critical element for their future use as theranostic agents. Nanoparticles, in general, possess very high surface energies as a consequence of their large surface area and as such are prone to aggregation. Additionally, it is predicted that the surface of oxides produced by aqueous is populated by hydroxyl (-OH) groups which are uncharged at physiologic pH, resulting in a relatively hydrophobic surface methods. Iron oxide nanoparticles produced by organic synthetic routes possess hydrophobic capping ligands that also make them insoluble in aqueous media. As such, various methods have been employed for the aqueous stabilization of iron oxide nanoparticles at physiological pH.

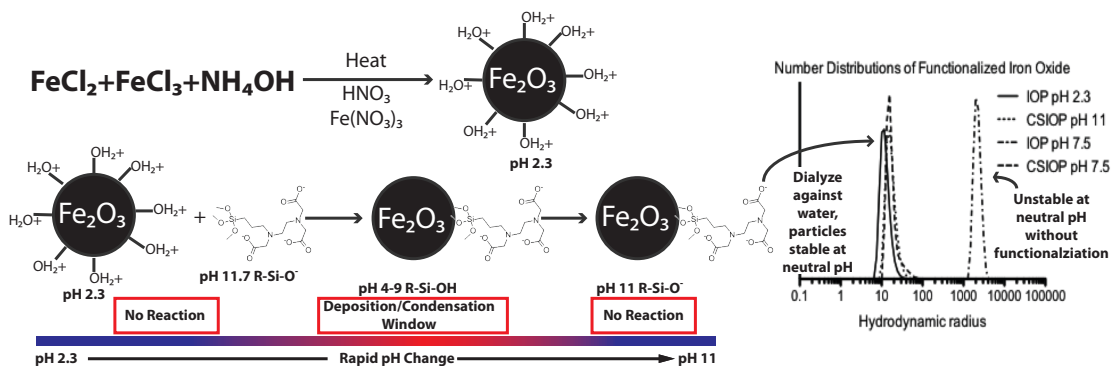


**Figure 15: Summary Schematic of Iron Oxide Nanoparticle Synthesis and Silane Functionalization.** Iron oxide nanoparticles are synthesized by alkaline co-precipitation and annealed in nitric acid and ferric nitrate under reflux. Functionalization via a carboxy silane utilizes a novel pH gradient shift in a self-limiting reaction that stabilizes the iron oxide in neutral pH without increasing its hydrodynamic radius.

Many of these methods rely on rendering hydrophilic surfaces through lengthy ligand exchange reactions (in excess of 72 hours) in the case of organic synthesis, or various coatings of small molecules, polymers, biological molecules such as proteins, metals or silica<sup>53,56-58</sup> in the aqueous synthesis case. From both an imaging and therapeutic perspective, an ideal surface coating would be covalent, thin (such that water may closely interact with the nanoparticle's magnetic field), pH stable, non-immunogenic and easily functionalized with further ligands. Current commercial iron oxide nanoparticles are most commonly coated in a thick layer of dextran with core sizes ~10nm but hydrodynamic radii ranging up to 140nm<sup>59</sup>.

### 3.4 Novel Iron Oxide Functionalization

To address the requirements of effectively stabilizing iron oxide nanoparticles, I developed a novel process to deposit an extremely thin stabilizing layer of silica over superparamagnetic iron oxide that yields particles that are aqueous stable over a wide

range of pH values (5.9-11.6) indefinitely on the bench top. The process takes advantage of a rapid pH shift that provides an instantaneous window for deposition that is sufficient to stabilize the particles, but rapid enough to prevent aggregation. The process can be seen schematically in Figure 15.

### 3.4.1 Iron Oxide Nanoparticle Synthesis Protocol

Iron oxide nanoparticles are produced following the protocol of Chastellain *et al.*<sup>57</sup>. Fe<sub>2</sub>O<sub>3</sub> iron oxide nanoparticles (IOP) are produced by standard alkaline co-precipitation followed by oxidation to Fe<sub>2</sub>O<sub>3</sub> in the presence of ferric nitrate and nitric acid. Briefly 86mM FeCl<sub>3</sub> and 43mM FeCl<sub>2</sub> are prepared in 25mL deionized water to which 2.5mL NH<sub>4</sub>OH is rapidly injected under ambient conditions. The black precipitate is washed several times with water and particles are refluxed with magnetic stirring in .2M Fe(NO<sub>3</sub>)<sub>3</sub> and .8M nitric acid for 1 hour. The black particles gradually turned bright orange/brown and precipitated on the magnetic stir bar. Excess nitric acid was removed and particles were immediately redispersed in 10mM nitric acid water and dialyzed overnight against 10mM nitric acid. The dialyzed sample was recovered in a final volume of 10mL of 10mM nitric acid. The transparent red Fe<sub>2</sub>O<sub>3</sub> solution is stable in 10mM nitric acid pH 2.3 by virtue of the -OH<sub>2</sub><sup>+</sup> groups on the surface and particles are monodispersed at 8 +/- 2nm in diameter. Transmission electron microscopy images of the particles can be seen in Figure 16. X-ray diffraction patterns of this synthetic protocol indicate an intermediate lattice parameter between maghemite and magnetite<sup>57</sup>.

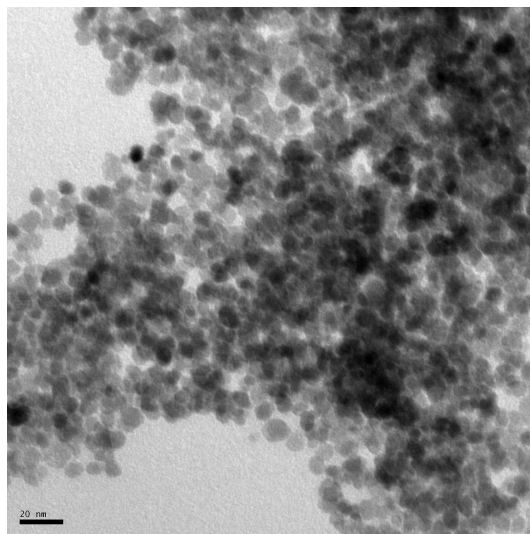


**Figure 16: Bare Iron Oxide Nanoparticles.** Sample produced by standard alkaline co-precipitation of ferric/ferrous chloride with ammonium hydroxide and refluxed in the presence of ferric nitrate and nitric acid. Resulting nanoparticles are 8 +/- 2nm in diameter. See procedure for details. Scale bar is 20nm.

### 3.4.2 Surface Silane Functionalization

The nanoparticles seen in Figure 16 are stable in 10mM nitric acid at pH 2.3, however aggregate substantially at neutral, physiologic pH. In order to render them stable at neutral pH, a carboxy silane ligand was chosen 1) because carboxyl groups are negatively charged at neutral pH and should grant the particles charge stabilization and 2) because silanes are known to bind covalently to hydroxyl groups on the iron oxide surface<sup>58,60,61</sup>. The ligand chosen was *n*-(trimethoxysilylpropyl)ethylene diamine triacetic acid, sodium salt seen in Figure 17.

### 3.4.3 Silane Functionalization Protocol

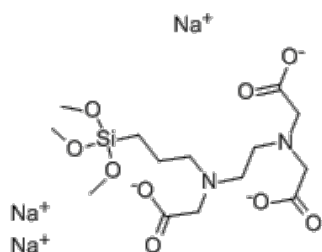


**Figure 17: *n*-(trimethoxysilylpropyl)ethylene diamine triacetic acid, sodium salt.**

The functionalization protocol is extremely easy. 66 $\mu$ L 50% (w/v) *n*-(trimethoxysilylpropyl)ethylene diamine triacetic acid, sodium salt in water (pH 11.7) (ABCR, Germany) is rapidly injected into 1mL of bare iron oxide nanoparticles in nitric acid at pH 2.3 (see iron oxide nanoparticle synthesis) under vigorous magnetic stirring. The dark red solution becomes briefly turbid and immediately re-clarifies with no net change in absorbance indicating no aggregation or solution based condensation. The solution settles to an equilibrium pH of 11 at which point the reaction is complete. The carboxy-silane functionalized iron oxide particles (CSIOP) were magnetically collected, washed in pH 11 NaOH to clear excess silane without inducing silane condensation and dialyzed overnight against water and recovered in 11mL of water. The functionalization reaction is essentially instantaneous resulting in stable particles immediately.

### 3.5 Functionalization Characterization

#### 3.5.1 Transmission Electron Microscopy

As analyzed by transmission electron microscopy, morphologically there is no distinction between bare IOP and CSIOP nanoparticles as seen in Figure 18. It is presumed that the silica layer deposited on CSIOPs is a monolayer because it cannot

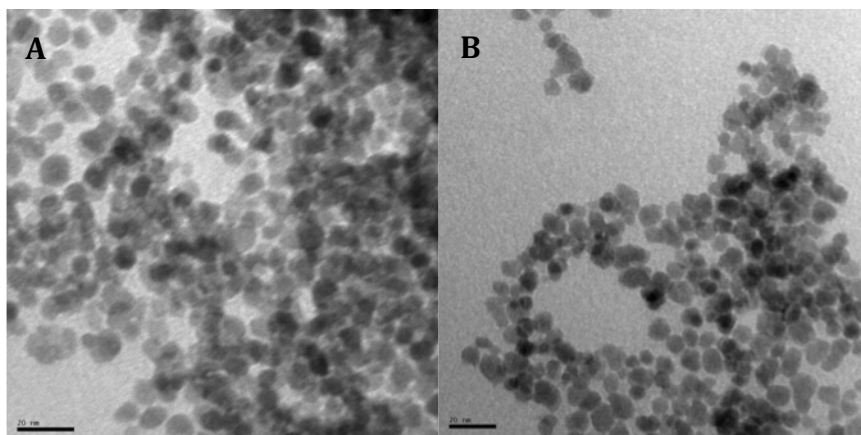


**Figure 18: Bare IOP (A) and CSIOP (B) Showing No Morphological Differences.** Iron oxide nanoparticles are produced by alkaline co-precipitation as in the described protocol and stabilized in pH 2.3 10mM nitric acid (**a**). Nanoparticles after silane functionalization in water (pH 6) show no aggregation and no discernable thickness to the functional silane layer (**b**).

be resolved by TEM.

Similarly, Dynamic Light Scattering (DLS) results do not indicate a substantial change in nanoparticle hydrodynamic radius as seen in Figure 19. However, it is visually evident that the stabilizing surface functionalization is present when comparing the response of IOP and CSIOP to changes in pH. When both IOP and CSIOP are mixed in 100mM Tris-Cl at pH 7.5, there is visible aggregation of the bare iron oxide as seen in Figure 19.

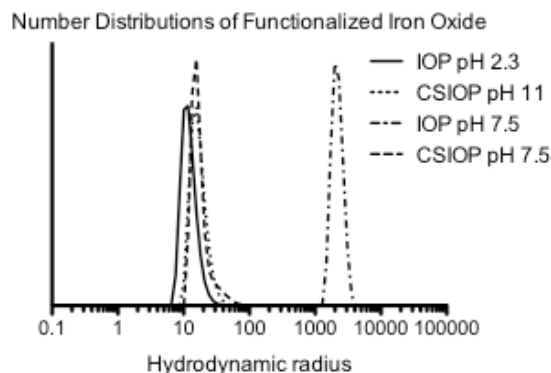


**Figure 19: Dynamic Light Scattering Measurements of IOP and CSIOP.** IOP immediately after synthesis at pH 2.3 are compared to CSIOP immediately after functionalization at pH 11 and CSIOP at neutral pH in 100mM Tris-Cl at pH 7.5 with almost no observed differences. In contrast, bare IOP at pH 7.5 aggregate substantially.

### 3.5.2 Fourier Transform Infrared Spectroscopy

To analytically verify the presence of the functional ligand, Fourier Transform Infrared Spectroscopy was performed. IOP and CSIOP were lyophilized and mixed in a potassium bromide (KBr) pellet for transmission spectroscopy. Silanes are known to covalently bond to iron oxide via surface

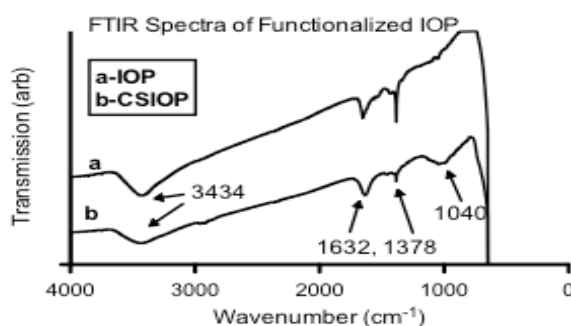


**Figure 20: Fourier Transform Infrared Spectroscopy of IOP and CSIOP.** The presence of a band at 1040cm<sup>-1</sup> in the CSIOP sample is indicative of the Si-O-Fe stretch and confirmation of the presence of the surface carboxy silane ligand.

-OH groups<sup>62</sup>. The Fourier Transform Infrared Spectrum seen in Figure 20 shows this functional bond. The strong absorption near  $650\text{cm}^{-1}$  is characteristic of the Fe-O bond in iron oxide and bands at  $3434\text{cm}^{-1}$ ,  $1632\text{cm}^{-1}$ , and  $1378\text{cm}^{-1}$  are stretching, deformed vibration and bending, respectively of the -OH bond<sup>63</sup>. The functional group is seen by the appearance of band at  $1040\text{cm}^{-1}$ , identifying the Si-OH, Si-O-Si, or Si-O-Fe stretch<sup>63</sup>. It is proposed that the silane functionalization is relatively sparse given the weakness of the peak by FTIR and the fact that transmission electron microscopy cannot resolve a layer.

### 3.5.3 Vibrating Sample Magnetometry

The purpose of these iron oxide nanoparticles is ultimately to serve as magnetic resonance contrast agents and therefore it is required that they be superparamagnetic. It is also important to determine whether the surface silane functionalization has any effect on their magnetic properties as silica coatings on iron oxide nanoparticles have been shown to substantially reduce the saturation magnetization<sup>64</sup>. Both IOP and CSIOP were lyophilized into powders and their magnetic properties were measured by Vibrating Sample Magnetometry (VSM) at several different temperatures as seen in Figure 21.

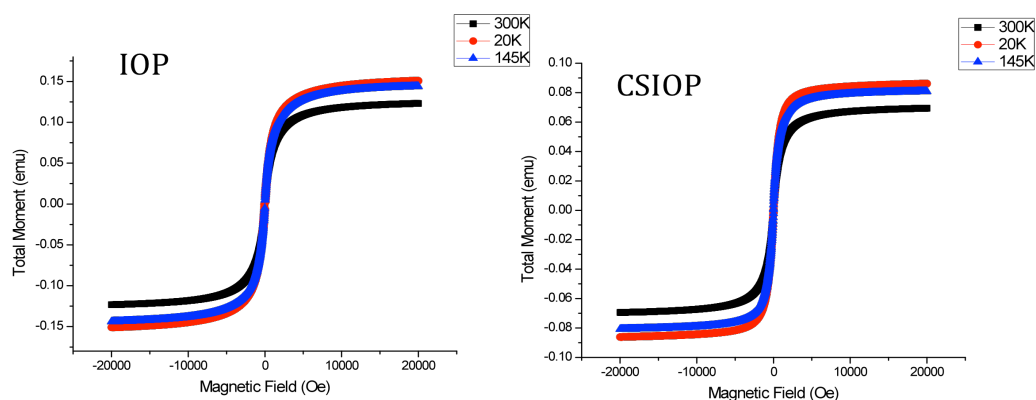


**Figure 21: Vibrating Sample Magnetization Curves for IOP and CSIOP.** Give the appropriate masses measured the saturation magnetizations for IOP is 79.9 emu/g and CSIOP is 59.9 emu/g.

Neither sample shows hysteresis at temperatures ranging from 20-300K indicating that they are fully superparamagnetic. The saturation values obtained for IOP and CSIOP are 79.9 and 59.9 emu/g respectively at 20K as compared to bulk maghemite which has a saturation magnetization of  $\sim 80$  emu/g<sup>65</sup>. It appears that the silane coating does have an effect on the net magnetization of the particles decreasing it about 25%, however, it is possible that if there was any free silane condensation into silica particles (thought not observed visually or by absorbance) that those particles would have contributed to the mass of the whole sample but not to the net magnetization. In this case, the saturation magnetization per gram particle weight would indicate a slightly lower value.

### 3.6 Aqueous Stability

The purpose of nearly all surface functionalizations of iron oxide nanoparticles is to render them aqueous stable at physiologic pH. The thin carboxy silane functionalization presented here yields iron oxide nanoparticles that are stable

indefinitely across a wide range of pH values. The plot in Figure 22 tracks the absorbance of iron oxide solutions at different pH values over time. The plot shows stability out to 2 weeks, but visual inspections have seen no observed changes or

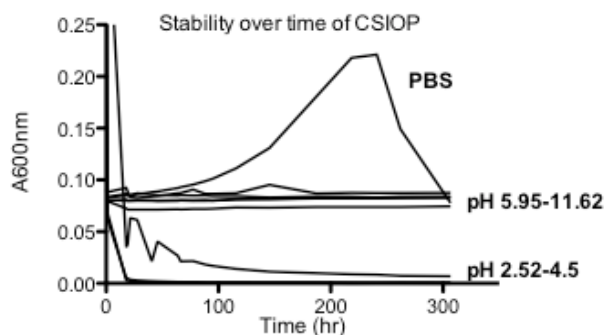


**Figure 22: Absorbance at 600nm of CSIOP Over Time.** Varying pH values demonstrating stability of CSIOP over pH 5.95-11.62 and in phosphate buffered saline (PBS)

aggregation over several months in 100mM Tris-Cl buffer pH 7.5. The range of stable pH values is in line with the range of pKa values for carboxyl groups which can range up to ~4-5 for various molecular carboxyls. Samples were measured only up to pH 11.62, however it is predicted that samples would be stable above this as well with deprotonated carboxyl groups providing sufficient charge stabilization. At pH values below the pKa value of the carboxyl group, the particles rapidly aggregate and fall out of solution. While particles are very stable in water, in physiologic salt conditions (137mM NaCl)—here tested in phosphate buffered saline (PBS)—the particles will slowly aggregate over time producing a cloudy solution. The observed increase “absorbance” is in reality just a larger degree of scattering as the particles aggregate into larger clumps with the subsequent decrease in absorbance resulting from those clumps falling out of solution. A similar aggregation and precipitation effect was seen when particles were incubated in 10% serum in water.

### 3.7 Proposed Reaction Mechanism

The functionalization reaction is nearly instantaneous and immediately results in stable nanoparticles in a self-limiting manner. The self-limiting functionalization is a result of the pH shift during synthesis that can be seen in Figure 23. The stock carboxysilane salt (45% in water) is stabilized in the siliconate form by the high pH of 11.7 resulting from the equilibrium of  $\text{COO}^-$  groups absorbing  $\text{H}^+$  ions from the aqueous solution. Upon addition to iron oxide at pH 2.3 (stabilized in 10mM nitric acid by a strong positive zeta potential resulting from  $\text{OH}_2^+$  surface groups), the siliconate groups become protonated to silanols and the basic solution drives the pH of the solution up initiating silanol condensation at the positively charged iron oxide surface<sup>66</sup>. The simultaneous addition of  $\text{COO}^-$  groups to the iron oxide surface,

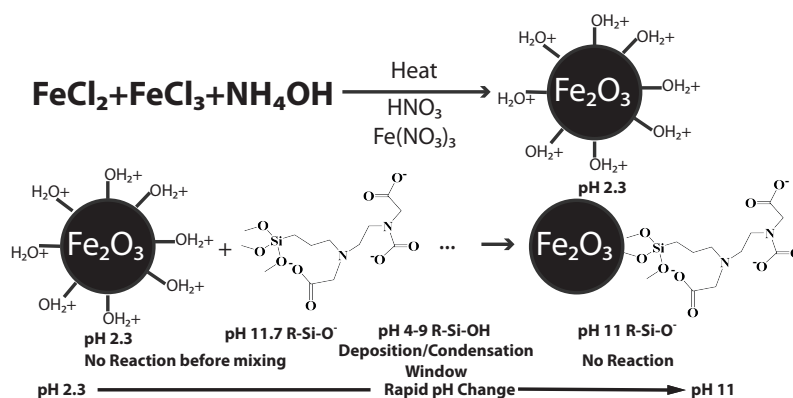


**Figure 23: Proposed Reaction Mechanism for Carboxy Silane Iron Oxide Functionalization.** Highly basic carboxy silane is added in sufficient quantity to acid stabilized IOP to achieve an equilibrium at pH 11. Reaction pH rapidly shifts from 2.3-11 passing rapidly through a window of silane deposition (~pH 6-8) that stabilizes particles without aggregation

coupled to the solution pH rapidly shifting to 11 quickly stops both surface and solution based silanol condensation and excess siliconates are restabilized at high pH.

The reaction is so rapid that iron oxide particles are taken through neutral zeta potential without aggregation and free silica condensation is prevented, resulting in a transparent solution with no increase in total absorbance at 600nm, indicating no new particle formation or substantial growth. It is important to note that this extreme pH shift is essential for particles to be stabilized. When smaller volumes of carboxy silane were injected into the acid stabilized iron oxide solution, the equilibrium pH obtained was much more neutral and free silane condensation continued to occur resulting in rapidly aggregating particles. It is necessary to add a sufficient amount of basic silane to the acidic iron oxide in order for the reaction to equilibrate at a pH at which the siliconates are once again stable and free condensation/aggregation is prevented. It is also of note that functionalization with this mechanism was not successful when attempted with an aminated silane (Aminopropyltriethoxy silane or APTES) regardless of the amount of silane added to the iron oxide solution. The APTES solution itself is basic, and its addition to the acidic iron does increase the pH in a similar manner, but the resulting functional amine groups are uncharged at the high equilibrium pH and consequently result in more neutral zeta potentials and aggregated particles. APTES is the mostly commonly used silane ligand to stabilize iron oxide nanoparticles<sup>58,60,61</sup>, however for aqueous synthesis protocols, APTES functionalization has not been shown to yield sufficient long term stability and/or thin enough functional layers to be practically useful<sup>61</sup>.

### 3.8 Conclusions

The application of superparamagnetic iron oxide nanoparticles is a growing field, however, few synthetic routes currently leads directly to water soluble particles necessary for biological applications. Various methods to produce water soluble particles from organic synthetic protocols have been devised, many of which involve substantial reaction times and toxic solvents. Aqueous synthetic routes are simpler but also result in hydrophobic surfaces at neutral pH. Common methods of stabilizing iron oxide often involve coatings of polymers, metals, silica or biomolecules and often result in thick coatings that dramatically increase the particle hydrodynamic radius or are unstable over long periods of time. To address this, I have developed a method for the rapid and covalent functionalization of iron oxide producing an extremely thin stabilizing layer that is unresolvable by TEM and does not substantially increase the particle hydrodynamic radius. Furthermore, the particles are stable in all pH ~5.9-11.6 indefinitely. The protocol is a useful addition to the tool kit for iron oxide functionalization approaches and its properties of aqueous stability, and thin functional layer that does not appreciably affect the magnetic response of the core iron oxide will serve as a precursor for the core shell structures discussed later in this dissertation.

### 3.9 Acknowledgements

This chapter contains materials taken from Steiner, J. Esener, S. Self-Limiting Deposition of *n*-(Trimethoxysilylpropyl)ethylene Diamine Triacetic Acid for the Production of Aqueous-Stable Iron Oxide Nanoparticles. *Chemistry Letters*. Vol. 40 (2011) , No. 5 p.536

## CHAPTER 4:

### INORGANIC NANOPARTICLE THERANOSTIC COMPONENT: GOLD NANOSHELLS/NANOCAGES

#### 4.1 Introduction/Rationale

In recent years, metallic nanostructures have gained substantial recognition for applications in a wide variety of fields owing to their unique optical properties, which differ dramatically from their bulk phases. For biological applications, much of this attention has been directed toward nanostructures of gold primarily for its relative biological inertness and ease of chemical modification, resulting in a diverse array of structures such as nanoparticles, nanorods, nanoshells, nanowires and a variety of modifications therein<sup>67-70</sup>. The specific optical properties of these structures are the product of surface plasmons that are generated in their quantum-confined volumes, the wavelength of which can be tuned across nearly the entire visible and near infrared (NIR) spectrum by altering the physical characteristics. Of important note is the ability to produce strong plasmon resonance in the 700-900nm range, the most optically transparent window of biological tissue, by the creation of thin nanoshells of gold surrounding a dielectric nanoparticle core<sup>26,68,71-74</sup>. The specific plasmon

resonances are governed by physical characteristics such as absolute particle size, ratio of shell/core diameter and surface functionalization and open the window for a wide array of *in vivo* applications. These nanoshells also possess the potential to encapsulate, ferry and protect cargo within its dielectric core such as drugs, iron oxide nanoparticles (IOP), and quantum dots and indeed such multifunctional particles have been utilized for biological applications<sup>68,75,76</sup>. Potential synergies of these multifunctional particles include orthogonal imaging modalities, such as the optical and magnetic properties of iron oxide encapsulated in a gold nanoshell, as well as the ability to provide therapeutic effect through either inherent thermoablation or through the encapsulation of toxic cargo<sup>64</sup>. Furthermore, an even greater structural hierarchy can be achieved in a subset of core/shell particles whereby the shell is both hollow and porous, resembling a “nanocage”. These cage structures are used primarily to encapsulate particles whereby the pore size is smaller than the entrapped particle diameter (Fig. 25). A potential advantage of this approach includes free access of the internal particle core to solution-based molecules while being shielded from interactions with larger particles, surfaces, and cells.

## 4.2 Gold Nanoshell Synthesis Summary

There are several approaches for the production of gold shells that can be divided into two main categories: gold nanoparticle seeding/growth and galvanic replacement. Direct surface reduction is another method, however, it is significantly less common.

### 4.2.1 Gold Nanoparticle Seeding

Seeding is perhaps the most common of these approaches and results in shells generally produced over a solid dielectric cores. The process involves binding small gold nanoparticles (2-5nm) covalently or electrostatically to a nanoparticle template particle. These seeds then serve as nucleation sites for the further reduction of a gold salt in solution utilizing reducing agents such as formaldehyde, sodium borohydride, hydroquinine, or ascorbic acid. The seeds grow rapidly in diameter until they merge into a complete shell. Substantial work has been done utilizing this approach for the production of gold nanoshells over silica and crosslinked polystyrene templates<sup>74,77,78</sup> with less work focusing on a variety of other polymer and uncrosslinked templates. However, producing gold nanoshells over uncrosslinked polymer templates has several advantages for biological applications such as the ability to have biodegradable cores that result in hollow shells with the possibility of releasing an encapsulated drug<sup>75</sup> and the ability to encapsulate larger particles and create heterogeneous hollow core/shell structures. The gold nanoparticle seeding process can be seen visually in Figure 24. The quality of the nanoshells produced by the seeding

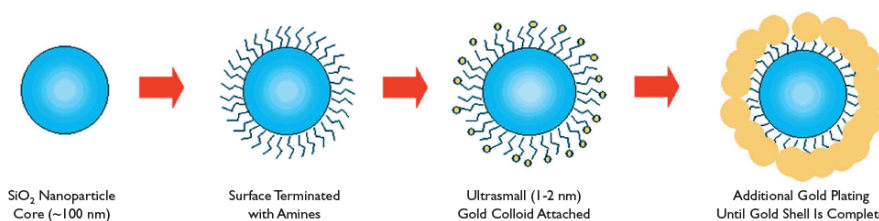


**Figure 24: Seeded Growth of Gold Nanoshells.** Small gold seeds (2-5nm) are covalently bound to a nanoparticle template and subsequently grown by the reduction of a gold salt to merge into full and complete shells<sup>79</sup>

process is highly dependent on both the reaction conditions as well as the choice of reducing agent. The choice of reducing agent is particularly important as it will determine the homogeneity of the produce and the extent of free nucleation that contaminates the production of gold shells. The most common reducing agents used are sodium borohydride<sup>74</sup>, formaldehyde<sup>75</sup>, or ascorbic acid<sup>80</sup>, ranked in order of their relative strength. It is important to note that all of these agents rapidly reduce gold salts in solution, the balance of gold shell to free nucleation being determined by the concentration of gold seeds to serve as nucleation sites. Reaction conditions for typical protocols utilize potassium carbonate ( $K_2CO_3$ ) and chloroauric acid ( $HAuCl_4$ ) for the production of gold hydroxide ( $H_3AuO_3$ ) which serves as the seeding salt for gold reduction. This process also buffers the reactions conditions with the carbonate ion.

In practice, it has been difficult with uncrosslinked polymer templates such as polylactic-co-glycolic acid (PLGA) (as opposed to silica) to achieve sufficient gold seed concentration (as a combination of both template concentration and gold seeding efficiency) to avoid free nucleation with the previously mentioned reducing agents. Published efforts to produce gold nanoshells over PLGA templates with formaldehyde have thus been executed with several stepwise reduction steps and centrifugation washing steps in between to remove small nucleated gold particles, ultimately resulting in poorly formed shells and an involved synthetic process (Fig. 28)<sup>75</sup>. It is therefore desirable to find a reducing agent that will not reduce gold salts in solution but will deposit gold on surfaces to grow existing seeds in order to produce

homogeneous gold nanoshells over uncrosslinked (and possibly sacrificial) polymer templates even in dilute conditions.

#### **4.2.1.1 Production of Gold Shells on PLGA Templates Via Gold Seeding**

The production of gold shells over PLGA template nanoparticles is primarily an issue of surface stabilization and functionalization, the key component of which is to securely attach gold seeds to the template nanoparticle surface, accomplished by either covalent bonds or electrostatic interaction. Published efforts to do this have used carboxy terminated PLGA and used carbodiimide chemistry to functionalize the surface with cysteamine—the thiol providing the gold binding agent<sup>75</sup>. Attempts made to reproduce this protocol continually met with aggregation as the amines and thiols altered the naturally negative zeta potential of PLGA toward neutral and destabilized the particles—additionally, even with short PLGA monomers, the number of carboxy terminated ends that reside on the surface does not appear to be sufficient to achieve a high seeding density when functionalized with thiols. Consequently a layered approach was taken to coat the negatively charged surface with positively charged poly-L-lysine (PLL). This layering approach stably reverses the negative zeta potential of PLGA to highly positive and produced a surface displaying several primary amines that can bind to gold in a covalent manner<sup>81</sup>. Citrate stabilized gold seeds (5nm) were then bound to the positively functionalized PLL-PLGA templates. The process is seen schematically in Figure 25. The electrostatic surface modification of this negatively charged template by coating with PLL is simple, effective and applicable to any negatively charged nanoparticle template. The primary amines of

the PLL serve both to bind to the negatively charged PLGA introducing a large shift in the zeta potential from -30mV to 45mV without inducing aggregation as well as provide binding sites for gold seeds. Importantly, the binding of PLL to the surface of PLGA is based primarily on charge attraction and therefore is not stable for long periods upon dilution or repeated extensive washings. However, subsequent seeding of 5nm citrate stabilized gold seeds reversed the zeta potential back negative to -30mV and appeared to be stable over at least several hours. It is of note that smaller 2nm gold seeds stabilized by tetrakis(hydroxymethyl) phosphonium chloride (THPC) did not result in a large enough negative zeta potential reversal to overcome the positive surface charge conferred by the PLL. PLGA coated with PLL and seeded with 2nm gold particles were unstable and aggregated quickly as a result of a more neutral final zeta potential.

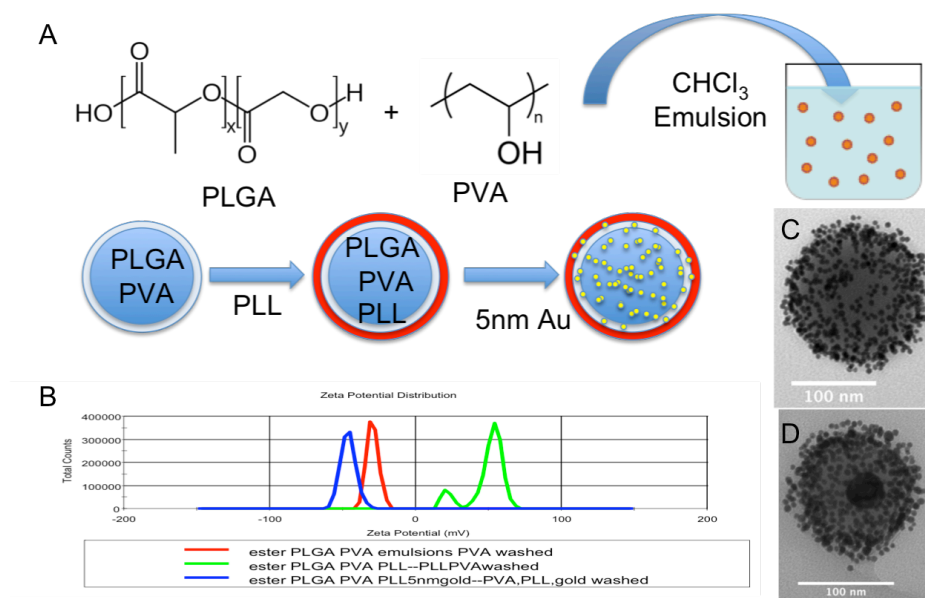


**Figure 25: Schematic Seeding of PLGA Nanoparticles with Gold Seeds for Gold Shell Production.** Emulsions of PLGA and PVA were made, coated with PLL and then seeded with 5nm gold (**a**). Gold particles bound to primary amines on the PLL in a semi diffuse manner as seen in the TEM micrograph (**c**). Particles were stable at each step of the procedure as noted by zeta potential (**b**). PLGA can also serve as a sacrificial template for encapsulating cargo such as iron oxide nanoparticles (**d**).

#### 4.2.1.2 Reducing Agents

A variety of reducing agents were employed to produce homogeneous gold shells. Sodium borohydride was tried first but is much too strong and produced a substantial amount of free nucleated gold particles. Formaldehyde was attempted as well, however as a relatively strong reducing agent, this also produced substantial free nucleation in solution—this was also noted in Yang *et. al.*<sup>75</sup> when formaldehyde was utilized as a reducing agent for gold nanoshells over PLGA templates. It is important to note that the rate of solution based nucleation is a function of both the choice of reducing agent as well as the concentration of gold salt, with higher concentrations

leading to more spontaneous nucleation. This restriction made it difficult to provide sufficient gold salt to produce complete shells in a single reduction step without producing free nucleation. Formaldehyde was successful in generating gold shells, however as in Yang *et. al.*<sup>75</sup>, several cycles of reduction and washing by centrifugation were required to complete the shells and there was substantial debris from free nucleation and gold detachment during centrifugation in the final solution as can be seen in Figure 26.

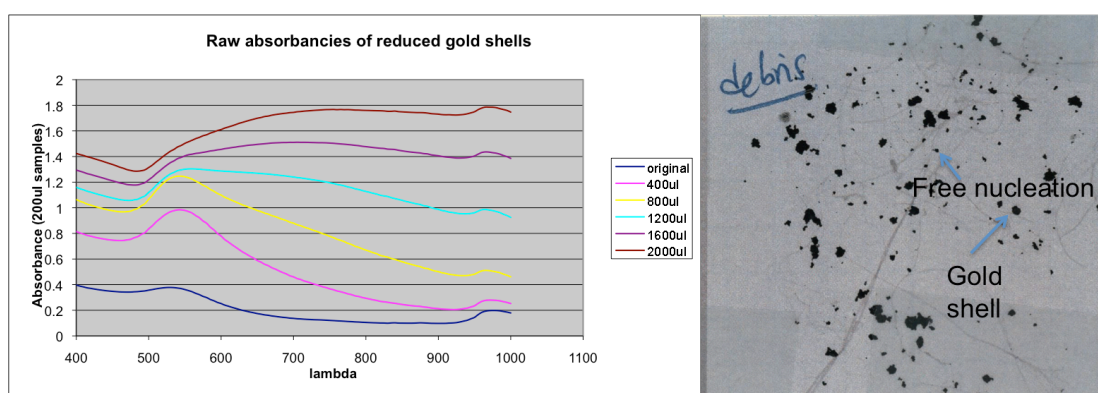


**Figure 26: Iterative Reduction of Chloroauric Acid on PLGA Templates by Formaldehyde.** The absorbance curves show progressive gold shell formation after iterative reductions (a). Between each consecutive volume, the samples were centrifuged and resuspended in reaction buffer. Shells did not begin to fully form until after several iterations and progressively larger gold particles would pellet with the PLGA-gold seeds resulting in substantial debris in the final preparation (b).

To address the issue of free nucleation, hydroxylamine was investigated as a reducing agent. Hydroxylamine ( $\text{NH}_2\text{OH}$ ) has been shown to demonstrate a near zero nucleation rate in free solution but a very rapid reduction rate on surfaces (especially gold seeds). It has been used to grow very precise increments on existing gold particles to nearly any desired diameter<sup>82</sup>. It is a natural extension to consider using this reducing agent for the production of gold shells as well. 5nm Au seeded PLGA nanoparticles were produced as before and added to mixed solutions of chloroauric

acid ( $\text{HAuCl}_4$ ) and hydroxylamine in water. It has been demonstrated that mixtures of hydroxylamine and chloroauric acid show no increase in absorbance after at least 20 minutes indicative of a near zero free nucleation rate<sup>82</sup>. Upon addition of gold seeded PLGA nanoparticles (initially red in color from the plasmon band of 5nm gold) the solution rapidly changed color to bluish gray indication formation of gold shells. It was possible to grow shells to any desired thickness or amount by adding subsequent stepwise amounts of both hydroxylamine and chloroauric acid under magnetic stirring or in a single step with any desired amount of initial gold salt. Note that at very high concentrations of either hydroxylamine or gold salt that free nucleation did occur, but these concentrations were not practically limiting given the amount of gold required to produce complete shells. Free nucleation will also occur rapidly in the presence of stabilizing agents such as citrate. However in water, even in unwashed samples, there was no observed free nucleation and samples without gold seeded PLGA resulted in either no color change, or deposition of pure gold on the stir bar (indicative of

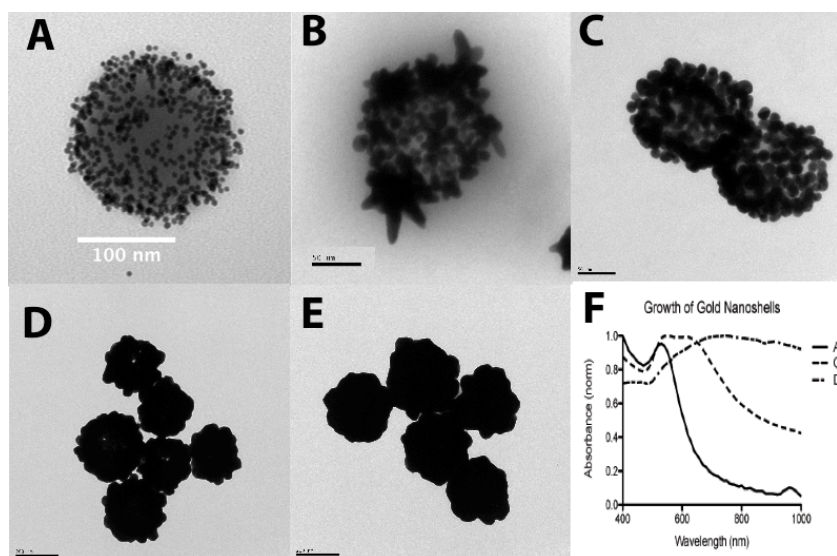


**Figure 27: Growth of Gold Nanoshells on PLGA Templates Using Hydroxylamine.** Growth reactions were done in single step reductions in water. Solutions of hydroxylamine and 1% chloroauric acid (2.5 $\mu$ L (b), 5 $\mu$ L (c), 10 $\mu$ L (d), 20 $\mu$ L (e)) were mixed vigorously and gold seeded PLGA was added. Reactions occurred nearly instantly and no free nucleation of gold was observed in any samples.

surface catalyzed reduction only) (Figure 29). Growth of gold shells in single reductive steps can be seen in Figure 27 along with corresponding absorbance profiles.

The morphology and homogeneity of the gold nanoshells produced by hydroxylamine reduction is also highly uniform and substantially cleaner than previous methods of producing gold nanoshells on PLGA templates. Figure 28 shows the homology difference between this method and published gold shell production on PLGA utilizing iterative formaldehyde reduction steps. The incomplete and spiky growth observed under low gold salt concentration (Fig. 27b) has been observed

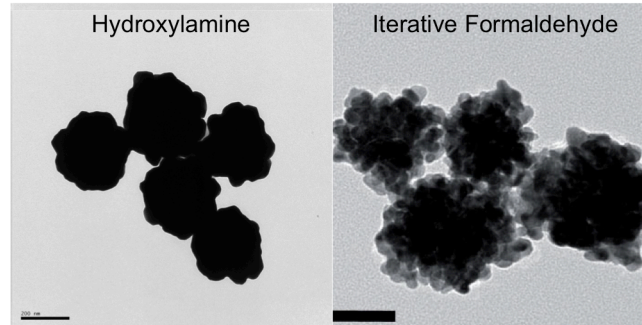


**Figure 28: Morphology Comparison of Gold Nanoshells on PLGA Templates With Hydroxylamine and Formaldehyde.** Hydroxylamine appears to produce not only more homogeneous shells, but it does so in a single, rapid reduction step with no free nucleation. Formaldehyde image taken from Yang *et. al.*<sup>75</sup>

previously in the production of gold shells as an anisotropic growth resulting from the limited availability of  $\text{Au}^{3+}$  ions in solution<sup>80</sup>. Even a slight increase in this concentration results in substantially more uniform growth (Fig. 27c). In addition there were two major observations made during the reduction process. Firstly, after the initial reduction, if the sample was allowed to magnetically stir for greater than 30 minutes, the particles began to aggregate in solution. And secondly, these aggregated particles began to rise to the surface and collect in a small bunch on the surface of the stirred solution.

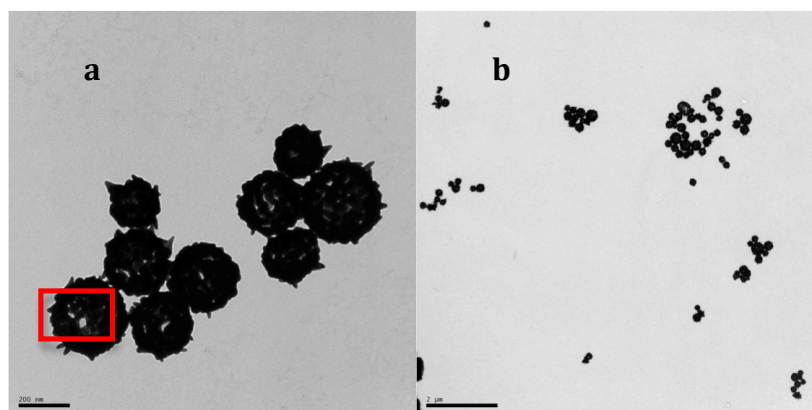


**Figure 29: Homogeneity of Unwashed Gold Nanoshells Produced with Hydroxylamine Revealing No Free Nucleation.** Gold nanoshells are produced over PLGA template particles as described in the text. The slightly spiky nature is a consequence of anisotropic growth characteristic of limiting  $\text{Au}^{3+}$  ions in solution and observed elsewhere<sup>80</sup>. Particles are completely free of spontaneous nucleation and are highly uniform **(b)**. The incomplete reduction appears to produce gold shells that are porous as well as hollow as no contrast can be seen through the open pores in the red box **(a)**.

It was noted that if these collected particles were subsequently sonicated, they would once again aggregate but instead settle on the bottom of the vial. The aggregation phenomenon is likely due to absorption of some of the excess hydroxylamine to the gold surface presenting relatively insoluble hydroxyl (-OH) groups to the solution. After reduction it was attempted to wash the particles and resuspend in a glycine buffer to replace the hydroxyl amine with a carboxyl amine and increase solubility. However, the amine-gold absorption energy is relatively strong ( $\sim 1.25\text{eV}$ ) and the exchange reaction was not sufficiently effective to stabilize the particles by charge. To overcome this it was necessary to introduce the much stronger thiol ligand ( $\sim 1.5\text{eV}$ ) and stabilize sterically with a 5kDa PEG molecule resulting in easily dispersible particles. The observation of the floating particles is a bit more

complex. However, from visually inspecting Figure 29a, the incomplete gold shell formed shows clearly defined pores that appear to be continuous through the particle indicating a hollow interior (see red box). It is known that PLGA degrades by acid hydrolysis<sup>83</sup> and the gold shell growth protocol involves the addition of chloroauric acid which reduces the solution pH to ~2 upon completion. It is possible that under these circumstances that the PLGA cores may have been degraded to a point where they could diffuse out of the formed gold cages. This result may also explain why the particles were observed to float to the surface of the reaction solution if allowed to stir for extended periods of time and why they would subsequently sink if sonicated. It may be surmised that the degradation of the PLGA from the gold shell core may allow for the diffusion of shorter PLGA polymers or lactic/glycolic acid monomers that would increase the porosity of the template particle and consequently decrease the overall density of the core (presuming that water would not rapidly diffuse in). This decrease in density may be sufficient to lend buoyancy to the particle as a whole resulting in their rising to the solution surface. This mechanism is conjecture, but if it is correct, it leads to a very natural method of producing homogenous, porous and hollow gold nanoshells in a highly reproducible manner and would be particularly useful for producing core/hollow structures with encapsulated nanoparticles such as the iron oxide cores seen in Figure 25.

As an additional point, to avoid free nucleation and produce the homogeneous gold shells as described in this dissertation, it is essential that the reaction be performed in water. There have been published protocols for the production of gold nanoshells with hydroxylamine in potassium carbonate buffer. Mixtures of

chloroauric acid with potassium are used to generate gold hydroxide ( $\text{H}_3\text{AuO}_3$ ) as the reductive precursor and also to provide a carbonate buffer. These protocols do generate gold nanoshells, however also produce substantial free nucleated gold that must be washed from the desired products<sup>73</sup>. In contrast, the reaction described above uses chloroauric acid itself as the gold precursor and is not buffered and results in zero free nucleated gold.

#### **4.2.1.3 Protocol For the Production of Gold Nanoshells on PLGA Templates**

A general process for the production of gold nanoshells over PLGA sacrificial templates is as follows. PLGA nanoparticles are produced via a nanoemulsion process. Briefly, 250 $\mu\text{L}$  of 31.5mg/ml ester terminated PLGA (i.v. .82) in chloroform is added dropwise to 1.5mL 2% 8-9k polyvinyl alcohol (PVA-80% hydrolyzed). This mixture is vortexed for 5 minutes and probe sonicated at 20W for 2 minutes, after which, chloroform is evaporated overnight resulting in PLGA encapsulating iron cores (PLGA-IOP). Particles are washed by centrifugation from free PVA and resuspended in 4mL water. 1mL is added dropwise to 2mL .5mg/ml 100kDa Poly L-Lysine (PLL) under magnetic stirring for 1 hour and washed by centrifugation. PLL coated particles are added dropwise to 5nm citrate stabilized gold seeds (BBInternational) and allowed to bind for 3 hours and washed by centrifugation to remove unbound gold. Au seeded particles are resuspended in 100 $\mu\text{L}$  water. Varying amounts (specified in figures) of 1%  $\text{HAuCl}_4$  (29.5mM) is added to 62.5 $\mu\text{L}$  40mM hydroxylamine hydrochloride (prepared fresh) in 2mL water under magnetic stirring. Aliquots (50 $\mu\text{L}$ ) of gold seeded PLGA are then added and the reaction was mixed for 5 minutes after which

either more hydroxylamine and HAuCl<sub>4</sub> were added or particles were centrifuged to wash. The color change from light pink to gray/blue was achieved within 1 minute. Particles were either left to stir for several hours (to observe aggregation and buoyant behavior or were collected by centrifugation and resuspended in .8mL of water with 200μL of 5mg/mL thiolated polyethylene glycol (PEG5k) and 2μL triethylamine as a proton scavenger. PEG samples were stirred for 2 hours, centrifuged and redispersed stably in water.

#### 4.2.2 Galvanic Replacement

The second major approach for the production of gold nanoshells is galvanic replacement. This process is based on the differing electrode potentials of gold (chloroauric acid) with a variety of other metals, silver being particularly common.

**Table 3: Standard Electrode Potentials of the Two Half Reactions of Galvanic Replacement of Silver With Gold.**

$\text{Ag}^+ + e^- \rightleftharpoons \text{Ag}(s)$	+0.7996
$[\text{AuCl}_4]^- + 3 e^- \rightleftharpoons \text{Au}(s) + 4 \text{Cl}^-$	+0.93

For the spontaneous reaction, the Gibbs free energy ( $\Delta G = -nFE_{\text{cell}}$ ) must be negative, so  $E_{\text{cell}}$  must be positive, resulting in Ag(s) donating electrons to Au<sup>3+</sup> and producing solid gold that “replaces” the silver oxidizing it to Ag<sup>+</sup>. The reaction typically utilizes silver nanoparticles as templates and most commonly takes place in boiling water under reflux. The initial steps of the reaction create an Au/Ag alloy on the surface of the template particle. Published data has shown that the reactions have

an increased rate at defect points (or points of higher surface energy) on the surface and that these become the active sites<sup>84</sup>. Ag atoms in the bulk migrate to these points and become oxidized by  $\text{Au}^{3+}$  ions, resulting in the deposition of solid gold and the dissolution of the bulk silver. This process continues until the bulk silver is all dissolved at which point a dealloying of the surface shell ensues. The stoichiometry of the reaction is 3:1 (Ag: Au) by electron balancing. The result is that as Ag atoms are dealloyed from the surface, they leave excess vacancies that Au atoms migrate to fill in order to lower the total surface energy.

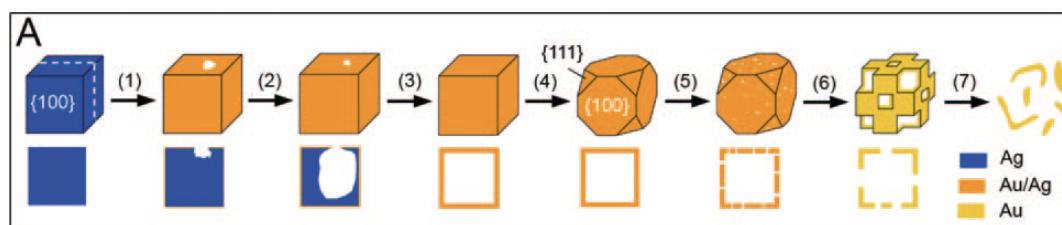


**Figure 30: Schematic of the Galvanic Replacement on Silver Nanocubes.**

Addition of gold ions increases to the right. Initially the surface of the cubes forms an alloy of Ag/Au and a defect site forms which becomes the active site. After bulk silver dissolution, dealloying of the shell begins. The vacancies left by the 3:1 stoichiometry of Ag: Au causes Au atoms to merge into ridges producing large holes in the shell that eventually can lead to complete shell breakage<sup>85</sup>

This process results in large holes produced in the shell that produces a more cage like structure and produces gold ridges<sup>84</sup>. If the process continues farther, the Au ridges will continue to merge and may result in structural instability and breakage of the shell releasing small clumps of gold. The reaction can be seen schematically in Figure 30.

Galvanic replacement reactions for the production of gold nanoshells and further of gold nanocages has several advantages. First, it is easier to produce shells

of any desired size. In contrast to a seeding mechanism where seed size to template size is a concern for homogeneity of the produced shells, as is getting high enough seeding densities, the galvanic replacement reaction can produce gold shells of any size or shape that a template particle can be produced in. Silver nanoparticle production of a variety of sizes and shapes is a mature field and gold nanoshells may be made from any of them. A second advantage is the natural production of nanocage structures as the reaction proceeds. Nanocages are unique structures that are taking a more prominent role in nanotechnology particularly for their ability to encapsulate larger particles while not restricting solution access to the core. It is possible to create nanocage type structures using seeded growth (Fig. 29) as well, however it is more difficult to control the balance between seeding density, reductive growth and homogeneity, and additionally requires dissolution of the template structure to create a hollow cage. Porous gold shells have also been produced over hydrogen nanobubbles in a completely distinct electrochemical process however, the pores formed in this process are much smaller than those achievable with the galvanic replacement reaction<sup>86</sup>. A third advantage of the galvanic replacement reaction is the potential to form core/shell structures or multi-layered structures by continued silver deposition and gold replacement. The production of a gold/silver alloyed shell readily serves as a template for further silver deposition that can be used in subsequent replacement reactions<sup>87</sup>. A summary of the products of the galvanic replacement reaction as produced over silver nanoparticles can be seen in Figure 31.

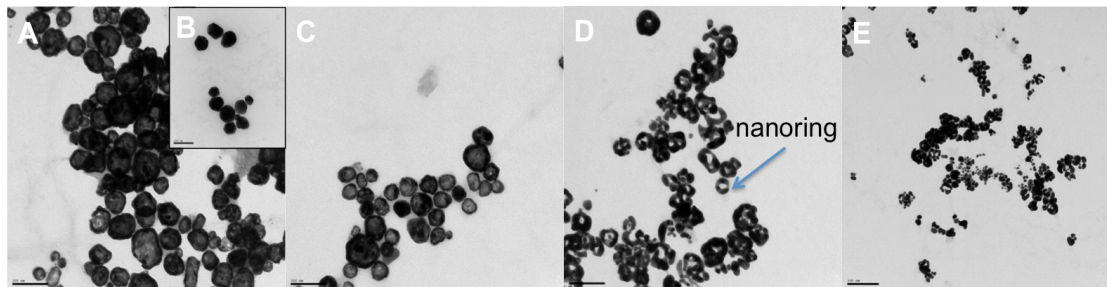


**Figure 31: Images of Gold Nanoshells/Nanocages Produced by the Galvanic Replacement Reaction.** Silver template nanoparticles (b) are refluxed in water with increasing amounts of 1mM chloroauric acid. 1mL (a), 2mL (c), 3mL (d), 4mL (e). The gradual hollowing out of the cores can be seen in (a) and (c). By (d), the gold ridges have formed and merged producing large holes and nanoring structures (SEM in Figure 32). Further addition results in structural breakage of the shells (e). Scale bars are 100nm for (a)-(d) and 200nm for (e). Absorbance profiles for these structures can be seen in Figure 34

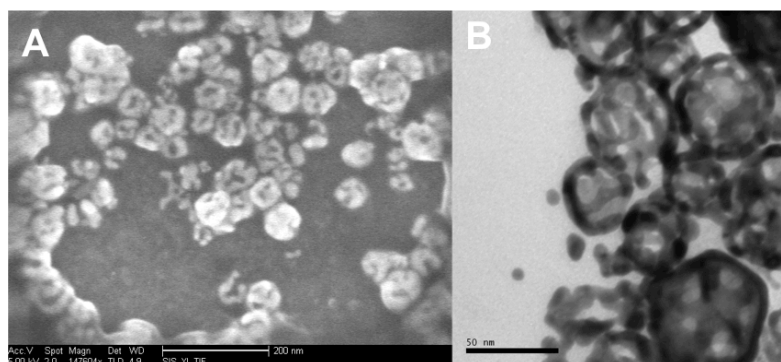


**Figure 32: SEM and TEM of Gold Nanocages.** Both surface details as well as transmitted details of gold nanocages produced via the galvanic replacement reaction

In principle it is possible to tune the size of the holes produced in the gold shells as well as the shell thickness and degree of Ag(s) replacement, however, not independently. The migration of Ag/Au atoms, the formation of ridges and pores by alloying/dealloying and the degree of Ag(s) dissolution are all dependent on each other and a degree of heterogeneity was seen in all nanocage samples produced. Parts of each sample exhibited very little replaced silver while other particles showed

extensive dealloying and gold ridge formation to the point of forming two dimensional ring like structures that lose the “cage” like properties, including the NIR absorbance of the gold shells as seen in Figure 34.

A note about the silver nanoparticle template size vs. the gold shells thickness: given the stoichiometry, molecular masses, and densities, if one were to consider that the gold shell is deposited uniformly around the template, the plot of the shell thickness vs. initial template size is linear as seen in Figure 33. This means that a 40nm silver template would contain enough silver to produce a 2nm gold shell if totally replaced. Practically this does not occur as the shell is not uniform due to Au ridge formation as atoms merge to fill the vacancies left by Ag with the result being areas of substantially thicker gold and completely open holes. Practically this is an important concept to keep in mind when one considers producing gold shells via

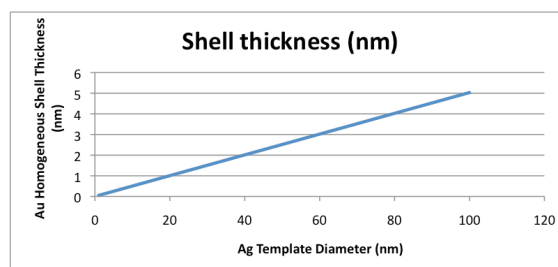


**Figure 33: Ag Template vs. Gold Shell Thickness for Homogeneous Galvanic Replacement.**

galvanic replacement on very small Ag templates as the amount of gold that can actually be deposited on the particles may not produce structurally sound shells and in fact it was later noted that all structurally sound shells produce on this size scale are likely Au/Ag alloys and not pure Au.

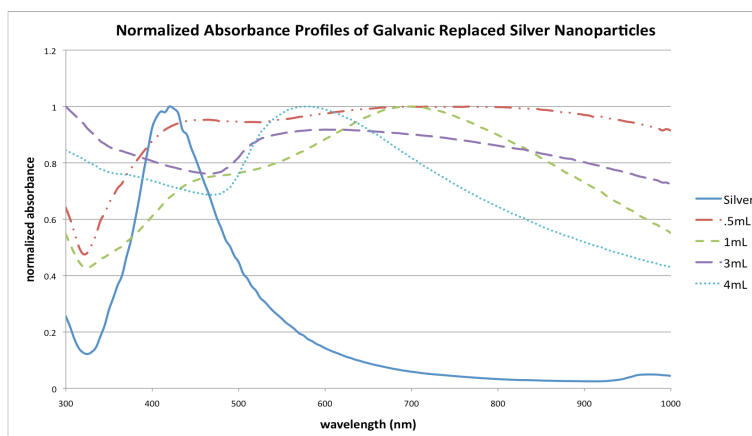


**Figure 34: Absorbance Profiles of Galvanic Replaced Samples in Figure 31.** Tracking the normalized absorbance of gold shells produced by galvanic replacement on silver nanoparticles. Initial silver nanoparticles has a strong Plasmon absorbance peak at 410nm. With increasing chloroauric acid, the silver plasmon peak at 410nm becomes diminished and the NIR peak of gold shells increases. Further increasing gold ion replacement results in degradation of the gold shell, decreased NIR absorbance and ultimately fragmentation into large gold particles as indicated by the rise in the peak between 580-600nm in the 4mL sample.

#### 4.2.2.1 Protocol For Galvanic Replacement Reaction

Polyvinylpyrrolidone (PVP) stabilized silver nanoparticle templates are produced via the polyol reduction method. 1.36g of 10kDa PVP are dissolved in 10mL ethylene glycol and heated to 160C in an oil bath. .17g  $\text{AgNO}_3$  is dissolved in 10mL ethylene glycol without using heat. If heat is used the solution will turn yellow indicating the formation of silver nanoparticles. This solution is added dropwise to the heated PVP solution and stirred for 4 hours at 160C in the dark. Particles formed are collected and precipitated in acetone (5:1 volume ratio). After washing and drying of acetone, particles are resuspended easily in water.

The galvanic replacement reaction is straight forward. PVP silver particles are refluxed for a few minutes in boiling water.  $\text{HAuCl}_4$  in water is added dropwise

slowly to the vigorously stirred solution. There is an immediate color change as the surface alloy forms. After all the solution is added the solution is refluxed for an additional 20 minutes to allow full atomic migration and shell formation. Slight color changes were observed over this time period. The sample is cooled and a saturating amount of NaCl is added to dissolve the AgCl and clarify the solution. Nanocages are washed via dialysis or centrifugation and dispersed in water.

### **4.3 Conclusions**

The advantageous properties of gold both as a chemical and in a variety of nanostructural conformations will continue to make it an attractive candidate component for many biological applications. In particular, its relatively favorable biological inertness makes gold well suited towards biological interface surfaces. As a component of nanostructures for biological use it is therefore natural to consider gold as a protective shell.

The synthesis of such shells occurs primarily by two mechanisms that are fundamentally different. Gold shells produced by the reductive growth of a gold salt onto gold nanoparticle seeds can generally be formed over any nanoparticle surface to which these seeds can be conjugated, most commonly silica or polymers, and in the latter case serves as a natural mechanism for producing gold shells around encapsulated cargo such as drugs or other smaller nanoparticles. Important factors in the production of homogeneous gold nanoshells via the reductive method include the density of initial seeding and relative ratios of seed to template size, choice of reducing agent, buffer pH and concentrations of seeded templates, reducing agent and

gold precursor salts. The balance of these values is of critical importance to achieve clean production of nanoshells devoid of spontaneous nucleation that would contaminate the sample. This chapter presents a method of gold nanoshell production utilizing hydroxylamine as a reducing agent that simplifies many of the above variables by possessing an extremely low free nucleation rate while retaining a robust reduction rate on surfaces such as gold seeds. Moreover, this chapter presents a simple mechanism for the production of gold nanoshells over PLGA emulsions which allow for the encapsulation of a variety of cargoes such as iron oxide nanoparticle cores. The simplified reaction takes place in water and produces perfectly homogeneous gold nanoshells over PLGA templates without substantial concern over seeded particle, gold precursor, or reducing agent concentration as hydroxylamine does not readily reduce gold precursors alone in solution. This greatly simplified protocol is applicable to any production of gold nanoshells that takes place via seeded growth. It is also of note that this method is also able to produce gold nanocages—or porous gold shells—via the incomplete reduction of gold shells. The natural heterogeneous distribution of gold seeds will allow some to merge while other do not, leave open pores such as is seen in Figure 29. The production of nanocages by this mechanism is, however, a delicate balance of concentrations to achieve the desired pore size coupled with shell integrity as structurally sound complete shells are not formed. It is also important to note that the dimensions of both the gold shells as well as the pore sizes produced in this manner are limited by the physics of PLGA emulsion formation and initial gold seed diameter. The ability to encapsulate nanoparticles in polymer templates that serve as scaffolds for gold shell production

possess as a lower limit the minimum size of effective homogeneous emulsions that the polymer can form while encapsulating the desired cargo as well as the template to seed size ratio that will be important for determining the homogeneity of the gold shells formed. Practically, for PLGA emulsions, this places a lower limit of ~50nm for gold shell size produced via this mechanism<sup>88</sup>. The limitation of homogeneity as determined by ratio of template to seed size may be able to be circumvented by a variety of ways (some of which are discussed in Chapter 5) which allow for the deposition of metals directly onto PLGA surfaces, though to my knowledge, no demonstration of this type of direct coating has been shown. An additional comment on the use of PLGA sacrificial templates for the encapsulation of iron oxide nanoparticle cores is that such cores would necessarily be coated in organic stabilizing ligands to be soluble in the emulsions. This may prove to be an obstacle to the aqueous interaction necessary for an effective contrast agent once the PLGA template is removed.

The second major route to producing gold nanoshells is via galvanic replacement. This approach involves the electrochemical reaction by which metallic precursors such as silver preferentially donate their electrons to reduce a gold salt. The reaction forms a gold/silver alloy on the template surface, proceeds to dissolve out the template core as more gold is deposited on the surface and ultimately dealloys the hollowed out shell with even further increasing gold deposition. Major advantages of this approach include 1) its ability to produce gold nanoshells over any sized silver template particle or shape that can be made (including rods, spheres, boxes, etc., 2) its natural production of hollow shells in a homogeneous way devoid of any free gold

formation as the reaction can only take place on template particle surfaces, 3) the ability to produce shells with large pores that resemble nanocages through increased dealloying of the shell and subsequent gold migration/consolidation resulting in large pores and 4) the ease of the reaction to perform. It appears like all stable gold shells produced by galvanic replacement (at least in the size range discussed in this chapter) are in reality still alloys of gold and silver since when the reaction is pushed farther to completion and more silver is dealloyed from the shell, they eventually lose integrity and break. This would indicate that shells made entirely of gold do not exist in this size range studied. It is also important to note that this method of production always results in a small degree of heterogeneity in the sample as some particles exhibit substantially more gold consolidation in the shell than others and indeed lose their nanocage type structures forming nanoring structures. This would be problematic for any synthetic protocol that required the encapsulation of cargo. Nevertheless, this method of producing gold nanoshells and nanocages is highly efficient and produces structures in a robust and simple manner that have unique optical properties making them useful for a variety of applications.

## CHAPTER 5:

# CORE/HOLLOW SHELL NANOSTRUCTURES OF IRON OXIDE AND GOLD

### 5.1 Introduction/Rationale

The interaction of nanoparticles and of nanotechnology in general with biological systems is a highly complex interplay of chemistry and physics that takes place at the nanoparticle (or synthetic) surface. It is nice to think that when we design nanostructures for *in vivo* (or even *in vitro*) use, that the surface functionalities that we conjugate will be effective and displayed as we imagine, however, in reality, the interaction of nanoparticles with biological systems is better characterized by Figure 35 as proteins and biomolecules bind and release to the nanoparticle surface in both close and loose interactions.

Many surface functional groups such as poly-ethylene glycol (PEG) have been added to nanoparticles to reduce this opsonization and increase circulation half life (or cellular uptake)<sup>29</sup>, however, the interactions are still quite complex. This biological interaction is particularly prevalent for nanoparticles made of biologically active molecules such as iron oxide. For iron oxide nanoparticles, this can substantially

decrease the circulation times *in vivo*<sup>89</sup>, however, for many applications, a long circulation is desired and, in fact, necessary for efficacy. To extend the circulation times for more effective imaging and drug delivery, several approaches have been

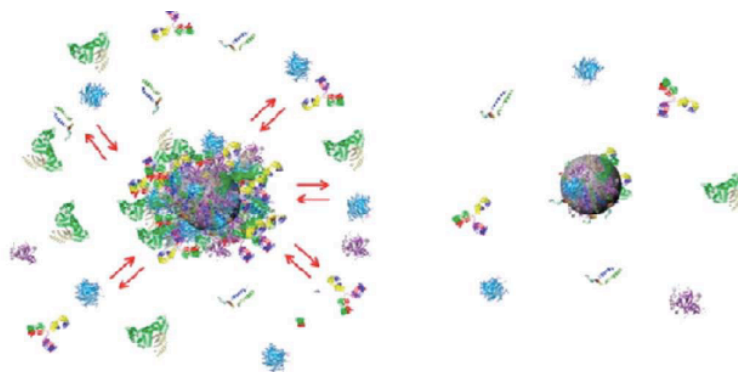


**Figure 35: Visualization of the Interactions of Nanoparticles With Biological Solutions.** Nanoparticle/protein interactions are characterized by two distinct domains. 1) A tightly bound, thin protein layer and 2) a loosely bound thick protein corona of exchangeable entities<sup>52</sup>

taken to coat and protect the iron oxide surface from protein adsorption, including crosslinked dextran (commercially available as Feridex), PEG<sup>89</sup>, noble metals such as gold<sup>90</sup>, silica<sup>64,91</sup> or a variety of polymeric encapsulations<sup>92</sup>. Each of these methods is designed to achieve the same goal--physically separating the iron oxide surface from the solution environment by a biologically inert barrier such that protein adsorption is limited. While this approach can be useful for increasing circulation, it can have a major impact on the one of the major applications of iron oxide, namely its utility as an imaging contrast agent. There have been several published results describing the magnetic effects of iron oxide coatings. For example, solid coatings of silver, gold, and silica have shown very large decreases in saturation magnetization values against bare iron oxide NPs in excess of 90%<sup>64,90,93</sup>. This is a direct effect on the ability of the

iron oxide to respond to externally applied magnetic fields, however, this is only one half of the characteristics that compose an efficacious imaging contrast agent, the other half being the agent's ability to impart that field to local protons in the bulk solution<sup>54</sup>. There are two fundamental aspects of this latter criteria: 1) The proximity of local water protons to the iron oxide such that they can be affected by the field and 2) the ability of these local protons to be rapidly exchanged with the bulk solution to provide for a bulk contrast effect<sup>54</sup>. In the case of solid coatings on iron oxide, the proximity criteria of aqueous protons is limiting as physical shells separate the iron oxide from the nanoparticle surface, however it may be conjectured that these water molecules at the surface are not impeded from exchanging with the bulk solution. In the case of iron oxide compositions that are stabilized by highly hydrated PEG or dextran layers, the situation is reversed. There is very close interaction of water with the nanoparticle surface, however this water is not permitted active exchange with the bulk solution as it remains tightly bound in the dense and highly hydrophilic polymer layers close to the nanoparticle surface that do not allow its bulk exchange at an appreciable rate<sup>94,95</sup>. Published results have demonstrated that the thickness of the PEG corona layer significantly affects the MR relaxivity and off resonance saturation of superparamagnetic iron oxide<sup>96</sup>. Additional research has determined that increasing the thickness of PEG layers on iron oxide results in a dramatic drop in the  $r_2$  relaxivity rate for which iron oxide nanoparticles are commonly employed and argues that thinner coatings are highly desirable from an imaging perspective<sup>97</sup>. From this it may be surmised that the same effect occurs with the crosslinked dextran in commercial iron oxide contrast agents where iron oxide cores may be  $\sim 10\text{nm}$  in diameter but

coatings may reach hydrodynamic radii of up to 140nm<sup>59</sup>. This substantial separation may have dramatic effects on the efficacy of iron oxide nanoparticles as imaging agents.

## **5.2 Criteria for Effective Magnetic Imaging Particles for *In Vivo* Utilization**

Therefore, one can propose four main criteria for effective iron oxide nanoparticle imaging agents.

- 1 There must be very close interaction of the iron oxide surface with the solution based protons (principally hydrogen nuclei of water)
- 2 These protons must be rapidly and freely exchangeable with the bulk solution
- 3 There must be no surface coatings that substantially diminish the magnetization saturation of the iron oxide
- 4 There must be an effective mechanism of shielding the iron oxide from cellular uptake so as to increase circulation time

## **5.3 Iron Oxide/Gold Core/Hollow Porous Shell Structure**

An elegant method of addressing each of these requirements is a core/hollow shells structure as seen in Figure 36. The components of this structure allow for several benefits. The outer shell is composed of gold, which has been shown to be highly biocompatible<sup>98</sup> and can further be functionalized with a variety of

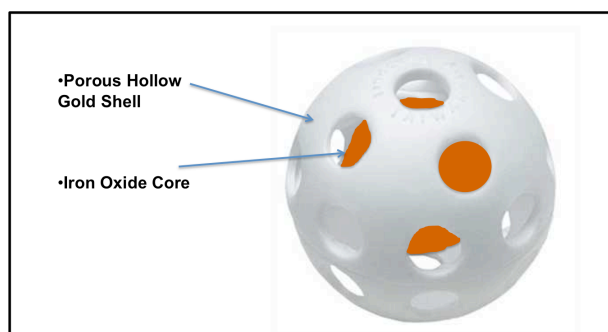


**Figure 36: Core/Hollow Shell Iron Oxide/Gold.** This structure addresses many of the criteria necessary for an effective *in vivo* MRI contrast agent. The gold shell presents a biocompatible surface that shields the encapsulated iron oxide core from surfaces, preventing its uptake by cells, while being sufficiently porous to allow free solution access to the core. In this manner, the iron core oxide surface is not impeded in any way from interaction with aqueous protons that are also freely exchangeable with the bulk solution while not being susceptible to premature cellular uptake.

ligands such as PEG that will extend the circulation and targeting capabilities.

Additionally it is both hollow and porous which allows free solution based access to the interior which contains a superparamagnetic iron oxide core. The shell protects this core from cell and surface base interaction while allowing close solution based interaction and obviates the need for thick protecting layers on the iron oxide itself as the important protecting layers for the evasion of endocytosis would only reside on the gold surface. A further advantage of this structure is that the whole particle may be produced to have a small hydrodynamic radius of  $\sim 30\text{nm}$  which is presumed to be advantageous for effective biodistribution<sup>99,100</sup>. By avoiding the need to have very thick polymer layers on the iron oxide, the gold shell may be functionalized with a thin PEG layer to provide enhanced circulation time. The final dimensions of the particle are then determined by the spacing between the iron oxide core and the gold shell and can be altered based on this distance.

Each of the components of this structure has been outlined in previous chapters. Chapter 3 discusses the production of aqueous stable superparamagnetic iron oxide nanoparticles with a surface functional group that does not increase hydrodynamic radius and has minimal effect on saturation magnetization and Chapter 4 covers the synthesis of hollow and porous gold nanoshells. A combination of these two elements could potential produce the desired structure. It is, in principle, possible to create the types of structures from both gold shell approaches (seeding and galvanic replacement). However from a practical perspective and considering that it is desirable to keep the whole structure as small as possible for effective biodistribution<sup>99</sup>, the seeding approach is likely not a realistic approach. While the process of creating core/shell structures by encapsulating cargo in sacrificial polymer templates such as PLGA and subsequently growing metallic shells is straightforward, the homogeneity of the shells produced is a function of the template to seed size, placing a practical lower limit on the size of shells that can be produced with this method. Additionally, with the requirement that the pores be less than ~10nm (smaller than the encapsulated iron oxide cores which must reside in the superparamagnetic domain (~<20nm), a seeded approach toward growing porous gold nanoshells over PLGA encapsulating superparamagnetic cores is impractical. However, the galvanic replacement reaction can produce gold shells of any desired size and naturally forms nanometer sized pores that are of an adequate size to retain superparamagnetic iron oxide cores. For this reason, a combination of the iron oxide synthesis described in Chapter 3 was combined with the galvanic replacement reaction for the production of

porous gold nanoshells described in Chapter 4 to produce the desired structure seen in Figure 36.

#### **5.4 Iron Oxide/Gold Core/Hollow Shell Synthesis Via Galvanic Replacement**

The first step to combining the synthesis of iron oxide with hollow gold shells is to coat the iron oxide with a sacrificial silver shell that will serve as the fuel to generate the subsequent gold nanoshell. There are a variety of methods for noble metal coating which were attempted with varying levels of success as described below.

#### **5.5 Summary of Silver Coating of Iron Oxide Methods**

Similar to the gold shell growth discussed in Chapter 4, there are two principle means of growing silver nanoshells: template seeding followed by reduction growth, or direct reduction on the nanoparticle surface. A summary of the possible mechanisms is described as well as their applicability to the iron oxide nanoparticles discussed in Chapter 3.

##### **5.5.1 Nanoparticle Seeding Mechanisms**

For CSIOP averaging  $\sim 8\text{nm}$  in diameter (Fig. 18) and a desired final nanoparticle size of  $\sim 30\text{nm}$  it is impractical to consider a silver or gold nanoparticle seeding with 2-5nm seed particles such as was described in Chapter 4 regarding gold shell growth, as seeds would be roughly the same order as the particles and their growth would likely result in uneven coatings and thicker shells than desired.

However, there are a variety of atomic seeding mechanisms that do not utilize complete particles, but rather atoms that have been described as noted below that may be able to provide the desired nucleation sites.

#### 5.5.1.1 Sn<sup>2+</sup> Seeding

One approach to coating nanoparticles with noble metals is through an ionic seeding mechanism involving SnCl<sub>2</sub> sensitization. Briefly, negatively charged templates are mixed with SnCl<sub>2</sub> in highly acidic conditions (to prevent Sn<sup>2+</sup> oxidation to Sn<sup>4+</sup>) such that the Sn<sup>2+</sup> ions adsorb onto the nanoparticle surface. Washed particles are then mixed with aqueous solutions of Ag[NH<sub>3</sub>]<sub>2</sub><sup>+</sup> ions and a redox reaction occurs at the template surface reducing Ag<sup>+</sup> to Ag(s) and oxidizing Sn<sup>2+</sup> to Sn<sup>4+</sup> resulting in the deposition of Ag(s) seeds on the template surface<sup>101,102</sup>. This method of seeding is not practical as iron oxide templates are not stable in acidic pH (Fig. 22)

#### 5.5.1.2 Ag[NH<sub>3</sub>]<sub>2</sub><sup>+</sup> Adsorption and Reduction

Published methods of silver seeding have also been demonstrated with direct Ag[NH<sub>3</sub>]<sub>2</sub><sup>+</sup> ion adsorption followed by NaBH<sub>4</sub> reduction to produce silver seeds that could subsequently be grown to produce shells. This method was attempted as published in Sanchez-Gaytan *et. al.*<sup>80</sup> and did not result in any observed silver nanoparticle seeding by either TEM or absorbance and consequently was not pursued as a growth strategy.

## 5.5.2 Direct Reduction on CSIOP Surface

Atomic seeding and nanoparticle seeding mechanisms did not appear to provide the desired coatings, so the alternative is direct reduction of silver onto the CSIOP surface. A variety of approaches were attempted to coat CSIOP with uniform layers of silver via direct reduction.

### 5.5.2.1 Formaldehyde, Ascorbic Acid, Hydroxylamine, Citrate

There have been several reports of direct coating of iron oxide with gold<sup>90,103</sup>, however, substantially less with silver. The choice of reducing agent is of particular importance when attempting any direct reductions on surfaces as free nucleation is to be avoided and uniform coatings are desirable. For gold coatings, combinations of hydroxylamine and glucose have proven to be very effective<sup>103</sup>, confirming the observations seen in Chapter 4 regarding gold surface reduction facilitated by hydroxylamine, however, the effectiveness of hydroxylamine for surface catalyzed silver reduction is substantially less specific and results in substantial free nucleation as well—note that hydroxylamine will also result in free gold nucleation in the presence of stabilizing agents such as citrate. It is possible that the different effect between gold surface catalyzed reduction and silver reduction by hydroxylamine is a result of the different oxidation states of  $\text{Au}^{3+}$  and  $\text{Ag}^+$  and the number of localized molecules of hydroxylamine required to reduce the metal to a solid. If the presence of more than one molecule of hydroxylamine will reduce gold more rapidly then it may be that hydroxylamine concentrates on surfaces via amine interaction and preferentially

reduces gold locally while for silver a single molecule in solution is sufficient resulting in no surface preference.

Various reduction attempts with formaldehyde, citrate and ascorbic acid did not yield uniformly coated CSIOP, and resulted in substantial free aggregation or nucleation. It is important to note that nanoparticle coating and synthesis is as much an art as it is a science. It is conceivable that there are recipes utilizing these reducing agents that would result in homogeneous shells of silver over CSIOP, however, the number of variables make optimization extremely difficult. Additionally, the surface characteristics of the iron oxide itself plays a large role in the deposition of metals. I would, however, note that I have seen no published literature of direct silver coating of carboxyl functionalized iron oxide achieved with any of these reducing agents in the absence of an initial seeding mechanism. There has been a report of platinum coating of amino silane functionalized maghemite using hydrazine hydrate as a reducing agent<sup>104</sup>, however, the stabilization of iron oxide detailed in Chapter 3 was not successful with amino silanes and the reported coating did not produce complete shells as determined by the energy dispersive x-ray spectrum<sup>104</sup>. Additionally silver coating of platinum particles has been reported in the presence of citrate stabilizers with a photoreductive mechanism<sup>105</sup>, however, it has also been observed that photoreductive synthesis of silver nanoparticles can proceed in solutions of just silver nitrate and citrate—an observation that was also noted in the next section and results in substantial free (and stable) silver nucleation and is therefore also unsuitable for this application<sup>106</sup>.

### 5.5.2.2 Photoreduction

It was noted during various synthetic attempts that silver particles would form spontaneously if solutions were left out on the bench for extended periods of time.

These particles would form discrete nanoparticle suspensions that could be dispersed

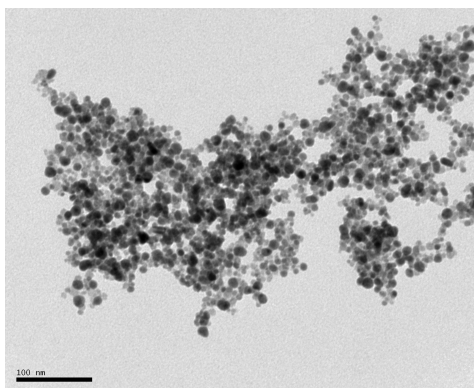


**Figure 37: Photoreduction of  $\text{Ag}^+$  on CSIOP Templates.** TEM image of iron oxide nanoparticles incubated with silver nitrate under UV irradiation in the absence of other stabilizing agents. The photoreduction of silver nitrate in the presence of iron oxide seeds produced discrete particles that could be separated by sonication but aggregated in time. Photoreduction of silver nitrate in the absence of iron oxide particles produced large aggregated clumps that rapidly fell out of solution.

by sonication in the presence of iron oxide templates, but would form large aggregates that precipitated in their absence. It has been published that ethylenediamine tetraacetic acid (EDTA) is able to catalyze metal reduction on the surface of oxide particles ( $\text{TiO}_2$ ) under ultraviolet light<sup>107</sup>. It is presumed that since the carboxy silane utilized in the iron oxide core stabilization is similar in chemical structure to EDTA that a similar mechanism was taking place resulting in the production of silver nanoparticles. The reaction could be dramatically sped up under a mercury lamp and a representative image of photoreduced silver on CSIOP may be seen in Figure 37. The image may be compared at least morphologically to iron oxide in Figure 18. Silver

possesses a higher electron density and would appear as darker in transmission microscopy. Absorbance spectra indicated the formation of silver particles with a 410nm plasmon resonance band. The particles were not stable in the absence of stabilizing molecules (such as citrate) and aggregated with time, however after reduction, particles could be stabilized by sonication in the presence of citrate to form stable suspensions. However, the presence of citrate prior to reduction resulted in free and stable nucleation of silver particles under UV light even in the absence of iron oxide templates—this has also been previously observed<sup>106</sup>. This process was not ultimately chosen and there was therefore no subsequent characterization.

#### **5.5.2.3 Glucose Reduction and Silver Shell Growth**

The difficulties of producing conformal metallic shells on such small nanoparticle templates while at the same time avoiding free, spontaneous nucleation necessitates a very gentle approach. It was seen that reducing agents such as formaldehyde, ascorbic acid, citrate and hydroxylamine were not suitable for clean shell formation, however, even weaker reducing agents exist that may prove useful. Glucose is one agent that has been shown to be sufficiently weak so as to catalyze only surface based reduction on iron oxide nanoparticles<sup>93</sup>. However, even this was not as straight forward as the published protocol and it was discovered to that achieve any appreciable amount of reduction, the reaction must also be heated and even at that elemental analysis demonstrated that only ~2% of the available  $\text{Ag}^+$  ions were reduced after 3 hours, and 4% in overnight incubations. The presence of the silver particle formation on the iron oxide can be seen clearly in Figure 38 by transmission electron

microscopy and the clean plasmon resonance at 410nm as well as the appearance of a silver peak in the x-ray diffraction pattern. It is noticeable from the fact that the iron oxide peak does not fully disappear that the particles are not fully coated, but perhaps only seeded. ICP-MS quantification of both iron oxide and silver concentration of silver seeded CSIOP would indicate that the amount of silver that was reduced was sufficient to only form a conformal shell of .35nm assuming an average iron oxide particle diameter of 8nm. Give this, it would be very difficult to resolve in TEM and since real films are not conformal, would also likely explain the exposed iron oxide still observed in the x-ray diffraction pattern (Fig. 38).

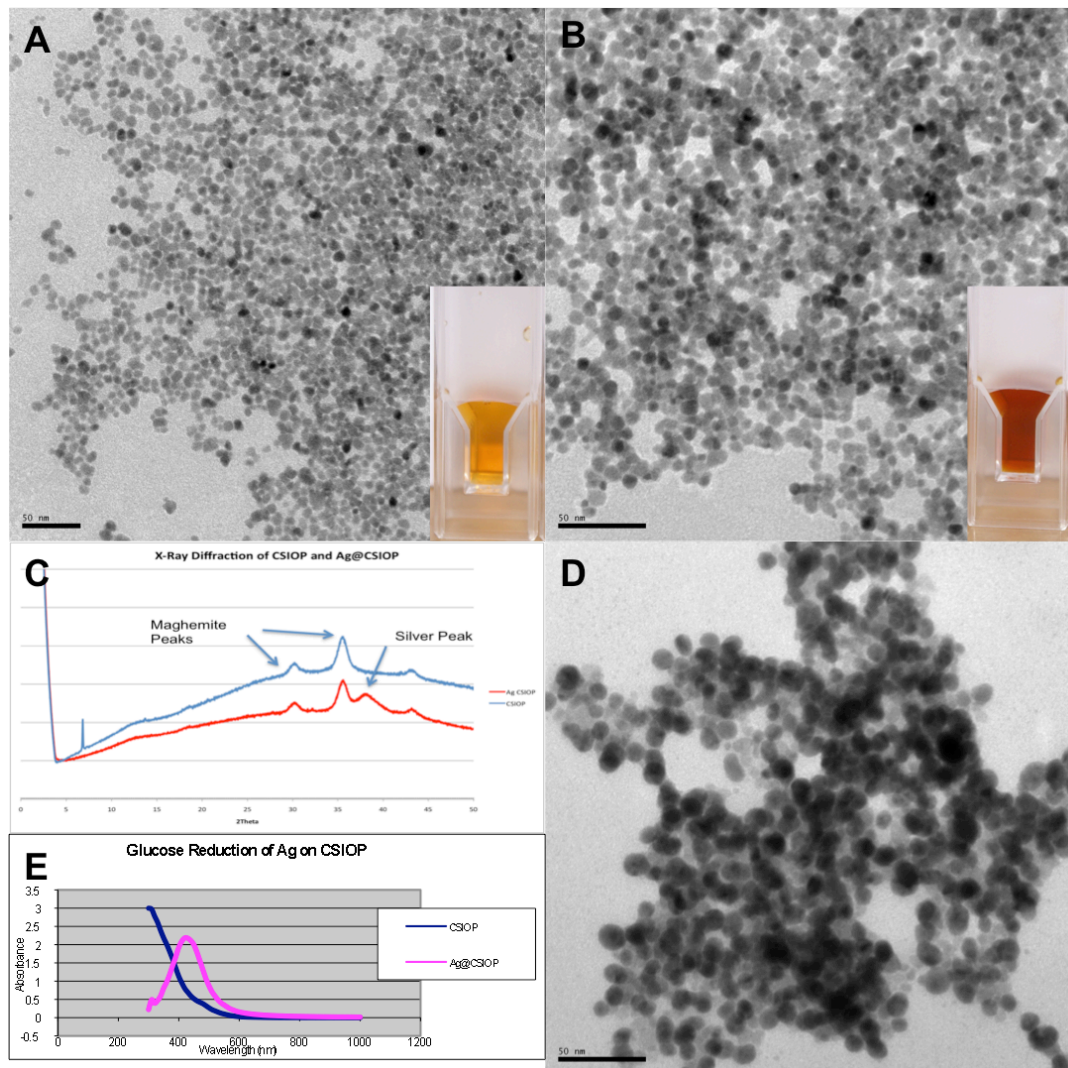


**Figure 38: Characterization of Silver Coated Iron Oxide Nanoparticles Produced Via Glucose Reduction.** Transmission electron microscopy images and photographs of stable CSIOP and silver seeded CSIOP **(a)**, **(b)** respectively. The X-ray diffraction pattern of each sample was taken to determine if the particles were fully coated. The maghemite peaks does not disappear, but a silver peak is seen in the reduced sample. This may indicate that the particles are seeded but not entirely coated **(c)**. The presence of these silver particles is also see by the strong 410nm plasmon band in **(e)**. The silver seeded particles in **(b)** are grown in a homogeneous and stepwise fashion via the protocol described in the text **(d)**.

The silver seedings obtained on the iron oxide nanoparticles could subsequently serve as rapid nucleation sites for the further reduction of silver as silver nanoparticles catalyze silver reduction much faster than solution based nucleation. The ultimate size of the nanoparticles is a function of the desired gold shell size and stability as noted in Figure 33. The total amount of silver available for replacement will be an important factor in the ultimate shell formation. It is also important in this step to avoid free nucleation of silver particles. In general, the uniformity of growth of metallic nanoparticles is determined by the presence of stabilizing agents and the speed of reduction. In the absence of stabilizing particles, there can be both substantial anisotropic growth and/or aggregation. However, the balance once again exists between surface catalyzed growth and free nucleation in the presence of these stabilizing ligands. In order to grow the silver shells, citrate at low concentration was used as a stabilizing agent for ascorbic acid catalyzed silver reduction. This process resulted in relatively even growth of silver particles to the desired size. The stepwise growth of the particles can be seen in Figure 39.

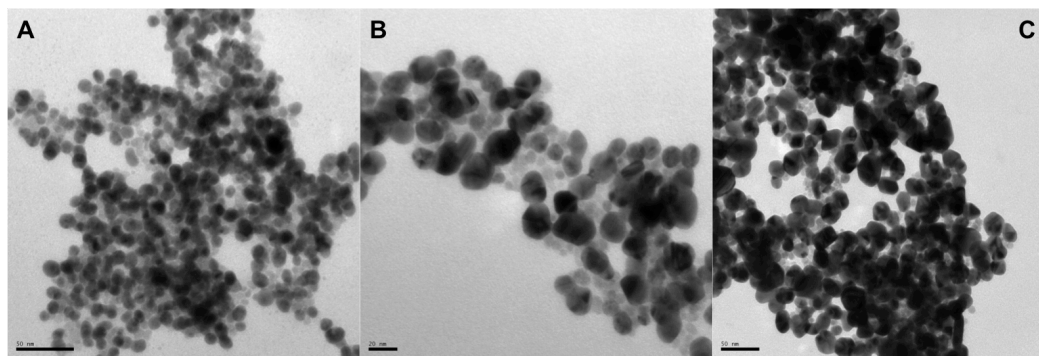


**Figure 39: Stepwise Growth of Silver Shells over Iron Oxide Templates.** Slow coating achieved by dropwise addition of ascorbic acid to solutions of silver seeded iron oxide and silver nitrate stabilized by dilute trisodium citrate. From (a) to (c), a fixed amount of silver seed iron oxide and silver nitrate are mixed in solution with stepwise additions of ascorbic acid as described in the text. Scale bars are 50nm for (a) and (c) and 20nm for (b). The growth appears relatively uniform, though it can be difficult to tell the extent of free nucleation as opposed to particle growth.

#### 5.5.2.4 Protocol for Silver Reduction on CSIOP by Glucose and Subsequent

##### Silver Shell Growth

5mL of CSIOP in water (see Section 3.4.3) were added to 90mL H<sub>2</sub>O with 10mL 1M glucose and 1.5mL 1M AgNO<sub>3</sub> (note any higher concentration of silver nitrate caused aggregation). The sample was stirred at 80C in the dark for 3 hours and gradually turned a team brown color. The sample slightly aggregated when cooled and was collected via centrifugation. The clear supernatant was removed and the seeded (Fig. 38b) particles were stably resuspended in 5mL of 2mM trisodium citrate. For nanoparticle growth, 100μL of these seeded particles was added to 10mL H<sub>2</sub>O along with 1mL 10mM AgNO<sub>3</sub>. 10mM ascorbic acid was added in 200μL increments (at 1 minute intervals) to the reaction to complete the reduction. For further reduction, this process was repeated in steps of 1mL 10mM AgNO<sub>3</sub> and 200μL additions of 10mM ascorbic acid. After complete reduction 100μL NH<sub>4</sub>OH was added to the

solution. For further galvanic replacement (see Section 5.6) the grown silver coated CSIOP were mixed in a 1:1 volume ratio with 2% PVP, precipitated with acetone, washed, vacuum dried and resuspended in water.

## **5.6 Gold Shell Generation by Galvanic Replacement**

Once a sufficient amount of silver has been grown to produce stable shells, the galvanic replacement reaction ensued as described in Chapter 4. Briefly, silver coated iron oxide particles were mixed with stabilizing PVP and precipitated with acetone to wash. The particles were then refluxed with dropwise addition of chloroauric acid ( $\text{HAuCl}_4$ ) until the reaction was complete. The amount of gold ions added was calculated to be near, but not fully replace all of the available silver. The premise of this is that nanoshell hollowing occurs first followed by shell dealloying. This would indicate that the silver coating the iron oxide would be dissolved, while the shell would still be stable as an alloy. It was not anticipated that there would be any electrochemistry between the gold ions and the iron oxide since the iron oxide is already in a fully oxidized state ( $\text{Fe}^{3+}$ ) and is not able to give up further electrons.

### **5.6.1 Transmission Electron Microscopy Characterization**

The characterization of the final products of this reaction can be seen in Figure 40. It is important to note that iron oxide possesses much lower electron density than does gold which may make it difficult to see in transmission electron microscopy

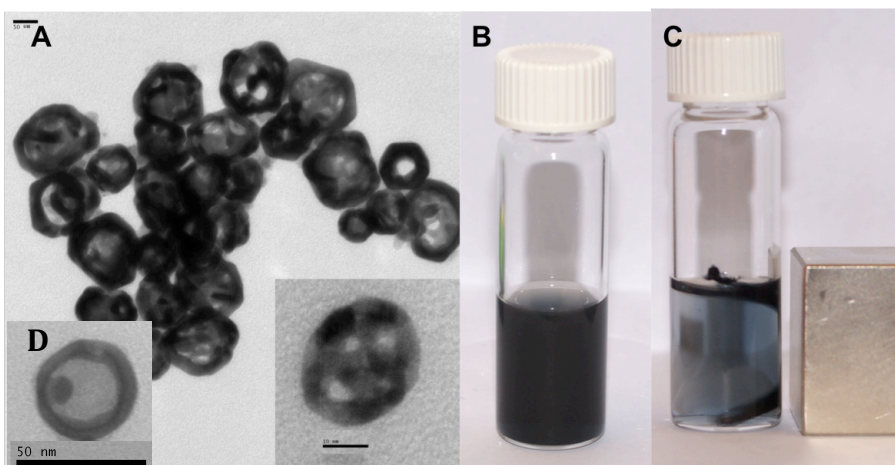


**Figure 40: Gold Shell Galvanic Replacement of Silver Coated Iron Oxide.** There is a relatively high degree of uniformity in the nanocages produced via the described mechanism and despite the existence of nanorings and some large pores, there does not appear visually to be free iron oxide outside of the shells—though it is difficult to view the presence of iron oxide inside as well because of the much greater electron density of gold producing darker contrast (a). Some samples appeared to have core/shell structures such, but the composition is difficult to verify (d). The sample was stable (b) and was attracted to a magnet (c). It was initially difficult to see the collected particles so the tube was turned to observe the trailing attraction of the particles. Residual color in the solution can be attributed to empty gold nanocages. After magnetic separation, particles could easily be stably resuspended with sonication and recollected on a magnet if desired. Scale bar in (a) is 20nm in large image and 10nm in inset.

and consequently, encapsulation of the iron oxide was difficult to verify visually.

However, there were cases where images such as Figure 40d occurred with frequency.

It is difficult to be sure of the composition of the components. However, from the visual images of silver coating and subsequent growth and the absence of obvious iron oxide on the outside of the gold shells in TEM images coupled with their attraction to a magnet, it may be inferred that the majority of the iron oxide is inside the nanocages. As a caveat to this, as is mentioned in Chapter 4, there is a degree of heterogeneity in the production of gold shells by galvanic replacement and control over shell thickness, pore size and extent of reaction is not independent. It was noted

that even in samples where the amount of gold ions added were not sufficient to completely replace the silver content, that some particles either broke or formed large pores resulting in rings that were large enough for iron oxide cores to be released. In each case, however, it was noted that a large portion of the gold shells were attracted to a magnet (Fig. 40) and were easily and stably resuspended after the removal of the magnet.

### **5.6.2 Magnetic Response Characterization**

Vibrating sample magnetometry was used to characterize the saturation magnetization saturation of the samples. As noted in the introduction to this chapter, solid metallic coatings on iron oxide have been demonstrated to substantially reduce the saturation magnetization of the iron oxide core. In order to maintain integrity of the gold shells, a non-saturating amount of gold ions were added such that shell dealloying would not occur so it needed to be determined whether this was sufficient to remove all of the silver coating from the iron oxide surface in the core of the particle. The saturation magnetization values can be seen in Figure 41. It was observed that the saturation was substantially diminished compared to free iron oxide indicating that there may still be a silver coating on the iron oxide cores. In an attempt to clean this off, the particles were incubated in nitric acid to dissolve any remaining silver. Both the gold and the iron oxide are resistant to corrosion by nitric acid (the iron protected by the oxide layer produced by nitric acid in the synthesis). After nitric acid treatment the saturation magnetization of the iron oxide was nearly fully restored

to free iron oxide levels, but the shells became unstable and fragmented as seen in Figure 42. This is indicative of two things:

1. The hollow shells formed are not pure gold, but rather a gold/silver alloy. The dissolution of the silver from the shells renders them unstable. This occurs under both boiling (where during the replacement reaction the temperature provides the energy to the gold atoms to migrate and fill dissolved  $\text{Ag}^+$  vacancies) and room temperature conditions, where the nitric acid bath could gradually be seen to change the color of the particles from blue to purple to gray as the shells became pockmarked and eventually fragmented losing the resonance absorbance (Fig. 42). Given that this same fragmentation effect occurs when gold ions are added in excess in the replacement reaction alone, it may be surmised that any stable shells produced by this mechanism are composed of gold/silver alloys and not pure gold.
2. There is not direct chemistry of gold acting directly on the surface of iron oxide. The ability of nitric acid (which does not affect gold) to restore magnetization saturation of the iron oxide is indicative of no gold coating on the iron oxide during the replacement reaction. This may also be attributed to the fact that a non-saturation amount of gold was added to replace the present silver so there may be incomplete removal of the silver layer on the iron oxide such that gold cannot access it, but also applies to iron oxide that may not have been conformally coated by silver to begin with (which may exist as well).

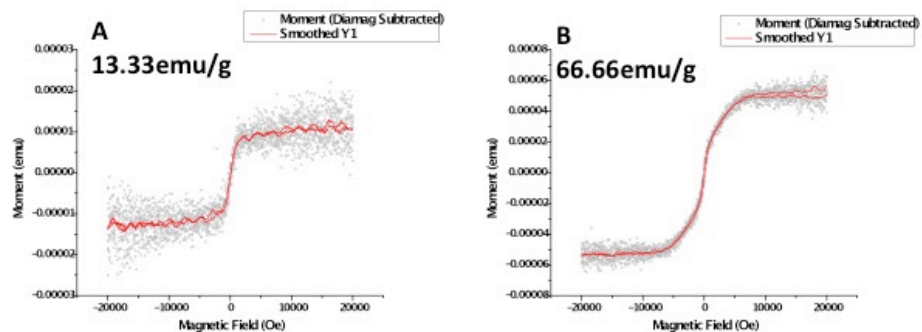


**Figure 41: Saturation Magnetization of Iron Oxide/Gold Core/Hollow Shell Nanoparticles Before and After Nitric Acid Dissolution of Free Silver.** Vibrating sample magnetometry was used to calculate saturation magnetizations of the gold shell iron oxide core structures. It was seen that as made, saturation was attenuated indicating residual silver coating on the iron oxide (see Figure 42c H<sub>2</sub>O sample) (a). Nitric acid washing restored the magnetization to near bulk values, but destabilized the nanocages as seen in Fig 42c HNO<sub>3</sub> sample (b).

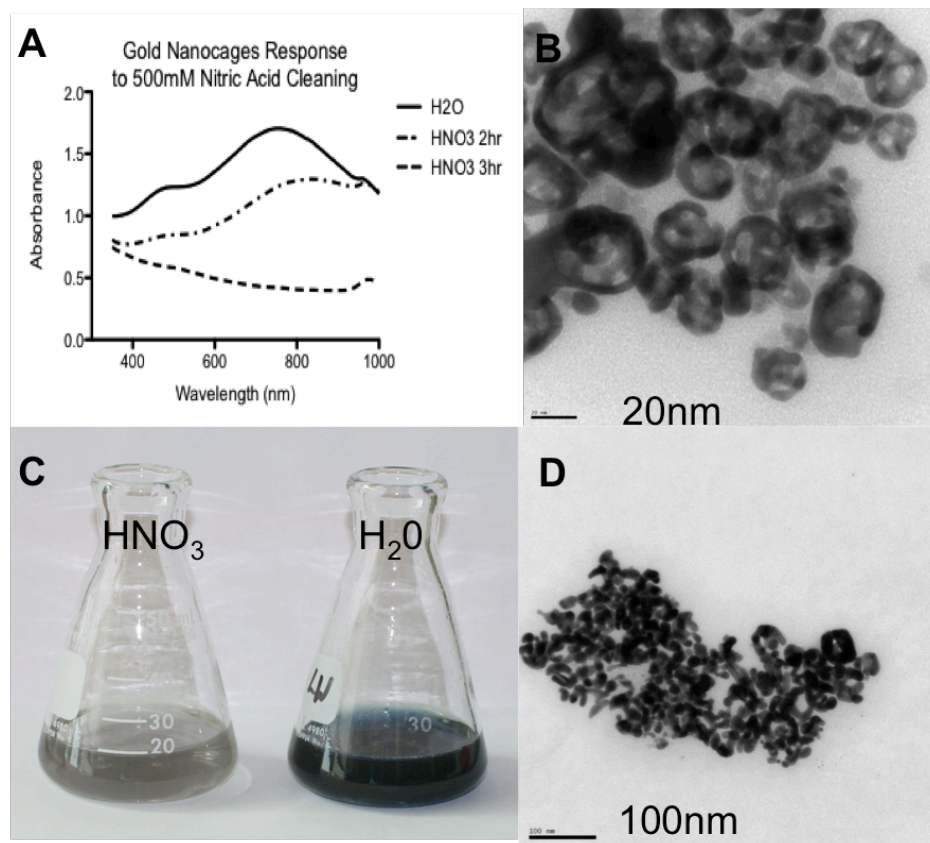


**Figure 42: TEM/Photo Images and Absorbance Profiles of Iron Oxide/Gold Core/Hollow Shell Nanoparticles Before and After Nitric Acid Dissolution of Free Silver.** The absorbance profiles of gold nanoshells produced by galvanic replacement using silver coated iron oxide as template particles showing the changes in absorbance as nitric acid dissolves and eventually breaks the nanocages (a). TEM images before and after nitric acid treatment showing destruction of nanocages (b), (d) respectively. Visual inspection of the nanocages in water and in nitric acid clearly shows distinct differences and loss of the absorbance profile characteristic of complete nanocages (c).

### 5.7 Magnetic Resonance Imaging Response

Ultimately these nanostructures are designed to be used as nanoparticle magnetic resonance imaging contrast agents, so it is valuable to understand a bit about their actual response in MRI imaging. There are two primary characteristics necessary to evaluate: 1) how the MRI relaxivities of the core/hollow shell nanostructures

compare to free iron oxide and 2) if there is a difference in response of the described nanostructures with different degrees of nanoshell porosity produced by driving the galvanic replacement to further completion. To study this, iron oxide containing gold nanocages were prepared by coating CSIOP with silver as described in section 5.5.2.3-5.5.2.4. These particles then served as templates for gold nanocage generation via galvanic replacement with varying degrees of chloroauric acid added to drive the reaction to different completion points. This is based on the concept that the initial steps of the galvanic replacement dissolve primarily the core of the silver structure leaving a hollow interior while the latter steps are involved in the dealloying of the nanocage shell. The varying amounts chloroauric acid were calculated to be close to total theoretical amount required to replace all the silver in the reaction and thus were presumed to all remove the silver core with the differentials being responsible for differing degrees of dealloying of the shell and gold ridge formation resulting in pore sizes of differing degrees. It was hypothesized that increased pore sizes would result in increased water diffusion and consequently increased observed relaxation times. Two porous gold shell/CSIOP core nanostructures were made with two different amounts chloroauric acid as in Section 5.6 and prepared in two fold serial dilutions. Magnetic measurements were performed in a 3 Tesla magnetic coil and  $r_1$ ,  $r_2$  and  $r_2^*$  measurements were determined and compared qualitatively to free CSIOP dilutions. The precise iron concentration in each of the prepared samples was not calculated, however there are several qualitative evaluations that can be made from the observations in Table 4.

**Table 4: Relaxivity Measurements for Iron Oxide/Hollow Gold Shell**

**Nanoparticles and Free CSIOP.** Samples of pure CSIOP were measured along with core/shell nanoparticle structures with varying degrees of gold replacement resulting in varying pore sizes in the shell. Sample 5 refers to 5mL of chloroauric acid producing larger pores than Sample 4 which refers to 4mL of chloroauric acid in the replacement reaction. Both Sample 4 and Sample 5 are made from the same silver coated CSIOP preparation and possess equal amounts of iron oxide. Measurements were made in a 3 Tesla MRI coil. Note that samples are normalized for concentration (max concentration is 1, .5, .25 such that absolute relaxivities are not relevant, but ratios within each sample are comparable across samples.  $r^2$  values for each linear plot are in ( ).

	<b>r1 (normalized)</b>	<b>r2 (normalized)</b>	<b>r2*(normalized)</b>	<b>r2*/r1 ratio</b>
<b>CSIOP</b>	5.22 ( $r^2=.998$ )	37.87 ( $r^2=.647$ )	62.36 ( $r^2=.975$ )	11.9
<b>Sample 5</b>	.5698 ( $r^2=.998$ )	39.22 ( $r^2=.999$ )	29.27 ( $r^2=.935$ )	48.9
<b>Sample 4</b>	.5967 ( $r^2=.996$ )	40.12 ( $r^2=.999$ )	28.60 ( $r^2=.956$ )	47.9

Several observations can be made from Table 4. Firstly, the  $r_2$  values for pure CSIOP are questionable and would benefit from a repeated measurement given the very low correlation value of the linear fit; even though the fits are much better for the samples, it becomes difficult to compare. The most immediate observation that there is very little difference between Samples 4 and 5. Both of these samples are prepared via galvanic replacement from the same sample of silver coated CSIOP and thus should contain equal amounts of iron oxide, with their only distinguishing difference being the degree of silver replacement and consequently the degree of dealloying and shell pore size. It is of note that the differential replacement is relatively minor due to the desire to have sufficient replacement to hollow the core while leaving room for varying degrees of dealloying. For this reason, and for general heterogeneity in the reaction, visualizing morphological difference in pore size via TEM was difficult to

quantify. Similarly, in order to avoid structural destabilization of the shell as seen in Figure 31, the differing extent of the reaction was not sufficient to fundamentally alter the plasmon absorbance bands between the two samples which are dictated to a larger extent in this case by the absolute diameter of the structures. Pushing the reaction toward larger and larger pores would change the plasmon band much more dramatically as seen in Figure 34, however, at the expense of destabilizing the shells.

A major point to note is the apparent effect on  $r_1$ , or the longitudinal relaxation. In general, all MRI contrast agents shorten both T1 and T2 relaxation times (increase the value of the relaxivities)<sup>108</sup>, with the degree of their effect on each determining which is their primary application. Iron oxide nanoparticles are considered T2 contrast agents<sup>54</sup> meaning that they predominantly increase the rate of spin-spin relaxation or the de-phasing of the transverse element of the perturbed magnetic moments. Ratios of  $r_2^*/r_1$  for each of the samples indicate that the strength of the  $r_1$  relaxation is substantially diminished with respect to  $r_2^*$  in the core/shell structures as compared to free CSIOP. This is either caused by a dramatic increase in  $r_2^*$  which is not likely when compared to free CSIOP, or a dramatic decrease in  $r_1$  which is consistent with restricted water access to the iron oxide core. This effect is in agreement with the observations in Figure 41, where the decreased saturation magnetization is seen in the water sample compared to the dissolved sample indicating residual silver coating the iron oxide core. The effect of the ratio of  $r_2^*/r_1$  is not likely a result of the net decreased saturation magnetization (which would likely affect both in similar ways), but rather an effect of the proximity barrier imposed by the apparent presence of a residual silver coating between the iron oxide core and the

surrounding water and its substantial effect on  $r_1$  as compared to  $r_2^*$ . Both of these pieces of evidence point to incomplete removal of a silver coating from the iron oxide cores.

## 5.8 Conclusions and Future Directions

Current approaches for the development of iron oxide nanoparticles as *in vivo* MRI contrast agents, in their efforts to increase biocompatibility and circulation time, do not effectively address some of the major attributes required for the effective transfer of the influence of a magnetic field to bulk solution for effective contrast. The common approaches of either direct inorganic coatings with metals or silica, or thick polymer coatings of PEG, dextran, or polyvinylalcohol all have the effect of attenuating one or both of the two factors that dictate the efficacy of iron oxide as an MRI contrast agent, namely the ability of the particle to magnetize in response to an externally applied magnetic field and its ability to impart its magnetic response to the surrounding bulk solution through both intimate proximity as well as rapid diffusion of affected molecules. This chapter presents a novel core/hollow shell structure that is designed to address both of attributes while still retaining a degree of freedom in functionalization of the surface to retain biocompatibility. The structures consist of a superparamagnetic iron oxide core that is encapsulated in a hollow and porous gold nanocage with pores on the size order capable of retain the iron oxide core while allowing free diffusion of water molecules. The rationale behind this design is to be able to remove the dense surface functionalities of traditional iron oxide nanoparticles utilized as MRI contrast agents that either substantially decrease the saturation

magnetization, surface access of water molecules, or the diffusion rate of those molecules to the bulk solution, while at the same time protecting it from surfaces and cells (to increase circulation time) with a biocompatible gold shell. The iron oxide cores are synthesized as in Chapter 3 and subsequently coated in a shell of silver that serves as a sacrificial template for a galvanic replacement reaction (described in Chapter 4) that produces the porous and hollow gold shell. This is an effective mechanism of producing very small gold nanocages that have magnetic properties.

The success of such a structure relies on a careful balance during the gold replacement reaction—the goal of which is to entirely hollow out the silver shell, leaving a bare iron oxide surface, while at the same time providing for a sufficient amount of dealloying of the shell to produce pores that would effectively allow water transfer. As noted in Chapter 4, these variables are not independent and several measurements indicate that the removal of silver from the surface of the iron oxide is not complete despite the initiation of shell dealloying (a process which generally proceeds after initial bulk dissolution has occurred). Both the VSM and MRI results point toward an inhibiting residual layer on the iron oxide—the VSM measurements by a decrease in saturation magnetization and the MRI results by a decrease in the  $r_1$  relaxivity. The solution to this issue is not immediately obvious. Attempts to clear this surface layer of silver by dissolution with nitric acid were indeed successful in restoring the full magnetization saturation of the iron oxide particles but at the expense of compromising the gold shell. It appears that the galvanic replacement reaction on small template particles produces nanocages that are only stable as Au/Ag alloys as either pushing the reaction to further completion with increased gold precursors or

dealloying the shell with nitric acid both result in complete destruction of the nanocage structure.

Core/hollow shell structures have been effectively created with consecutive gold/silver alloys forming both the core and the shell<sup>87</sup>, however, in these cases there is no demanding reason to have the reaction go to completion in order to visualize unique higher order nested structures. Ultimately the requirement of these structures proposed in this chapter rests on the ability to completely remove the silver coating from the iron oxide surface in the replacement reaction; without which we may as well resort to simple direct metal coatings. However, driving the reaction to this form of completion with galvanic replacement appears to have the effect of substantially destabilizing the gold shells through dealloying. Similarly, attempts to remove this layer with excess nitric acid results in shell fragmentation. With both of these observations in mind, it does not appear as if this synthetic protocol will satisfy the necessary requirements for a core/hollow shell structure of iron oxide/gold for use as MRI contrast agents.

That being said, the proposed structure still retains all the desirable characteristics of an effective *in vivo* contrast agent as described in Section 5.2. Various reported publications have commented on the negative effects that PEG, dextran and a variety of solid coatings have on the ability of iron oxide to serve as an effective contrast agent (at least when compared to bare iron oxide). The greatest ability of iron oxide to both respond to magnetic fields and convey that response to a bulk fluid occurs when the iron oxide surface is unencumbered by coatings and water diffusion near the layer is not impeded. A natural way to do this while still retaining a

degree of flexibility in functionalization for the purposes of circulation and biocompatibility is to introduce a protective shell layer around the iron oxide that will provide a passivating surface open for a variety of functionalizations. In addition this protective shell must not impede the diffusion of water to and from the iron oxide surface and bulk solution, be biocompatible, not decrease iron oxide saturation magnetization, and not dramatically increase the hydrodynamic radius of the whole structure.

Nanoshells can be composed of a variety of materials—liposomes, metals, silica, polymers, etc., however, it is more difficult to make nanocages with pores of sufficient size to not impede water diffusion (and retain encapsulated particles) that are at the same time small in total diameter (~30nm). Gold nanoshells are a good option for this because of their structural rigidity and biocompatibility. The production of these shells with appropriate dimensions of both diameter and pore size is the challenging step as, in general, the encapsulation of iron oxide nanoparticles in a variety of sacrificial materials, such as polymers, is relatively straight forward. The choice of sacrificial material and method of production of gold shells with the desired characteristics are the two principle challenges, followed by the effective removal of the sacrificial template.

The other route is to grow the iron oxide nanoparticles inside of existing shells. This has been attempted previously<sup>86</sup> via a co-precipitation method that was unsuccessful in producing superparamagnetic iron oxide—likely because of the restricted diffusion rate of the catalyzing base resulting in slower reaction time and consequently larger particles. This mechanism also will produce substantial

nucleation of iron oxide outside of the shells (much of which could irreversibly adhere to the shells in the absence of stabilizing agents) and requires extensive washing. However, there are other methods of growing iron oxide such as a hydrothermal method that is substantially slower and more uniform that may be a good approach for growing iron oxide in the presence of gold nanocages for the purpose of encapsulation. It is also possible that nanoparticles grown in the presence surfactants (such as in hydrothermal synthesis) would result in stabilized iron oxide particles that would form both inside and outside but would be stabilized so as not to adhere to the gold shells. Such hydrothermal methods utilizing surfactants have been shown to produce very uniform iron oxide nanoparticles over a period of several minutes by the oxidation of ferrous sulfate in the presence of n-decylamine at elevated temperatures and pressures in aqueous solution<sup>109</sup>. Gold shells (along with gold shells containing iron oxide cores grown inside of them) could subsequently be washed by centrifugation taking advantage of the substantial density difference of gold and iron oxide, 19.6 and 5.2 (g/cm<sup>3</sup>) respectively. With this method, the utilization of the galvanic replacement reaction as described in Chapter 4 is an ideal method for producing the gold nanocage precursors with all of the desired characteristics prior to iron oxide growth.

## **5.9 Acknowledgements**

Chapter 5 contains materials taken from Steiner, J. Esener, S. Iron Oxide/Gold Core/Hollow Porous Shell Nanostructures for Utilization as Magnetic Resonance Contrast Agents (in preparation)

## CHAPTER 6

### CONCLUDING REMARKS

To conclude this dissertation (and because it is written as a requirement for a Doctor of Philosophy degree), I would like to make a few philosophical comments both on the future and genre of nanoparticles (specifically with applications in biology) as well as the essential aspects of successful future research in the field. To begin simply, I have learned that the world of nanoparticle synthesis and functionalization, whether of simple one-component particles or higher order structures and compositions, is as much an art as it is a science. The delicate balances between precursor concentrations, temperatures, pressures, pHs for synthesis, combined with surface energies, charges, hydrophobicity, and functional groups for particle stability make the production of specific characteristics, sizes and morphologies akin to cooking as a continual search for the ideal recipe. The situation can be dramatically complicated by multistep synthetic processes where the products of one must serve as templates for the next, necessitating compatibility of a wide range of characteristics. However, it is precisely the control over these processes that is the promise and goal of nanotechnology and throughout the studies in this dissertation, I

have learned a substantial amount about the practical limitations, applications and processes that govern the synthesis and stability of structures on the nanoscale. Some of the primary lessons learned are below:

1. While it is possible to combine many distinct components in a single nanoparticle platform to achieve some mix of orthogonal functionalities, it is often neither practical or even necessarily desirable to do so. The degree of complexity introduced by each orthogonal addition to a nanoparticle platform is likely not a linear function, both in synthetic steps and, for *in vivo* applications, in the behavior and characteristics of the interactions with biological systems. In addition, it is currently ambiguous how multi-component particles are viewed from a regulatory standpoint as reproducibility and homogeneity become more difficult to achieve and define. With this in mind, in order to design useful nanoparticle platforms, it becomes essential to very clearly specify and limit the functionalities one wishes to achieve.
2. When it comes to nanoparticles, uniformity and simplicity of synthesis cannot be overrated. This is particularly true with regards to higher order structures that gain their functionality from such structures. However, it is also very important for understanding *in vivo* kinetics and distributions, which can differ substantially with nanoparticle morphology for even very simple particles<sup>110,111</sup>. For practical (and commercializable) applications, synthetic processes must produce homogeneous results that do not require extensive washing,

processing or purification. This also correlates with Lesson 1 in keeping the number of component functionalities limited.

Each of these lessons is perhaps obvious, however, for future work in the nanoparticle field, they are vitally important to understand and to take into consideration and each should be applied to future work in each of the topics discussed in this dissertation. Both of these lessons are taken from the perspective of nanoparticle research with ultimate commercializable *in vivo* applications.

There is a substantial way to go before we can fully understand the biological effects of the particles that we design for biological use and we need to tread wisely into the future so as to be clear of the path ahead. Perhaps more than any other field, the variety of possible structures and functions available to the nanoparticle field is astounding as the combinatorial mathematics of coupling materials, shapes, structures, ligands, and a plethora of other attributes exponentially increases the spectrum of possibilities. This open horizon of possibility is both a major strength and a major weakness of the nanoparticle arena and demands both a broad spectrum understanding of the field and its various components as well as a very specific and clear goal and set of criteria for any proposed topic of research. A major challenge in the nanoparticle field for biological applications is the breadth of knowledge required to make intelligent decisions about plausible directions of research. For example, chemists may be able to design perfectly monodisperse superparamagnetic iron oxide nanoparticles with extremely efficient processes, but without a firm understanding of the physics of magnetic resonance and the factors that contribute to it, these particles may have limited applications for biological imaging. Furthermore, a lack of

understanding of *in vivo* circulation kinetics and biodistributions will further limit the ultimate applicability of such particles. Ultimately this means that the world of nanoparticle synthesis for biological applications must be highly interdisciplinary and require not just the input from several areas of expertise, but a broad spectrum understanding from all contributors of all of the influential factors. This necessitates a new way of educating future researchers out of traditional segmented disciplines into a new class of synthesizers of disciplines.

From the perspective of an incoming graduate student in the field of nanotechnology, this would manifest as a requirement for extensive broad based review of each aspect of the topic that they desire to explore prior to initiating any research direction. For *in vivo* nanoparticle applications in cancer, this would entail a review and understanding of cancer physiology and cell biology with emphasis on immunogenicity, systemic clearance, and biocompatibility; an understanding of the basic classes of nanoparticles and the pros and cons of each including polymers, liposomes, metals, oxides, dendrimers, emulsions, inorganics such as silica, and others; and a basic review of historical approaches and attempts to address the issue at hand. Extensive reviews compiling both the basics as well as comprehensive reference lists of these topics are readily available<sup>8,10</sup>. From a philosophical point of view, a solid grounding in the broader field of view helps answer the question “why” in a manner that allows clarity of purpose and fuels motivation through difficulties. Ultimately, effective research projects and productive researchers are fueled by compelling consecutive answers to the question “why” as applied to each hierarchical level of the research rationale, from the details of an individual experiment all the way

to the ultimate goal of curing cancer. This progressive rationale should be the cornerstone of any research project as the most difficult (and most important) aspect of any research or project is determining the correct problem to address. Researchers who will be successful in the field of bionanotechnology will be required to understand the extensive landscape into which they are stepping, from a biological, chemical, physical, regulatory and ultimately practical standpoint to avoid the time and resource draining production of novel solutions and then searching for problems

## REFERENCES

- (1) Treacy, M. M. J.; Ebbesen, T. W.; Gibson, J. M. *Nature* **1996**, *381*, 678-680.
- (2) Hohenester, U.; Krenn, J. R. *Phys Rev B* **2005**, *72*, -.
- (3) Klar, T.; Perner, M.; Grosse, S.; von Plessen, G.; Spirkl, W.; Feldmann, J. *Phys Rev Lett* **1998**, *80*, 4249-4252.
- (4) McEuen, P. L.; Fuhrer, M. S.; Park, H. K. *Ieee T Nanotechnol* **2002**, *1*, 78-85.
- (5) Rao, S. G.; Huang, L.; Setyawan, W.; Hong, S. H. *Nature* **2003**, *425*, 36-37.
- (6) Pascual, J. I.; Mendez, J.; Gomezherrero, J.; Baro, A. M.; Garcia, N.; Landman, U.; Leudtke, W. D.; Bogachek, E. N.; Cheng, H. P. *J Vac Sci Technol B* **1995**, *13*, 1280-1284.
- (7) Taton, T. A. *Nat Mater* **2003**, *2*, 73-74.
- (8) Ferrari, M. *Nat Rev Cancer* **2005**, *5*, 161-171.
- (9) Etzioni, R.; Urban, N.; Ramsey, S.; McIntosh, M.; Schwartz, S.; Reid, B.; Radich, J.; Anderson, G.; Hartwell, L. *Nat Rev Cancer* **2003**, *3*, 243-252.
- (10) Davis, M. E.; Chen, Z.; Shin, D. M. *Nat Rev Drug Discov* **2008**, *7*, 771-782.
- (11) Brannon-Peppas, L.; Blanchette, J. O. *Adv Drug Deliver Rev* **2004**, *56*, 1649-1659.
- (12) Pramanik, M.; Swierczewska, M.; Green, D.; Sitharaman, B.; Wang, L. V. *J Biomed Opt* **2009**, *14*, -.
- (13) Sitharaman, B.; Kissell, K. R.; Hartman, K. B.; Tran, L. A.; Baikalov, A.; Rusakova, I.; Sun, Y.; Khant, H. A.; Ludtke, S. J.; Chiu, W.; Laus, S.; Toth, E.; Helm, L.; Merbach, A. E.; Wilson, L. J. *Chem Commun* **2005**, 3915-3917.
- (14) Babes, L.; Denizot, B.; Tanguy, G.; Le Jeune, J. J.; Jallet, P. *J Colloid Interf Sci* **1999**, *212*, 474-482.
- (15) Gupta, A. K.; Gupta, M. *Biomaterials* **2005**, *26*, 3995-4021

- (16) Xing, Z. W.; Wang, J. R.; Ke, H. T.; Zhao, B.; Yue, X. L.; Dai, Z. F.; Liu, J. B. *Nanotechnology* **2010**, *21*, -.
- (17) Hainfeld, J. F.; Slatkin, D. N.; Focella, T. M.; Smilowitz, H. M. *Brit J Radiol* **2006**, *79*, 248-253.
- (18) Wang, L.; Tan, W. H. *Nano Lett* **2006**, *6*, 84-88.
- (19) Bagalkot, V.; Zhang, L.; Levy-Nissenbaum, E.; Jon, S.; Kantoff, P. W.; Langer, R.; Farokhzad, O. C. *Nano Lett* **2007**, *7*, 3065-3070.
- (20) Devaraj, N. K.; Keliher, E. J.; Thurber, G. M.; Nahrendorf, M.; Weissleder, R. *Bioconjugate Chem* **2009**, *20*, 397-401.
- (21) Cho, K. J.; Wang, X.; Nie, S. M.; Chen, Z.; Shin, D. M. *Clin Cancer Res* **2008**, *14*, 1310-1316.
- (22) Chavanpatil, M. D.; Patil, Y.; Panyam, J. *Int J Pharm* **2006**, *320*, 150-156.
- (23) Patil, Y.; Sadhukha, T.; Ma, L. N.; Panyam, J. *J Control Release* **2009**, *136*, 21-29.
- (24) Feng, S. S. *Nanomedicine-Uk* **2006**, *1*, 297-309.
- (25) Hilger, I.; Hiergeist, R.; Hergt, R.; Winnefeld, K.; Schubert, H.; Kaiser, W. A. *Invest Radiol* **2002**, *37*, 580-586.
- (26) Weissleder, R. *Nat Biotechnol* **2001**, *19*, 316-317.
- (27) O'neal, D. P.; Hirsch, L. R.; Halas, N. J.; Payne, J. D.; West, J. L. *Cancer Lett* **2004**, *209*, 171-176.
- (28) Anderson, S. A.; Rader, R. K.; Westlin, W. F.; Null, C.; Jackson, D.; Lanza, C. M.; Wickline, S. A.; Kotyk, J. J. *Magnet Reson Med* **2000**, *44*, 433-439.
- (29) Verrecchia, T.; Spenlehauer, G.; Bazile, D. V.; Murrybrelier, A.; Archimbaud, Y.; Veillard, M. *J Control Release* **1995**, *36*, 49-61.
- (30) Shenoy, D.; Little, S.; Langer, R.; Amiji, M. *Pharm Res* **2005**, *22*, 2107-2114.
- (31) Kong, G.; Braun, R. D.; Dewhirst, M. W. *Cancer Res* **2000**, *60*, 4440-4445.

- (32) Xie, J.; Lee, S.; Chen, X. Y. *Adv Drug Deliver Rev* **2010**, *62*, 1064-1079.
- (33) Tuerk, C.; Gold, L. *Science* **1990**, *249*, 505-510.
- (34) Klinman, D. M. *Int Rev Immunol* **2006**, *25*, 135-154.
- (35) Bourquin, C.; Anz, D.; Zwioerek, K.; Lanz, A. L.; Fuchs, S.; Weigel, S.; Wurzenberger, C.; von der Borch, P.; Golic, M.; Moder, S.; Winter, G.; Coester, C.; Endres, S. *J Immunol* **2008**, *181*, 2990-2998.
- (36) Berti, L.; Alessandrini, A.; Facci, P. *J Am Chem Soc* **2005**, *127*, 11216-11217.
- (37) Fichou, Y.; Ferec, C. *Trends Biotechnol* **2006**, *24*, 563-570.
- (38) Rothmund, P. W. K. *Nature* **2006**, *440*, 297-302.
- (39) Wilson, D. S.; Szostak, J. W. *Annu Rev Biochem* **1999**, *68*, 611-647.
- (40) Smith, G. P.; Scott, J. K. *Method Enzymol* **1993**, *217*, 228-257.
- (41) Clackson, T.; Hoogenboom, H. R.; Griffiths, A. D.; Winter, G. *Nature* **1991**, *352*, 624-628.
- (42) Acid-Based-Technologies  
<http://www.molgen.mpg.de/~nabt/background.html> Accessed May 21, 2011.
- (43) Details-of-Research-Interests  
<http://mbg.cornell.edu/cals/mbg/research/lis-lab/researchdetails.cfm> Accessed May 21, 2011.
- (44) Bunka, D. H. J.; Stockley, P. G. *Nat Rev Microbiol* **2006**, *4*, 588-596.
- (45) Farokhzad, O. C.; Jon, S. Y.; Khademhosseini, A.; Tran, T. N. T.; LaVan, D. A.; Langer, R. *Cancer Res* **2004**, *64*, 7668-7672.
- (46) Hong, S.; Leroueil, P. R.; Majoros, I. J.; Orr, B. G.; Baker, J. R.; Holl, M. M. B. *Chem Biol* **2007**, *14*, 107-115.
- (47) Austin, R. *Nat Mater* **2003**, *2*, 567-568.
- (48) Jarvius, J.; Melin, J.; Goransson, J.; Stenberg, J.; Fredriksson, S.; Gonzalez-Rey, C.; Bertilsson, S.; Nilsson, M. *Nat Methods* **2006**, *3*, 725-727.

- (49) Rahimi, F.; Murakami, K.; Summers, J. L.; Chen, C. H. B.; Bitan, G. *Plos One* **2009**, *4*, -.
- (50) Dwyer, J. J.; Dwyer, M. A.; Kossiakoff, A. A. *Biochemistry-Us* **2001**, *40*, 13491-13500.
- (51) Vant-Hull, B.; Payano-Baez, A.; Davis, R. H.; Gold, L. *J Mol Biol* **1998**, *278*, 579-597.
- (52) Mahmoudi, M.; Sant, S.; Wang, B.; Laurent, S.; Sen, T. *Adv Drug Deliv Rev* **2010**.
- (53) Wu, W.; He, Q. G.; Jiang, C. Z. *Nanoscale Res Lett* **2008**, *3*, 397-415.
- (54) Caravan, P. *Chem Soc Rev* **2006**, *35*, 512-523.
- (55) Taylor, K. M. L.; Kim, J. S.; Rieter, W. J.; An, H.; Lin, W. L.; Lin, W. B. *J Am Chem Soc* **2008**, *130*, 2154-+.
- (56) Shubayev, V. I.; Pisanic, T. R., 2nd; Jin, S. *Adv Drug Deliv Rev* **2009**, *61*, 467-77.
- (57) Chastellain, A.; Petri, A.; Hofmann, H. *J Colloid Interf Sci* **2004**, *278*, 353-360.
- (58) De Palma, R.; Peeters, S.; Van Bael, M. J.; Van den Rul, H.; Bonroy, K.; Laureyn, W.; Mullens, J.; Borghs, G.; Maes, G. *Chem Mater* **2007**, *19*, 1821-1831.
- (59) Jain, T. K.; Richey, J.; Strand, M.; Leslie-Pelecky, D. L.; Flask, C. A.; Labhasetwar, V. *Biomaterials* **2008**, *29*, 4012-4021.
- (60) Ma, M.; Zhang, Y.; Yu, W.; Shen, H. Y.; Zhang, H. Q.; Gu, N. *Colloid Surface A* **2003**, *212*, 219-226.
- (61) Shen, X. C.; Fang, X. Z.; Zhou, Y. H.; Liang, H. *Chem Lett* **2004**, *33*, 1468-1469.
- (62) Huang, X.; Schmucker, A.; Dyke, J.; Hall, S. M.; Retrum, J.; Stein, B.; Remmes, N.; Baxter, D. V.; Dragnea, B.; Bronstein, L. M. *J Mater Chem* **2009**, *19*, 4231-4239.
- (63) Bruce, I. J.; Sen, T. *Langmuir* **2005**, *21*, 7029-7035.

- (64) Ji, X. J.; Shao, R. P.; Elliott, A. M.; Stafford, R. J.; Esparza-Coss, E.; Bankson, J. A.; Liang, G.; Luo, Z. P.; Park, K.; Markert, J. T.; Li, C. *J Phys Chem C* **2007**, *111*, 6245-6251.
- (65) Tzitzios, V.; Basina, G.; Bakandritsos, A.; Hadjipanayis, C. G.; Mao, H.; Niarchos, D.; Hadjipanayis, G. C.; Tucek, J.; Zboril, R. *J Mater Chem* **2010**, *20*, 5418-5428.
- (66) Merrill, R. C.; Spencer, R. W. *J Phys Colloid Chem* **1950**, *54*, 806-812.
- (67) Jain, P. K.; Huang, X. H.; El-Sayed, I. H.; El-Sayed, M. A. *Accounts Chem Res* **2008**, *41*, 1578-1586.
- (68) An, K.; Hyeon, T. *Nano Today* **2009**, *4*, 359-373.
- (69) Cai, W.; Gao, T.; Hong, H.; Sun, J. *Nanotechnology, Science and Applications* **2008**, *1*, 17-32.
- (70) Alric, C.; Serduc, R.; Mandon, C.; Taleb, J.; Le Duc, G.; Le Meur-Herland, A.; Billotey, C.; Perriat, P.; Roux, S.; Tillement, O. *Gold Bull* **2008**, *41*, 90-97.
- (71) Oldenburg, S. J.; Averitt, R. D.; Westcott, S. L.; Halas, N. J. *Chem Phys Lett* **1998**, *288*, 243-247.
- (72) Yong, K. T.; Sahoo, Y.; Swihart, M. T.; Prasad, P. N. *Colloid Surface A* **2006**, *290*, 89-105.
- (73) Shi, W. L.; Sahoo, Y.; Swihart, M. T.; Prasad, P. N. *Langmuir* **2005**, *21*, 1610-1617.
- (74) Kah, J. C. Y.; Phonthammachai, N.; Wan, R. C. Y.; Song, J.; White, T.; Mhaisalkar, S.; Ahmad, I.; Sheppard, C.; Olivo, M. *Gold Bull* **2008**, *41*, 23-36.
- (75) Yang, J.; Lee, J.; Kang, J.; Oh, S. J.; Ko, H. J.; Son, J. H.; Lee, K.; Suh, J. S.; Huh, Y. M.; Haam, S. *Adv Mater* **2009**, *21*, 4339-+.
- (76) Chen, J.; Saeki, F.; Wiley, B. J.; Cang, H.; Cobb, M. J.; Li, Z. Y.; Au, L.; Zhang, H.; Kimmey, M. B.; Li, X. D.; Xia, Y. *Nano Lett* **2005**, *5*, 473-477.
- (77) Kalele, S.; Gosavi, S. W.; Urban, J.; Kulkarni, S. K. *Curr Sci India* **2006**, *91*, 1038-1052.
- (78) Lim, Y. T.; Park, O. O.; Jung, H. T. *J Colloid Interf Sci* **2003**, *263*, 449-453.

- (79) Halas, N. *Optics and Photonics News* **2002**, 26-30.
- (80) Sanchez-Gaytan, B. L.; Park, S. J. *Langmuir* **2010**, *26*, 19170-19174.
- (81) Leff, D. V.; Brandt, L.; Heath, J. R. *Langmuir* **1996**, *12*, 4723-4730.
- (82) Brown, K. R.; Walter, D. G.; Natan, M. J. *Chem Mater* **2000**, *12*, 306-313.
- (83) You, J. O.; Auguste, D. T. *Biomaterials* **2010**, *31*, 6859-6866.
- (84) Lu, X. M.; Tuan, H. Y.; Chen, J. Y.; Li, Z. Y.; Korgel, B. A.; Xia, Y. N. *J Am Chem Soc* **2007**, *129*, 1733-1742.
- (85) Xianmao Lu, J. C., S E Skrabalak, and Younan Xia *J. Nanoengineering and Nanosystems* **2008**, *221*.
- (86) Huang, C. W.; Jiang, J. C.; Muangphat, C.; Sun, X. K.; Hao, Y. W. *Nanoscale Res Lett* **2010**, *6*, -.
- (87) Sun, Y. G.; Wiley, B.; Li, Z. Y.; Xia, Y. N. *J Am Chem Soc* **2004**, *126*, 9399-9406.
- (88) Chu, C. H.; Wang, Y. C.; Huang, H. Y.; Wu, L. C.; Yang, C. S. *Nanotechnology* **2011**, *22*, -.
- (89) Zhang, Y.; Kohler, N.; Zhang, M. Q. *Biomaterials* **2002**, *23*, 1553-1561.
- (90) Iglesias-Silva, E.; Vilas-Vilela, J. L.; Lopez-Quintela, M. A.; Rivas, J.; Rodriguez, M.; Leon, L. M. *J Non-Cryst Solids* **2010**, *356*, 1233-1235.
- (91) Yan, F.; Xu, H.; Anker, J.; Kopelman, R.; Ross, B.; Rehemtulla, A.; Reddy, R. *J Nanosci Nanotechno* **2004**, *4*, 72-76.
- (92) Wassel, R. A.; Grady, B.; Kopke, R. D.; Dormer, K. J. *Colloid Surface A* **2007**, *292*, 125-130.
- (93) Iglesias-Silva, E.; Rivas, J.; Isidro, L. M. L.; Lopez-Quintela, M. A. *J Non-Cryst Solids* **2007**, *353*, 829-831.
- (94) Lusse, S.; Arnold, K. *Macromolecules* **1996**, *29*, 4251-4257.
- (95) Jin, Y.; Wang, W.; Su, Z. H. *Macromolecules* **2011**, *44*, 2132-2139.

- (96) Khemtong, C.; Togao, O.; Ren, J. M.; Kessinger, C. W.; Takahashi, M.; Sherry, A. D.; Gao, J. M. *J Magn Reson* **2011**, *209*, 53-60.
- (97) Leslie E.W. LaConte, P., 1 Nitin Nitin, PhD,1 Omar Zurkiya, PhD,1; Daniela Caruntu, P., 2 Charles J. O'Connor, PhD,2 Xiaoping Hu, PhD,1 and; Gang Bao, P. *JOURNAL OF MAGNETIC RESONANCE IMAGING* **2007**, *26*, 1634–1641.
- (98) Shukla, R.; Bansal, V.; Chaudhary, M.; Basu, A.; Bhonde, R. R.; Sastry, M. *Langmuir* **2005**, *21*, 10644-10654.
- (99) Berry, C. C.; Wells, S.; Charles, S.; Curtis, A. S. G. *Biomaterials* **2003**, *24*, 4551-4557.
- (100) Chouly, C.; Pouliquen, D.; Lucet, I.; Jeune, J. J.; Jallet, P. *J Microencapsul* **1996**, *13*, 245-255.
- (101) Chen, D.; Liu, H. Y.; Liu, J. S.; Ren, X. L.; Meng, X. W.; Wu, W.; Tang, F. Q. *Thin Solid Films* **2008**, *516*, 6371-6376.
- (102) Kobayashi, Y.; Salgueirino-Maceira, V.; Liz-Marzan, L. M. *Chem Mater* **2001**, *13*, 1630-1633.
- (103) Liang, C. H.; Wang, C. C.; Lin, Y. C.; Chen, C. H.; Wong, C. H.; Wu, C. Y. *Anal Chem* **2009**, *81*, 7750-7756.
- (104) Rong Hu, Q. H., Jingke Huang , Wei Wu and Lei Zeng *IEEE* **2008**, 1522-1525.
- (105) Park, H. H.; Zhang, X.; Choi, Y. J.; Park, H. H.; Hill, R. H. *J Nanomater* **2011**, -.
- (106) Park, H. H.; Zhang, X.; Choi, Y. J.; Kim, H.; Park, H. H.; Hill, R. H. *J Ceram Soc Jpn* **2010**, *118*, 1002-1005.
- (107) Park, E. H.; Jung, J. H.; Chung, H. H. *Chemosphere* **2006**, *64*, 432-436.
- (108) Chen, R. C.; Lii, J. M.; Chou, C. T.; Chang, T. A.; Chen, W. T.; Li, C. S.; Tu, H. Y. *J Formos Med Assoc* **2008**, *107*, 798-805.
- (109) Takami, S.; Sato, T.; Mousavand, T.; Ohara, S.; Umetsu, M.; Adschiri, T. *Mater Lett* **2007**, *61*, 4769-4772.
- (110) De Jong, W. H.; Hagens, W. I.; Krystek, P.; Burger, M. C.; Sips, A. J. A. M.; Geertsma, R. E. *Biomaterials* **2008**, *29*, 1912-1919.

(111) Glangchai, L. C.; Caldorera-Moore, M.; Shi, L.; Roy, K. *J Control Release* **2008**, *125*, 263-272.